MPD physics performance studies in Bi+Bi collisions at $\sqrt{s_{NN}} = 9.2$ GeV

R. Abdulin[20], V. Abgaryan[1], R. Adhikary[16], K.G. Afanaciev[16,13], S.V. Afanaciev[16], G. Agakishiev[16], E.I. Alexandrov[16], I.N. Alexandrov[16], M. Alvarado-Hernández[14], D.I. Andreev[16], S.V. Andreeva[16], T.V. Andreeva[16], E.V. Andronov[28], N.V. Anfimov[16], A. Anikeev[21], A.V. Anufriev[28], A.A. Aparin[16], R. Arteche-Diaz[16], V.I. Astakhov[16], T. Aushev[23], S.P. Avdeev[16], G.S. Averichev[16], A.V. Averyanov[16],A. Ayala[14], V.N. Azorskiy[16], L. Bavichev[32], V.A. Babkin[16], P. Bakhtin[19], A.I. Balandin[16], N.A. Balashov[16], A. Baranov[10], D.A. Baranov[16], N.V. Baranova[31], R.V. Baratov[16], N. Barbashina[21], V. Barbasová[23], V.M. Baryshnikov[16], K.D. Basharina[16], A.E. Baskakov[16], V.G. Bayev[13], A.G. Bazhazhin[16], S.N. Bazylev[16], P. Beletsky[25], S.V. Belokurova[28], A.V. Belyaev[16], E.V. Belyaeva[16], D.V. Belyakov[16], Y. Berdnikov[24], F. Berezov[22], M. Bhattacharjee[16], W. Bietenholz[14], D. Blau[19], G.A Bogdanova[31], D.N. Bogoslovsky[16], I.V. Boguslavski[16], E.A. Bondar[12], E.E. Boos[31], A. Botvina[10], A. Brandin[21], S.A. Bulychjov[19], V. Burdelnaya[25], N. Burmasov[20], M.G. Buryakov[16], J. Busa Jr.[16], A.V. Butenko[16], S.G. Buzin[16], A.V. Bychkov[16], Z. Cao[35], C. Ceballos-Sánchez[16], V.V. Chalyshev[16], V.F. Chepurnov[16], Vl.V. Chepurnov[16], G.A. Cheremukhina[16], A.S. Chernyshov[31], E. Cuautle[14], A. Demanov[21], D.V. Dementiev[16], D. Derkach[8], A.V. Dmitriev[16], E.V. Dolbilina[16], V.H. Dodokhov[16], A.G. Dolbilov[16], I. Domínguez[6], D.E. Donetz[16], V.I. Dronik[16], A.Yu. Dubrovin[16], P.O. Dulov[16,26], V.B. Dunin[16], A. Dyachenko[20], A.A. Efremov[16], D.S. Egorov[16], V.V. Elsha[16], N.E. Emelianov[16], J. Erkenova[25], G.H. Eyyubova[31], A. Ezhilov[20], D. Fang[7], O.V. Fateev[16], O. Fedin[20], A.I. Fedosimova[12], Yu.I. Fedotov[16], A.S. Fedotov[16], J.A. Fedotova[27], A.A. Fedunin[16], S. Feng[33], G.A. Feofilov[28], I.A. Filippov[16], G. Fomenko[19], M.A. Gaganova[16], K.A. Galaktionov[28], Ya.D. Galkin[27], A.S. Galoyan[16], Ch. Gao[17], P.E. García-González[15], O.P. Gavrishuk[16], N.S. Geraksiev[26], S.E. Gerasimov[16], K.V. Gertsenberger[16], N. Gevorgyan[1], Y. Ghoneim[16], O. Golosov[19], V.M. Golovatyuk[16], M. Golubeva[10], A.O. Golunov[16], I. Goncharov[22], N.V. Gorbunov[16], P. Gordeev[19], I.P. Gorelikov[16], H. Grigorian[1], P.N. Grigoriev[16], F. Guber[10], D. Guo[17], A.V. Guskov[16], D. Han[34], W. Han[11], W. He[7], L.A. Hernández-Rosas[3], M. Herrera[5], S. Hnatic[16], M. Hnatič[23], M. Huang[29], S.A. Ibraimova[12], D.M. Idrisov[10], T.K. Idrisova[12], Z.A. Igamkulov[16], S.N. Igolkin[28], A.Yu. Isupov[16], D. Ivanishchev[20], A.V. Ivanov[16], A. Ivashkin[10], J. Jiao[30], I. Jadochnikov[1], S.I. Kakurin[16], N.I. Kalinichenko[28], A. Kamkin[25], M.N. Kapishin[16], D.E. Karmanov[31], N. Karpushkin[10], I.A. Kashunin[16], Y. Kasumov[22], A.O. Kechechyan[16], G.D. Kekelidze[16], V.D. Kekelidze[16], A. Khanzadeev[20], P.I. Kharlamov[31], G.G. Khodzhibagiyan[16], E. Kidanova[2], V.A. Kireyeu[16], Yu.T. Kiriushin[16], L. Kochenda[20], O.L. Kodolova[31], A.A. Kokorev[16], A.O. Kolesnikov[16], V.I. Kolesnikov[16], N. Kolomoyets[16], A.A. Kolozhvari[16], V. Kondtratiev[28], V.V. Korenkov[16], M.G. Korolev[31], V.L. Korotkikh[31], A.I. Kostylev[16], D. Kotov[20,24], V.N. Kovalenko[28], I. Kozmin[25], V.A. Kramarenko[16], A. Kravčáková[23], P. Kravtsov[20], Yu.F. Krechetov[16], I.V. Kruglova[16], V.A. Krylov[16], A.V. Krylov[16], E. Kryshen[20], A.P. Kryukov[31], S.N. Kuklin[16], V.V. Kulikov[19], A.A. Kulikovskaya[19], A.V. Kunts[27], E. Kurbatov[8], A. Kurepin[10], V. Kuskov[19], V.A Kuzmin[31], A. Kyrianova[20], D.E. Lanskoy[31], N.A. Lashmanov[16], R. Lednicky[16], V.V. Leontev[16], I.A. Lebedev[12], L. Li[34], P. Li[9], S. Li[33], T.Z. Ligdenova[16], A.V. Litomin[27], E.I. Litvinenko[16], D. Liu[30], V.I. Lobanov[16], Yu.Yu. Lobanov[16], S.P. Lobastov[16], I.P. Lokhtin[31], J.R. Lukstins[16], D. Larionova[24], A. Lobanov[24], P. Lu[35], I. Luna-Reyes[15], X. Luo[17], Y. Ma[7], D.T. Madigozhin[16], A.A. Makarov[16], V.I. Maksimenkova[16], A.I. Malakhov[16], M. Malaev[20], I.A. Maldonado-Cervantes[16], V. Maleev[20], I.V. Malikov[16], N.A. Maltsev[28], N.A. Makarov[28], M. Maksimov[20], M.A. Martemianov[19], P. Martínez-Torres[15], M.A. Matsyuk[19], M. Medvedeva[27], D.I. Melikov[31], D.G. Melnikov[16], M.M. Merkin[31], S.P. Mertz[16], I.N. Meshkov[16], V.V. Mialkovski[16], I.I. Migulina[16], K.R. Mikhaylov[16,20], G.D. Milnov[16], J. Milosevic[37], Yu.I. Minaev[16], S.A. Mituxin[16], G.V. Mescheriakov[16], N.A. Molokanova[16], S. Morozov[10], A.A. Moshkin[16], S.A. Movchan[16], A.N. Moybenko[16], K.A. Mukhin[16], Yu.A. Murin[16], S. Musin[10], G.G. Musulmanbekov[16], V.V. Mytsin[16], E.E. Muravkin[16], L. Nadderd[37], R.V. Nagdasev[16], Yu. Naryshkin[20], A.V. Nechaevskiy[16], V.A. Nikitin[16], V.A. Novoselov[16], I.A. Olexs[16], A.G. Olshevski[16], O.E. Orlov[16], V. Papoyan[1], P.E. Parfenov[16,21], S.S. Pargicky[16], M.E. Patiño-Salazar[14], S.V. Patronova[16], V.A. Pavlyukevich[16], I.S. Pelevanyuk[16], V.A. Penkin[16], D. Peresunko[19], D.V. Peshekhonov[16], V.A. Petrov[16], V.V. Petrov[28], A.V. Piliar[16], A. Piloyan[1], S.M. Piyadin[16], M.N. Platonova[31], D.V. Podgainy[16], M. Pokidova[20], V.N. Popov[28], D.S. Potapov[16], D.S. Prokhorova[28], N.A. Prokofiev[28], D.I. Priakhina[16], I. Pshenichnov[10], A.M. Puchkov[28], N. Pukhaeva[22,16] A. Pyatigor[2], J. Qin[35], F. Ratnikov[8], A. Raya[15], V. Rekovic[37], M. Reyes-Gutiérrez[15], S. Reyes-Peña[16], A. Riabov[20], V. Riabov[20], Yu. Riabov[20], S.P. Rode[16], A. Rodríguez-Alvarez[16], O.V. Rogachevsky[16], V.Yu. Rogov[16], V.A. Rudnev[28], I.A. Rufanov[16], M.M. Rumyantsev[16], I. Rudziankou[32], Yu. Rusak[32], A.A. Rybakov[16], Z. Sadygov[16], A.U. Sáenz-Trujillo[4], V.A. Samsonov[16], A.A. Savenkov[16], S. Savenkov[10], S.A. Sedykh[16], T.V. Semchukova[16], A.Yu. Semenov[16], R.N. Semenov[16], I.A. Semenova[16], V.Z. Serdyuk[16], S.V. Sergeev[16], A.S. Serikkanov[12], E.V. Serochkin[16], Yu. Shafarevich[27], D. Shapaev[24], O.M. Shaposhnikova[28], L.M. Shcheglova[31], M.F. Shopova[26], D.V. Shchegolev[16], A.V. Shchipunov[16], Y. Shen[29], A.D. Sheremetiev[16], A.I. Sheremetieva[16], S. Shi[17], M.O. Shitenkov[16], E.E. Shmanay[27], S.V. Shmatov[16], I.A. Shmyrev[16], A.A. Shunko[16], A.V. Shutov[16], V.B. Shutov[16], A.O. Sidorin[16], S.V. Simak[28], I.V. Slepnev[16], V.M. Slepnev[16], I.P. Slepov[16], I.A. Smelyanskiy[16], A.M. Snigirev[31], O.V. Sobol[28], A.N. Solomin[31], A.S. Sorin[16], G.G. Stiforov[16], L.Yu. Stolypina[16], E.A. Streletskaya[16], O.I. Streltsova[16], M. Strikhanov[21], T.A. Strizh[16], A. Strizhak[10],

X. Sun[17], D.A. Suvarieva[26], A. Svetlichnyi[10], Z. Tang[35], M.E. Tejeda-Yeomans[5], A. Taranenko[21], V.A. Tchekhovski[27], D.A. Tereshin[16], A.V. Terletskiy[16], O.V. Teryaev[16], V.V. Tikhomirov[16], A.A. Timoshenko[16], G. Tinoco-Santillán[4], V.D. Toneev[16], N.D. Topilin[16], T.Yu. Tretyakova[31], V.V. Trofimov[16], V.V. Troshin[16,21], G.V. Trubnikov[16], A.Trutse[21], E.A. Tsapulina[16], I. Tserruya[16,*], I.A. Tyapkin[16], S.Yu. Udovenko[16], V.V. Uzhinsky[16], M. Val'a[23], F.F. Valiev[28], V.A. Vasendina[16], A. Vasilyev[20], V.V. Vechernin[28], V.K. Velichkov[26], S.V. Vereshagin[16], A.S. Vodopyanov[16], K. Vokhmyanina[2], V. Volkov[10], A.L. Voronin[16], A.N. Vorontsov[16], V. Voronyuk[16], J. Vrláková[23], J. Wang[9], X. Wang[36], Y. Wang[34], Y. Wang[30], Y. Wang[30], Y. Wang[17], K. Wu[33], L. Xiao[17], M. Xiao[36], G. Xie[29], C. Yang[30], H. Yang[11], Z. Yuan[29], V.I. Yurevich[16], S.V. Yurchenko[28], E.E. Zabrodin[31], G. Zalite[20], N.I. Zamyatin[16], S.A. Zaporozhets[16], A.K. Zarochentsev[28], W. Zha[35], M. Zhalov[20], H. Zhang[11], Y. Zhang[11], Z. Zhang[34], C. Zhao[11], I. Zhavoronkova[21], V.I. Zherebchevsky[28], X. Zhu[34], X. Zhu[9], A.I. Zinchenko[16], D.A. Zinchenko[16], V.N. Zruyev[16], M.I. Zuev[16], I.A. Zur[27], and A.P. Zvyagina[28]

[1]*A.I. Alikhanyan National Lab of Armenia, Yerevan, ARMENIA*
[2]*Belgorod National Research University, Belgorod, RUSSIA*
[3]*Departamento de Física, Universidad Autónoma Metropolitana-Iztapalapa, Mexico City, MEXICO*
[4]*División de Posgrado, Facultad de Ingeniería Eléctrica, Universidad Michoacana de San Nicolás de Hidalgo, Morelia, MEXICO*
[5]*Facultad de Ciencias - CUICBAS, Universidad de Colima, Colima, MEXICO*
[6]*Facultad de Ciencias Físico-Matemáticas, Universidad Autónoma de Sinaloa, Culiacán, MEXICO*
[7]*Fudan University, Shanghai, CHINA*
[8]*HSE University, Moscow, RUSSIA*
[9]*Huzhou University, Huzhou, CHINA*
[10]*Institute for Nuclear Research of the Russian Academy of Sciences, Moscow, RUSSIA*
[11]*Institute of Modern Physics of the Chinese Academy of Science, Langzhou, CHINA*
[12]*Institute of Physics and Technology, Satbayev University, Almaty, KAZAKHSTAN*
[13]*Institute of Power Engineering of the National Academy of Sciences of Belarus, Minsk, BELARUS*
[14]*Instituto de Ciencias Nucleares, Universidad Nacional Autónoma de México, Mexico City, MEXICO*
[15]*Instituto de Física y Matemáticas, Universidad Michoacana de San Nicolás de Hidalgo, Morelia, MEXICO*
[16]*Joint Institute for Nuclear Research, Dubna, RUSSIA*
[*]*also at Weizmann Institute of Science, Rehovot, ISRAEL*
[17]*Key Laboratory of Quark and Lepton Physics of the Ministry of Education, Central China Normal University, Wuhan, CHINA*
[18]*Moscow Institute of Physics and Technology, Moscow, RUSSIA*
[19]*National Research Center "Kurchatov Institute", Moscow, RUSSIA*
[20]*Petersburg Nuclear Physics Institute named by B.P. Konstantinov of NRC "Kurchatov Institute", Gatchina, RUSSIA*
[21]*National Research Nuclear University MEPhI (Moscow Engineering Physics Institute), Moscow, RUSSIA*
[22]*North Ossetian State University, Vladikavkaz, RUSSIA*
[23]*Pavol Jozef Šafárik University, Košice, SLOVAKIA*
[24]*Peter the Great St. Petersburg Polytecnic University, Saint Petersburg, RUSSIA*
[25]*Plekhanov Russian University of Economics, Moscow, RUSSIA*
[26]*Plovdiv University Paisii Hilendarski, Plovdiv, BULGARIA*
[27]*Research Institute for Nuclear Problems of Belarusian State University (INP BSU), Minsk, BELARUS*
[28]*Saint Petersburg State University, Saint Petersburg, RUSSIA*
[29]*School of Nuclear Science and Technology, University of the Chinese Academy of Sciences, Beijing, CHINA*
[30]*Shandong University, Qingdao, CHINA*
[31]*Skobeltsyn Institute of Nuclear Physics (SINP) of the Moscow State University, Moscow, RUSSIA*
[32]*State Scientific Institution "Joint Institute for Energy and Nuclear Research - Sosny" of the National Academy of Sciences of Belarus, Minsk, BELARUS*
[33]*Three Gorges University, Yichang, CHINA*
[34]*Tsinghua University, Beijing, CHINA*
[35]*University of Science and Technology of China, Hefei, CHINA*
[36]*University of South China, Hengyang, CHINA*
[37]*"VINČA" Institute of Nuclear Science - National Institute of the Republic of Serbia, University of Belgrade, SERBIA*

Received 31 March 2025; accepted 2 June 2025

The Multi-Purpose Detector (MPD) is one of the three experiments of the Nuclotron Ion Collider-fAcility (NICA) complex, which is currently under construction at the Joint Institute for Nuclear Research in Dubna. With collisions of heavy ions in the collider mode, the MPD will cover the energy range $\sqrt{s_{NN}} = 4 - 11$ GeV to scan the high baryon-density region of the QCD phase diagram. With expected statistics of 50–100 million events collected during the first run, MPD will be able to study a number of observables, including measurements of light hadrons and (hyper)nuclei production, particle flow, correlations and fluctuations, have a first look at dielectron production, and modification of vector-meson properties in dense matter. In this paper, we present selected results of the physics feasibility studies for the MPD experiment in Bi+Bi collisions at $\sqrt{s_{NN}} = 9.2$ GeV, the system considered as one of the first available at the NICA collider.

Keywords: Heavy-ion collision experiments; quark-gluon matter.

DOI: https://doi.org/10.31349/RevMexFis.71.041201

1. Introduction

Heavy-ion collisions have been used to study QCD matter under extreme conditions of high temperatures and baryon densities for over 30 years. The main goal of this research has been to better understand the rich structure of the QCD phase diagram and to search for the phase transition into a new state of matter, the quark-gluon plasma (QGP), and the existence of a Critical End-Point (CEP) [1-3]. The research program started in the late 80 s at the AGS ($\sqrt{s_{NN}} \sim 5$ GeV) and the SPS ($\sqrt{s_{NN}} \sim 17$ GeV). It was followed later by detailed studies of the hot matter at much higher energies at RHIC (up to $\sqrt{s_{NN}} = 200$ GeV) and LHC (up to $\sqrt{s_{NN}} = 5$ TeV). All these studies revealed the existence of a transition from hadronic matter to a QGP at a temperature $T_{\rm c} \sim 160$ MeV and near-zero net baryon densities, which is consistent with the lattice QCD predictions of a cross-over transition [4].

Heavy-ion collisions at lower energies ($\sqrt{s_{NN}} = 2 - 10$ GeV) provide the means to study a different region of the QCD phase diagram, which is characterized by lower temperatures but higher net baryon densities. Models predict that a first-order phase transition and a CEP may exist under such conditions, which remain to be proven experimentally [5]. The corresponding region of the QCD phase diagram lies in the center of the Beam Energy Scan (BES) programs carried out by the STAR experiment at RHIC, the NA61 experiment at SPS, the BM@N experiment at the Nuclotron and the HADES experiment at SIS18 [6-8] as well as at the upcoming Nuclotron-based Ion Collider Facility (NICA) [9], the Facility for Antiproton and Ion Research (FAIR) [1] and the High-Intensity Heavy-Ion Accelerator Facility (HIAF) [10]. So far, no evidence of the CEP nor signs of the first-order phase transition have been observed in these experiments.

The Multi-Purpose Detector (MPD) at NICA, which is in the final stage of construction at the Joint Institute for Nuclear Research (JINR) in Dubna, Russia, will provide an excellent opportunity to extend these studies to the range of energies $\sqrt{s_{NN}} = 4 - 11$ GeV by providing high-luminosity scans both in collision energy and in system size [9].

The MPD is a 4π spectrometer, depicted in Fig. 1, with excellent PID for charged hadrons, electrons and photons. In the first stage of operation, the MPD detector has three main subsystems covering the central rapidity region: the Time Projection Chamber (TPC), the electromagnetic calorimeter (ECAL), the Time of Flight (TOF) and two forward region subsystems: the Fast Forward Detector (FFD) and the Forward Hadron Calorimeter (FHCAL). One of the advantages of the MPD over the current NA61/SHINE experiment at the SPS or the future CBM experiment at FAIR is the capability to operate both in fixed target and colliding modes. The MPD will complement the STAR beam energy scan program with measurements at mid-rapidity at $\sqrt{s_{NN}} = 4 - 7.7$ GeV. Other advantages of the MPD are its ability to perform a system-size scan and direct photon measurements that provide unique information on the properties of the hot matter produced in nuclear collisions in the NICA energy range.

The search for the phase transition and CEP will be done by measuring a wide variety of observables, including production of light-flavor hadrons and (hyper)nuclei, electromagnetic probes such as (direct) photons and dielectrons, by studying the particle flow, correlations and fluctuations. First

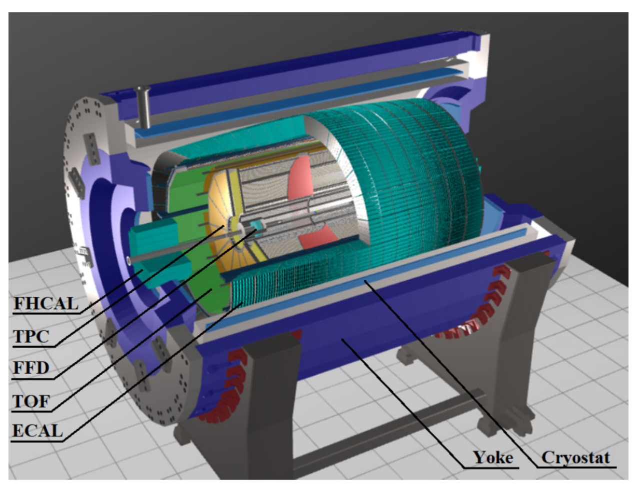

FIGURE 1. Schematic view of the MPD apparatus in the first stage of operation. The central barrel subsystems from inside to outside: TPC, TOF and ECAL and the forward subsystems: FFD and FHCAL.

tests with a beam at the NICA collider are expected to start in the summer of 2025. Bi+Bi collisions at $\sqrt{s_{NN}} = 9.2$ GeV are among the first systems to be studied in the NICA collider. The choice of nuclei is determined by the ion source capabilities in the initial configuration. The energy was picked to be close to one of the energies studied in Au+Au collisions by the STAR experiment during the BES program to provide some basic comparison.

In this paper, we present selected results of physics feasibility studies for the MPD experiment in Bi+Bi collisions at $\sqrt{s_{NN}} = 9.2$ GeV with a focus on observables that will become available with 50–100 M collected events. The paper is organized as follows: In Sec. 2, we briefly describe the setup of the MPD experiment. In Sec. 3, we describe the data analysis framework, which was used to produce the presented results. In Sec. 4, we discuss the global characterization of heavy-ion collisions and in Sec. 5, we present physics feasibility and performance studies for selected physics observables that can be carried out with the MPD in the first run. A summary is provided in Sec. 6.

2. MPD setup

The design of the experimental setup and the preliminary results of the MPD performance with heavy-ion beams have been published in Ref. [11]. The MPD is designed as a magnetic spectrometer capable of measuring and identifying charged hadrons, electrons, and photons over a wide range of momentum and rapidity. In this section, we give a brief description of the setup in the first stage of the MPD [12]. A schematic view of the MPD is shown in Fig. 1. The superconducting magnet generates a magnetic field up to $B = 0.57$ T with a nominal field for the regular operation of $B = 0.5$ T. Reduced and reversed-field runs are also expected to provide better coverage for lower-momentum particles and systematic studies, respectively.

The central barrel detectors are mounted inside the magnet and cover the full azimuthal angle and a pseudorapidity range $|\eta| < 1.5$. A detailed description of the MPD is presented in Ref. [11].

The trajectories and momenta of charged particles are measured in a large volume TPC. The TPC also provides particle identification by measuring their energy loss (dE/dx) in the operational gas (90% Ar and 10% CH_4), with a typical resolution of $\sim 6.5\%$ achieved in heavy-ion collisions. Up to 53 points are measured along the track trajectory to provide reliable momentum reconstruction and particle identification. The Fig. 2a) shows the momentum resolution for primary particles with more than 20 measured points in the TPC. In a wide momentum range, the resolution is $\sim 2 - 3\%$, deteriorating at lower momentum due to multiple scattering and at higher momentum due to limited spatial resolution. The right panel of the same figure shows the distribution of dE/dx signals reconstructed for charged particles as a function of momentum, where one can identify bands corresponding to electrons, pions, kaons and protons. The solid curves show the $\pm 2\sigma_{\text{TPC}}$ selections for different particle species. The TPC provides π/K and K/p separations within 2σ in the momentum range up to 0.7 GeVc and 1.2 GeVc, respectively.

A wall of TOF detectors follows the TPC in radius and consists of 28 modules (14 modules in φ and two modules in z-direction), each made of 10 Multi-gap Resistive Plate Chambers (MRPC). The TOF detector provides time-of-flight measurements for charged particles with a typical resolution of $\sim$ 80 ps. Together with the momentum and track length measurements in the TPC, it provides particle separation by mass^2 or velocity β, as shown in the Fig. 3a). The TOF detector extends the particle identification capabilities of the TPC to higher momenta, providing 2σ separation of π/K and K/p up to 1.5 GeVc and 2.5 GeVc, respectively. Only pion (proton) tracks with transverse momentum $p_{\text{T}} > 150\,(350)$ MeVc can reach the TOF for the nominal

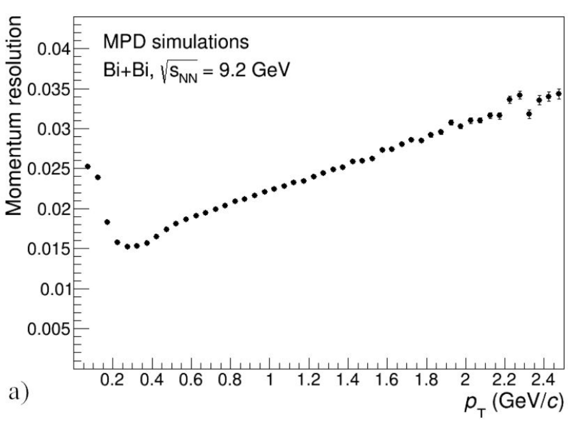

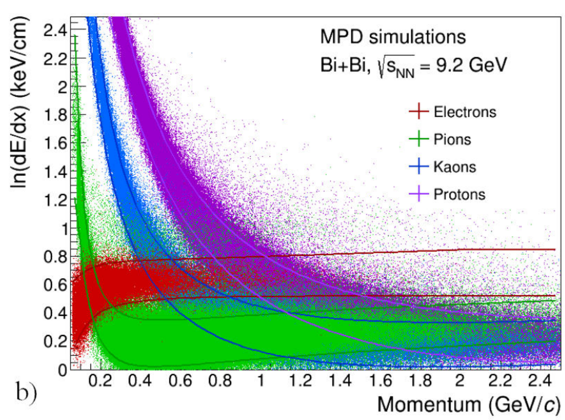

FIGURE 2. a) Momentum resolution for primary charged particles reconstructed in the TPC at midrapidity ($|\eta| < 1.0$) with number of points $n_{\text{hits}}^{\text{TPC}} > 20$. b) dE/dx signals for primary charged particles reconstructed in the TPC with number of points $n_{\text{hits}}^{\text{TPC}} > 20$. The bands of different colors correspond to $2\sigma_{\text{TPC}}$ selections for electrons, pions, kaons and (anti)protons. Simulation results are shown for Bi+Bi collisions at $\sqrt{s_{NN}} = 9.2$ GeV.

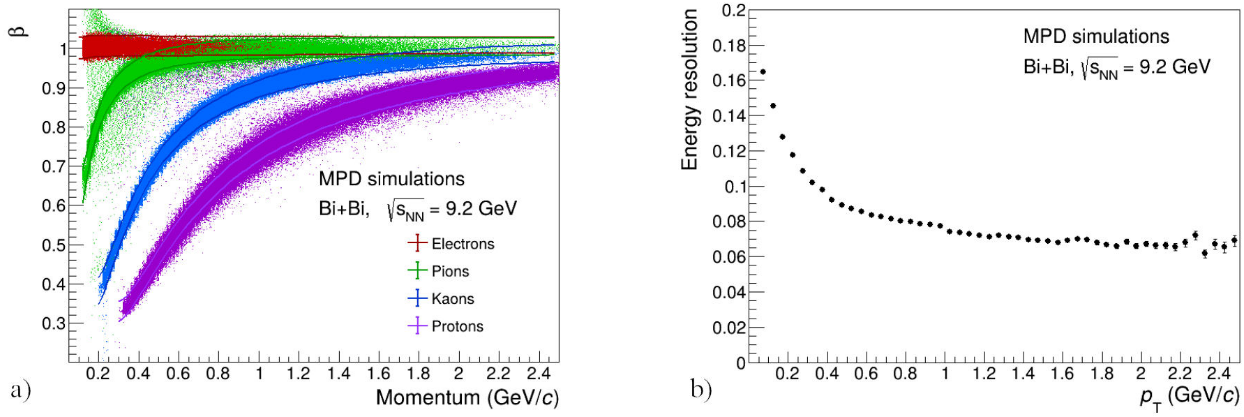

FIGURE 3. a) Particle velocities evaluated using combined measurements of momentum and track length in the TPC and time-of-flight in the TOF. The bands of different colors correspond to $2\sigma_{\rm TOF}$ selections for electrons, pions, kaons and (anti)protons. b) Energy resolution of the ECAL for primary photons. Results are shown for Bi+Bi collisions at $\sqrt{s_{NN}} = 9.2$ GeV.

magnetic field. At lower momenta, charged particle identification is only possible with the TPC.

The ECAL is the outermost detector, consisting of 38,400 shashlyk-type towers packed into 50 half-sectors (25 half-sectors in φ and 2 half-sectors in the z direction). It spans the full azimuthal angle and $|\eta| < 1.4$ in pseudorapidity. It is built with projective geometry; that is, the orientation of the tower varies in the z direction to ensure that the towers point approximately to the nominal interaction point (IP). The projective geometry of the ECAL is important for efficient registration of low-energy showers, which are the majority at NICA energies. The energy resolution of the ECAL estimated for photons in heavy-ion collisions is shown in the Fig. 3b). It is defined by the intrinsic resolution of the detector and is degraded by the cluster reconstruction procedure, which takes care of the shower reconstruction and of splitting of merged showers in high-multiplicity events. The electromagnetic calorimeter is the primary detector for measuring photons. It also helps to identify electrons at higher momenta, where TPC and TOF become less effective, requiring the E/p ratio to be close to unity, and where E and p are the measured electron energy and momentum, respectively.

The MPD is also equipped with two forward detectors for event triggering, measurement of event starting time (t_0), and estimation of collision centrality and geometry. The FFD consists of two identical detectors located at ± 140 cm from the nominal interaction point (IP). The detector covers the full azimuthal angle and $2.9 < |\eta| < 3.3$ in pseudorapidity. Each FFD consists of 80 Čerenkov quartz counters surrounding the beam pipe. Each counter has a 1 cm thick lead radiator to induce showers from photons produced in π^0-decays. In addition to the photons, the FFD detects fast charged particles. The time resolution of each counter is ~ 50 ps. By measuring the arrival times of the fastest particles (photons for most of the time) in the two arms ($t^{E}_{\rm FFD}$ and $t^{\rm W}_{\rm FFD}$), one can determine the event starting time and the event vertex

$$t_0^{\rm FFD} = \left(t^{\rm E}_{\rm FFD} + t^{\rm W}_{\rm FFD}\right)/2 - L/c,$$
$$z^{\rm FFD}_{\rm vertex} = c\left(t^{\rm E}_{\rm FFD} - t^{\rm W}_{\rm FFD}\right)/2, \quad (1)$$

respectively, where L is the distance from the nominal IP to the FFD along the beam axis and c is the speed of light. The resolution of the FFD, $t_0^{\rm FFD}$, depends on the number of channels N fired on each side by fast particles and is better than 50/$\sqrt{N}$ ps. However, the measured time resolution degrades to ~ 70 ps in peripheral events due to the spread in the arrival times of the incoming particles and becomes comparable to the TOF time resolution. The vertex resolution varies from 0.5 to 2 cm from central to peripheral collisions, respectively.

The FHCAL is designed to measure the fragments produced in the forward direction. They are located at a distance of $\pm$ 3.5 m from the nominal IP and cover 2π in azimuthal angle and $2 < |\eta| < 5$ in pseudo-rapidity. Each FHCAL calorimeter consists of 44 towers with a transverse size of 15×15 cm^2, covering in total about 1 m^2. Similarly to the FFD, the FHCAL can provide the start time and the event vertex position of each event. The typical time resolution of FHCAL modules is ~ 1 ns, making the $t_0^{\rm FHCAL}$ resolution inferior to that of the TOF and ECAL. Due to the hole occupied by the beam pipe, a significant part of the fragments escape detection, resulting in an ambiguity between the measured energy deposition and the centrality of the event. Various methods are being developed to resolve this ambiguity and to relate the measured energy deposition to the event centrality. The FHCAL is mainly used for event plane measurements at forward rapidity.

Collisions of Bi+Bi at $\sqrt{s_{NN}} = 9.2$ GeV are proposed as one of the first systems to be studied at NICA. A detailed description of the collider's operation parameters can be found in Ref. [13]. Each collider ring is about 503 m long and is filled with a maximum of 22 bunches, resulting in a time between bunches of about 75 ns. The collider luminosity at start-up is expected to be two orders of magnitude lower than the nominal one, corresponding to an event rate of $\sim$ 50 Hz. With a realistic estimate of the first run duration, we may expect around 50-100 million minimum bias collected events. Due to the incomplete optics of the collider rings, the vertex distribution in the MPD interaction region will be quite broad along the beam direction with $\sigma Z \sim$ 50 cm. This poses challenges for the trigger system and effective track reconstruction, but at the same time provides access to a wider rapidity coverage of the detector.

3. Data analysis framework

Physics feasibility studies were carried out using centralized Monte Carlo (MC) productions (listed in Table I) to ensure consistency of the results obtained by different groups and to provide a test of the existing computing and software infrastructure in preparation for real data analysis. Despite limited statistics, these productions are used to address a large number of observables using realistic data analysis techniques. A centralized data analysis framework, the so-called Data Analysis Train, was developed and implemented to process the simulated data samples with minimal load on disks, network, and CPU resources.

3.1. Event generators and centralized productions

A list of MC productions for physics feasibility studies is presented in Table I. Various event generators, such as the cascade version of UrQMD [14,15] the fragmentation model DCM-QGSM-SMM [16], the microscopic transport model PHQMD [17], hybrid models with QGP formation and hadronic phase PHSD [18,19] and vHLLE+UrQMD [20,21] were used to generate Bi+Bi collisions at $\sqrt{s_{NN}} = 9.2$ GeV. These models provide physically well-motivated scenarios for heavy-ion collisions at NICA energies. The choice of the event generator for a particular study was driven by the physics observable of interest and the range of measurements. For example, the UrQMD, PHSD and vHLLE+UrQMD event generators were used to study the production of light hadrons and (hyper) nuclei at midrapidity, while PHQMD and DCM-QGSM-SMM were also used to study the response of forward detectors, where realistic simulation of fragment production is important.

The generated events were used as input for the complete chain of realistic simulations of particle propagation through the detector materials, based on GEANT-4 [22]. In the calculations a uniform magnetic field of $B = 0.5$ T was used. The simulations of the detector subsystems and global tracking were performed using the MpdRoot [23] code, which is the official software of the MPD Collaboration. For all generators, the event vertex along the beam axis was smeared by a Gaussian function with $\sigma_{\text{z, vertex}} = 50$ cm. The impact parameter ranged within 0-16 fm, except for productions numbers 3 and 4, where it was set to 0-12 fm to enhance the statistics for (semi)central events.

The simulations were carried out using computational resources from the MLIT Multifunctional Information and Computing Complex (MICS), including the "Govorun" supercomputer and the VBLHEP computing farm "NICA" at JINR, united by the DIRAC platform [24-26].

TABLE I. The list of centralized MC productions for physics feasibility studies.

No.	Generator	Events	Purpose
1	UrQMD	50 M	General purpose
2	DCM-QGSM-SMM	1 M	Trigger
3	PHQMD	20 M	(Hyper)nuclei
4	PHSD	15 M	Global polarization
5	vHLLE+UrQMD	15 M	Flow, correlations

3.2. Analysis Train Framework

The analysis of large volumes of future and simulated real data samples ($\sim$ 10 PB) requires a coordinated effort on the part of the MPD Collaboration, which led to the implementation of the Analysis Train Framework (hereafter referred to as Train). Train users interested in running over a particular data set sign up for a pass over the data with their analysis modules. The analysis codes are checked into the MPD code management system (Git). The required input files are read-out once by the Train manager, and all analysis modules are sequentially run through the data. This approach reduces the number of input/output (I/O) operations and simplifies the storage architecture. The output files contain the required histograms and NTuples of small size and are stored on the local disks for further analysis.

The first modules in the Train are used to provide global information for all other physics analysis modules, such as event centrality and event plane orientation. In addition, special modules parametrize variables of common interest for each reconstructed track in terms of standard deviations, including the track matching to the primary vertex and outer detectors such as TOF and ECAL and the deviation of particle identification signals measured in the TPC and TOF from those expected for electrons, pions, kaons, protons, and light ions. The use of centralized parametrizations minimizes the amount of work required to start a new analysis and ensures a consistent approach throughout the MPD Collaboration. The Train architecture also simplifies the storage and sharing of analysis codes and methods. Most of the time, we are able to process the largest simulated datasets (50 M events) in 12 hours by running a Train with ~ 15 modules. A thousand jobs, each processing 50,000 events, are submitted with a total equivalent consumption of one year of CPU time. The number of events per job should not be too small to correctly fill the mixing pools for invariant-mass analyses. The first run of the Train took place in September 2023, with regular on-request runs since then.

4. Global event categorization

The global event quantities discussed in this section are the event centrality and the event plane, which characterize the geometry of heavy-ion collisions. These two observables provide basic information for more focused physics studies related to the onset of quark confinement, chiral symmetry restoration, and for the search of the CEP in the QCD phase diagram.

4.1. Trigger system and efficiency

The trigger system of the MPD experiment uses signals from three subsystems: FFD, FHCAL and TOF. The performance of the trigger system was studied using centralized productions numbers 2, see Table I.

The main trigger detector is the FFD. The trigger requires a signal in at least one channel on each side of the detector. The time difference between the signals generated in the east and west parts of the FFD are required to be within $|t^{\rm E}_{\rm FFD} - t^{\rm W}_{\rm FFD}| < 10$ ns. The high precision of the online vertex measurements with the FFD allows an effective suppression of background events from beam-gas and beam-pipe collisions and the selection of events close to the center of the interaction region.

The FHCAL produces fast signals from the energy deposition in the 44 modules per side, which can also be used for a trigger decision. Despite its modest time resolution of ~ 1 ns, which results in a primary vertex resolution of ~ 10 to ~ 30 cm from central to peripheral events, the FHCAL is still useful for background rejection.

The TOF subsystem generates a fast trigger signal for each of the 280 MRPCs that is hit by at least one particle. The TOF detects particles produced at central rapidity and is sensitive even to events with a small multiplicity. The actual threshold for the number of MRPCs fired in an event to make a trigger decision will depend on the noise conditions of the detector. The TOF will not be able to provide online information on collision time or vertex position.

Figure 4 shows the trigger efficiencies estimated for FFD, FHCAL and TOF as functions of the impact parameter and the event vertex for Bi+Bi collisions at $\sqrt{s_{NN}} = 9.2$ GeV. Since the background situation is not yet known, the efficiencies are shown for a different number of channels fired for each subsystem. All three subsystems show an efficiency of $\sim 100\%$ in central and semi-central Bi+Bi collisions, which decreases rapidly in peripheral collisions. The FHCAL and TOF subsystems show higher trigger efficiencies compared to those of the FFD. The trigger efficiency is not dependent on the position of the vertex in a wide range $|z_{\rm vertex}| < 140$ cm, making it possible to collect data in a wide range of vertices with the same efficiency.

The simulated response of the trigger system is not realistic for most of the productions in Table I because event generators such as UrQMD and PHSD do not simulate fragment production at forward rapidity. Therefore, the trigger efficiency estimates obtained in this section for FHCAL using the DCM-QGSM-SMM event generator were used as a benchmark for the performance of the MPD trigger system in all productions. The inefficiency of the trigger system was emulated for all productions by removing peripheral events according to the estimated dependence of the trigger efficiency on event track multiplicity, providing an overall efficiency of 91% for inelastic Bi+Bi collisions.

4.2. Event centrality

In heavy-ion collisions, the centrality of a collision is characterized by the impact parameter, which is the distance between the centers of the nuclei in the plane perpendicular to the beam axis. The impact parameter determines the overlap region of the nuclei.

In a nuclear collision event, the value of the impact parameter is not accessible experimentally. Therefore, events are usually classified into centrality classes using some measurable quantity like multiplicity, transverse energy measured in a predefined pseudo-rapidity interval, or the energy of fragments registered in a hadronic calorimeter. Each class corresponds to a percentile of the total inelastic nucleus-nucleus cross section and an average impact parameter that is obtained from some model, usually a Monte Carlo Glauber (MCG) model.

In this study, we used the centrality determined from the multiplicity of charged particles measured in the TPC at midrapidity, although alternative procedures can also be considered [11]. We consider such a procedure to be sufficient in the initial stage of MPD at NICA. However, in order to avoid possible autocorrelation effects, future centrality determination using the charged particle multiplicity measured in the TPC will be performed similarly to the procedure developed by STAR [27,28], *i.e.* by selecting centralities from a region different from the one used in the data analysis. The centrality was evaluated for events with a reconstructed vertex within $|z_{\rm vertex}| < 130$ cm. As shown in Sec. 4.1, the trigger efficiency remains constant in this range. A wider range would include collisions with vertices close to the FFD. Rather loose selection criteria were used for the reconstructed tracks: number of TPC hits $N^{\rm TPC}_{\rm hits} > 10$, transverse momentum $p_{\rm T} > 0.1$ GeVc, track matching to the primary vertex < 2 cm, and track pseudo-rapidity $|\eta| < 0.5$. Each track is corrected for the TPC reconstruction efficiency estimated as a function of the event $z_{\rm vertex}$ pseudo-rapidity of the track η. A typical multiplicity distribution is shown in Fig. 5.

The centrality of the event is estimated as a percentile of the total multiplicity with a maximum value of 91%. By definition, the reconstructed centrality distribution is flat between 0 and 91 %. The standard MCG model [29] was used to parametrize the reconstructed multiplicity distribution and estimate the geometrical parameters of the collisions. The impact parameter distribution of the MCG model was reweighted to reproduce the distributions modeled in the event generators listed in Table I.

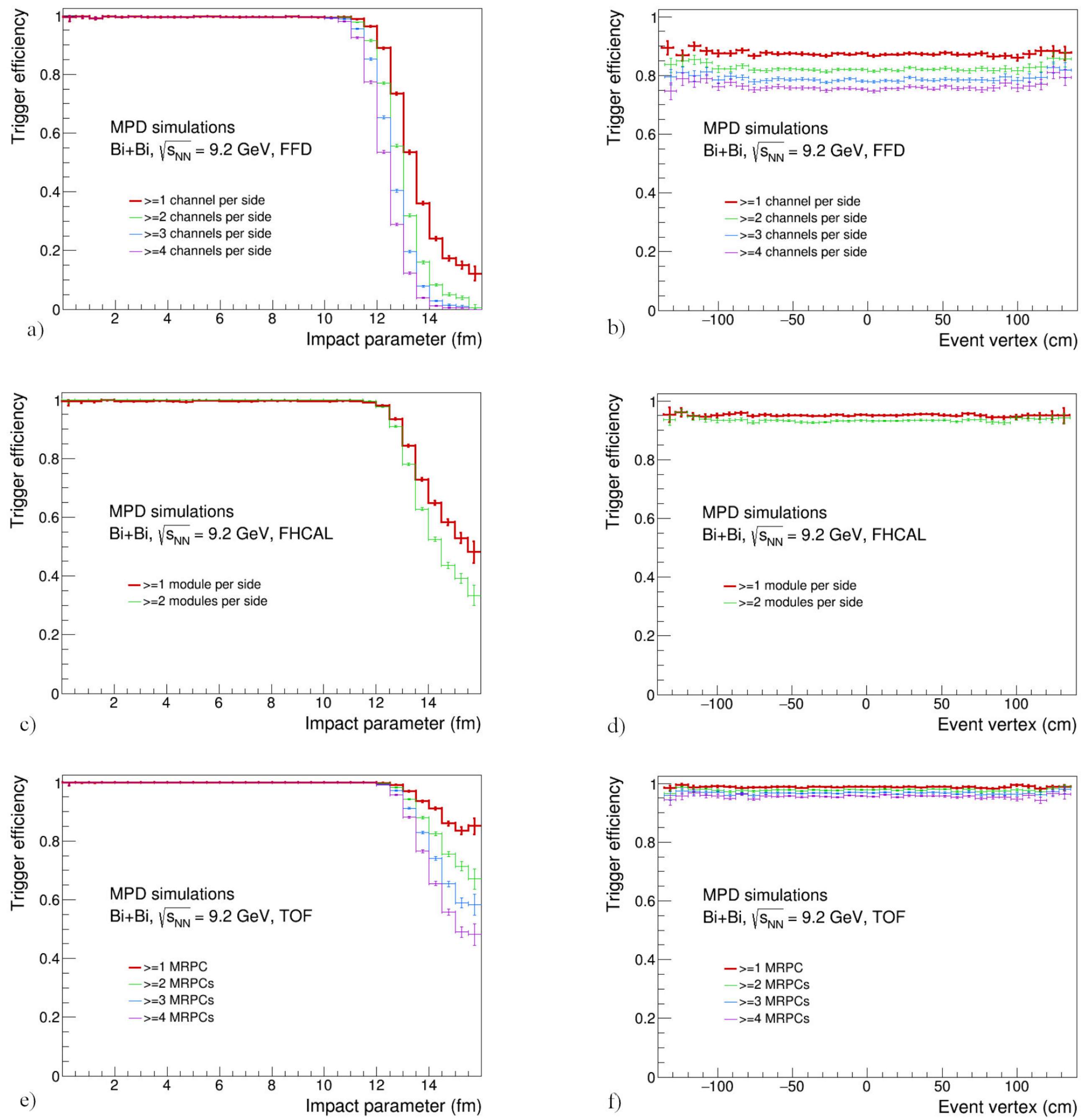

FIGURE 4. Trigger efficiency of the FFD (top), FHCAL (middle) and TOF (bottom) detectors estimated as a function of impact parameter with no z_{vertex} selections (left) and event z_{vertex} with no centrality selection (right) for Bi+Bi collisions at $\sqrt{s_{NN}} = 9.2$ GeV.

Within the MCG model, the multiplicity distribution of particles is modeled as the sum of particles produced from a set of independent emitting sources (N_{a}), each of which produces particles according to a negative binominal distribution NBD(μ, k). The number of emitting sources is parametrized as

$$N_{\text{a}} = fN_{\text{part}} + (1-f)N_{\text{coll}}, \quad (2)$$

where N_{part} and N_{coll} are the number of participating nucleons and the number of inelastic binary nucleon-nucleon collisions, respectively. The parameters μ, k and f are varied to minimize the χ^2/NDF of the description of the measured multiplicity distribution in the range $N_{\text{tracks}}^{\text{TPC}} > 10$. This range can be varied for a systematic study and, by default, was set to the minimal value corresponding to the saturation of the trigger efficiency.

The distribution, represented by the red markers in Fig. 5, shows the result of this procedure. A good agreement between the multiplicity distribution measured and MCG simulated in the overlap region can be observed. The ratio of the multiplicity distributions reconstructed and MCG is shown in the bottom part of the figure as an estimate of the trigger ef-

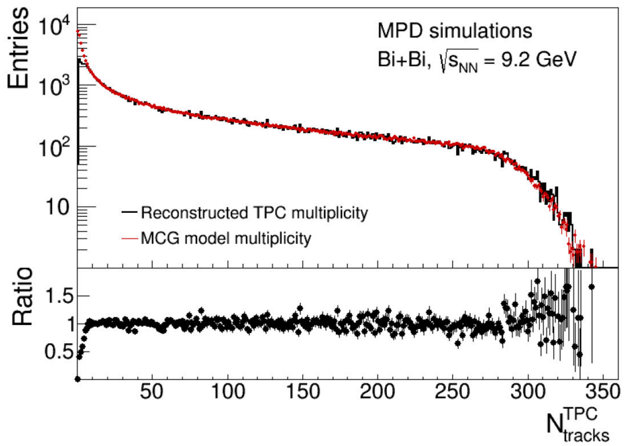

FIGURE 5. The reconstructed TPC (black) and MCG modeled (red) multiplicity distributions for Bi+Bi collisions at $\sqrt{s_{NN}} = 9.2$ GeV. The bottom part of the figure shows the ratio of the reconstructed and MCG modeled multiplicity distributions.

ficiency as a function of the event multiplicity. The weighted average efficiency estimated from the ratio is $\sim$ 90%, which is very close to the expected value of 91 %.

The MCG model is then used to estimate the initial geometry of the centrality classes. The values of the impact parameter, N_{part} and N_{coll} for 10% centrality intervals are evaluated for the UrQMD, DCM-QGSM-SMM, PHSD, and PHQMD event generators. Figure 6 shows the mean and RMS values with markers and error bars, respectively, evaluated for the impact parameter and N_{part}. The symbols for different event generators are shifted for visibility. Good agreement is found for the extracted values of the model parameters.

4.3. Event plane

The event plane method correlates the azimuthal angle ϕ of each particle with the azimuthal angle Ψ_n of the event plane determined from the anisotropic flow itself [30,31]. The event flow vector $Q_n = (Q_{n,x}, Q_{n,y})$ in the transverse (x, y) plane and the azimuthal angle of the event plane Ψ_n can be defined for each harmonic, n, of the Fourier expansion by

$$Q_{n,x} = \sum_{\text{k}=1}^{\text{M}} w_{\text{k}} \cos(\varphi_{\text{k}}),$$

$$Q_{n,y} = \sum_{\text{k}=1}^{\text{M}} w_{\text{k}} \sin(\varphi_{\text{k}}),$$

$$\Psi_n = \frac{1}{n} \tan^{-1}\left(\frac{Q_{n,y}}{Q_{n,x}}\right), \tag{3}$$

where M is the multiplicity of the particles k used in the calculation of the event plane, and φ_{k} and w_{k} are the laboratory azimuthal angle and the weight for the particle k, which is used, either to correct for the azimuthal anisotropy of the detector, or to account for the multiplicity of hadrons stopped in a particular cell of the segmented detector. The details of the estimation of w_{k} can be found in Ref. [30-32]. The reconstructed Ψ_n values can be used to measure the differential v_n flow coefficients of particles detected in the TPC ($|\eta| < 1.5$),

$$v_{\text{n}}(p_{\text{T}}, y) = \frac{\langle\cos(\text{n}(\phi - \Psi_n))\rangle}{R(\Psi_n)}, \tag{4}$$

where $R(\Psi_n)$ represents the event plane resolution factor and brackets denote the average over the particles and events. The 2-sub-event method with the extrapolation algorithm is used to estimate the $R(\Psi_n)$ factors [33].

Figure 7 shows the centrality dependence of the event plane resolution factor $R(\Psi_1)$ for directed v_1 flow measurements for Bi+Bi collisions at $\sqrt{s_{NN}} = 9.2$ GeV, simulated in production number 4 in Table I. Here, $\Psi_1 = \Psi_{1,\text{FHCAL}}$ is determined from the directed flow ($n = 1$) of particles detected in the FHCal ($2 < |\eta| < 5$).

The open symbols correspond to the $R(\Psi_1)$ values from the analysis of the fully reconstructed events 'reco', and the

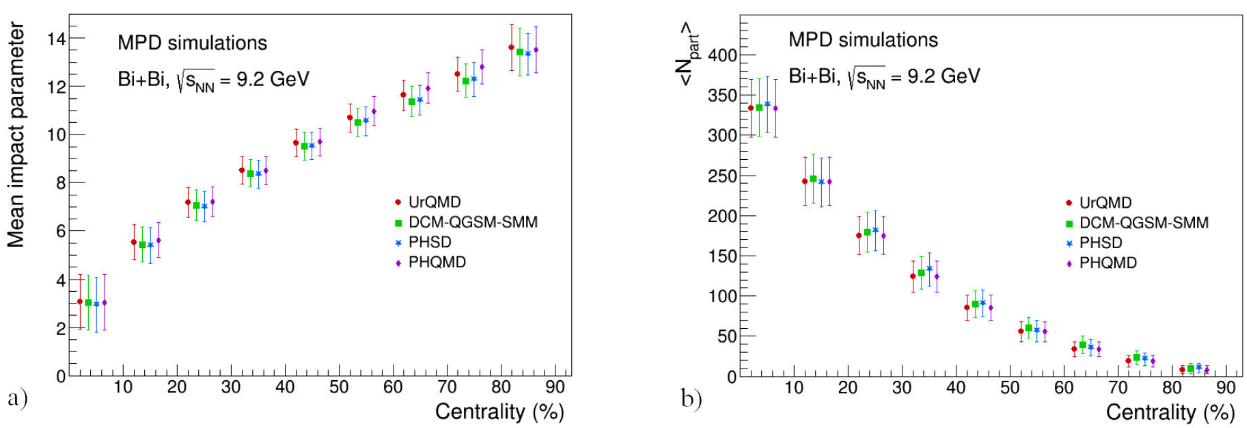

FIGURE 6. a) The value of the mean impact parameter for 10% centrality intervals estimated for Bi+Bi collisions at $\sqrt{s_{NN}} = 9.2$ GeV, modeled with the UrQMD, DCM-QGSM-SMM, PHSD, and PHQMD event generators. b) The same for the mean number of participants $\langle N_{\text{part}}\rangle$. The symbols are slightly shifted horizontally for better visibility.

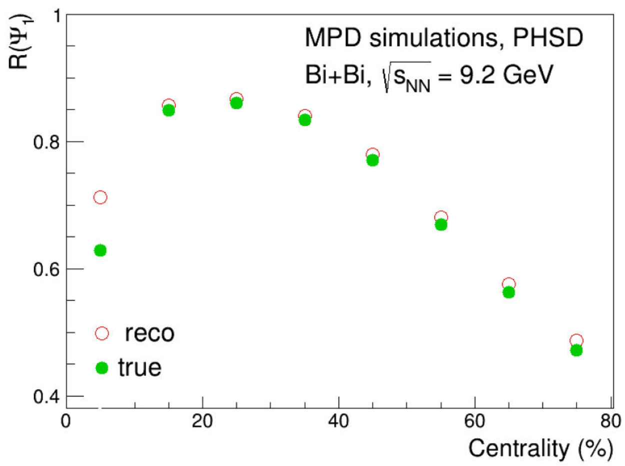

FIGURE 7. Centrality dependence of the event plane resolution factor $R(\Psi_1)$ for v_1 and P_Λ measurements in Bi+Bi collisions at $\sqrt{s_{NN}} = 9.2$ GeV, production 4 in Table I.

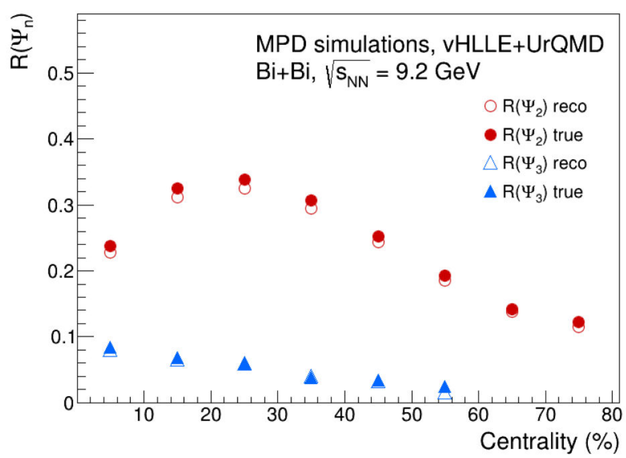

FIGURE 8. Centrality dependence of the event plane resolution factor $R(\Psi_\mathrm{n})$ for the second $n = 2$ (circles) and third $n = 3$ (triangles) order event planes constructed from the tracks of charged particles in the TPC. Open markers correspond to the reconstructed data, closed markers to the generated vHLLE+UrQMD model events.

closed symbols correspond to the results from the generated 'true' PHSD events. For midcentral events, the resolution factor $R(\Psi_1)$ is as large as 0.85 for v_1 and the global polarization P_Λ of Λ hyperon [34] measurements.

Figure 8 shows the centrality dependence of the event plane resolution factor $R(\Psi_\mathrm{n})$ for elliptic (v_2) and triangular (v_3) flow measurements for Bi+Bi collisions at $\sqrt{s_{NN}} = 9.2$ GeV. Here, the flow vectors $Q_\mathrm{n} = Q_{n,\mathrm{TPC}}$ and the azimuthal angle of the event plane $\Psi_n = \Psi_{n,\mathrm{TPC}}$ are constructed from the charged particle tracks reconstructed in the TPC ($|\eta| < 1.5$) [32].

The open markers correspond to $R(\Psi_\mathrm{n})$ values from the analysis of fully reconstructed vHLLE+UrQMD events (production 5 in Table I) and the closed markers to results from the generated events. The difference in the resolution factors for different flow harmonics reflects the observed ordering at NICA energies: $v_1 > v_2 > v_3$. The details of the extraction of collective flow parameters of different species are discussed in Sec. 5.

5. Physics performance studies

In this section, we present selected results of physics feasibility studies for the MPD experiment in Bi+Bi collisions at $\sqrt{s_{NN}} = 9.2$ GeV with emphasis on the measurements expected for the first years of MPD operation.

5.1. Light flavor hadron production

Light-flavored hadrons are plentifully produced and play an important role in understanding the physics of relativistic heavy-ion collisions. Experimental studies of charged-pion, kaon and (anti)proton spectra and yields are used to determine the properties of the hot and dense baryonic matter at the moment of its decay into final-state hadrons, allow testing of thermal and chemical equilibrium in the system, and provide insight into the underlying reaction dynamics by addressing the collective effects in the longitudinal and transverse expansion of the fireball. The shapes of particle p_T distributions and $\langle p_\mathrm{T}\rangle$ probe the reaction dynamics and are sensitive to particle production mechanisms in different kinematic regions, and to the interplay of the radial flow and parton recombination at intermediate transverse momenta. Measurements of hadrons containing strange quarks allow one to study the strangeness enhancement in heavy-ion collisions. Studying the strangeness enhancement of particles with open and hidden strangeness provides much more details of the strangeness production mechanisms. The production of short-lived resonances with lifetimes comparable to the fireball lifetime is measured to study the rescattering and regeneration processes in a dense hadronic medium.

5.1.1. Yields of charged pions, kaons and (anti)protons

The present analysis of charged-hadron yields uses data of production number 3 from Table I. To select events, we apply a primary vertex position cut of $|z_\mathrm{vertex}| < 100$ cm. To minimize contamination of secondary tracks, the Distance of Closest Approach (DCA) from the track to the collision vertex is taken to be less than 3 cm. To select tracks with good momentum and dE/dx resolution and to reject split tracks, it is required that the number of TPC points associated with the track be greater than 20. The center-of-mass rapidity and transverse momentum windows, to perform the analysis, are $|y| < 1.1$ and $0.05 < p_\mathrm{T} < 2.5$ GeVc, respectively. Two different approaches have been used for the identification of charged hadrons.

Approach 1 Signals in the TPC and TOF are required for each charged particle track to be accepted, and particle identification is achieved by a combination of energy loss dE/dx and time-of-flight measurements. This approach provides the best purity of the measured signals [see Fig. 9b)], but limits

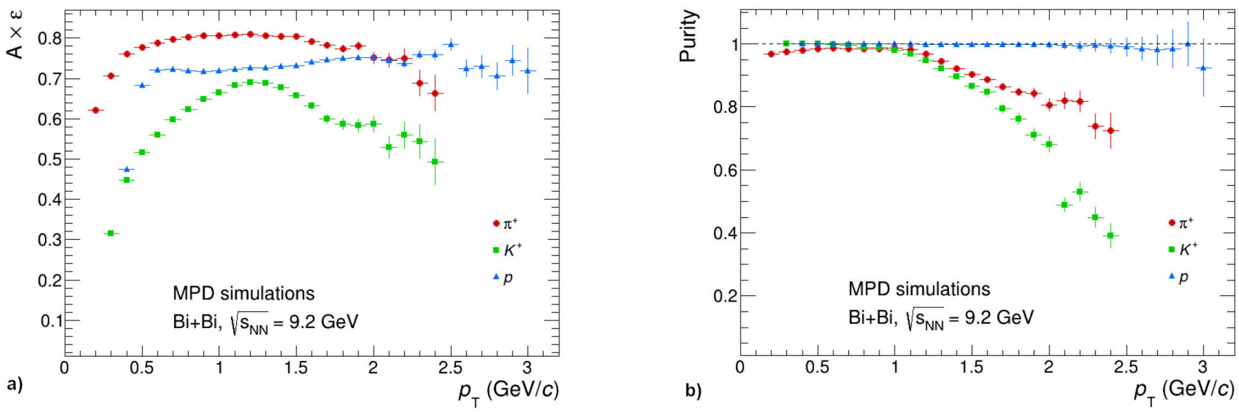

FIGURE 9. a) Overall efficiency for positively charged hadrons as a function of p_{T} in Approach 1. b) Purity for positively charged hadrons as a function of p_{T}.

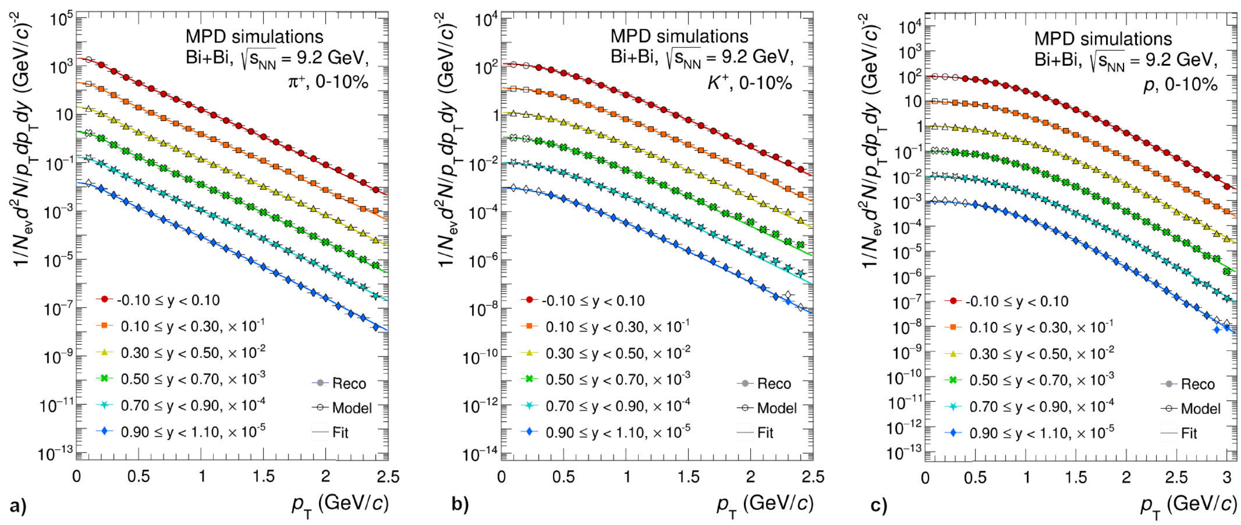

FIGURE 10. Invariant p_{T}-spectra of π^{+} a), K^{+} b) and p c) in several rapidity intervals for 0-10% central Bi+Bi collisions. The reconstructed data are shown by filled symbols while the model data are depicted by open symbols. Fits to invariant spectra are shown by lines (see text for details).

the measurement ranges at low p_{T} due to limited acceptance of the TOF, see Sec 2. The raw yields of the measured hadrons are corrected for reconstruction efficiency [see Fig. 9a)], which accounts for hadron misidentification, reconstruction losses, geometrical acceptance, and contamination from secondary interactions in the detector material and from weak decays of hyperons (relevant for pions and protons). The yields of charged hadrons are divided into centrality classes (0-10%, 10-20%, 20-30%, 30-40%, 40-80%) and in several rapidity intervals. As an example, Fig. 10 shows the comparison of the transverse momentum spectra of positively charged pions (left panel), kaons (central panel), and protons (right panel) reconstructed in 0-10% central Bi+Bi collisions to the generated ones. The comparison of spectra is shown in rapidity intervals of $\Delta y = 0.2$, where spectra are scaled down relative to the data at midrapidity by successive orders of ten for clarity. We found good agreement between the reconstructed and generated spectra in all cases.

In this approach, the MPD has limited p_{T} coverage at low transverse momenta, and to calculate the integrated yields one has to extrapolate the spectra to an unexplored p_{T}-range. To do this, the spectra are approximated with appropriate functional forms. The yield of pions is enhanced at low p_{T} due to a contribution from resonance decays, thus a sum of two exponentials in m_{T} (thermal function) is used. The kaon distributions are well described with a thermal function, while for protons a Blast-Wave motivated function [35] is used. The contribution of the extrapolation region varies for different species of particles but does not exceed 5%, 10%, and 15% for pions, kaons, and protons, respectively. The rapidity density distributions (dN_{ch}/dy) of positively charged hadrons (π^{+}, K^{+}, p), obtained by integrating the transverse momentum spectra in Fig. 10, are shown in Fig. 11, where the reconstructed data are shown with symbols, while the spectra at generator level are shown by lines. The measurements for pions and kaons cover approximately 65% of the total phase space and the rapidity distributions can be approximated by a

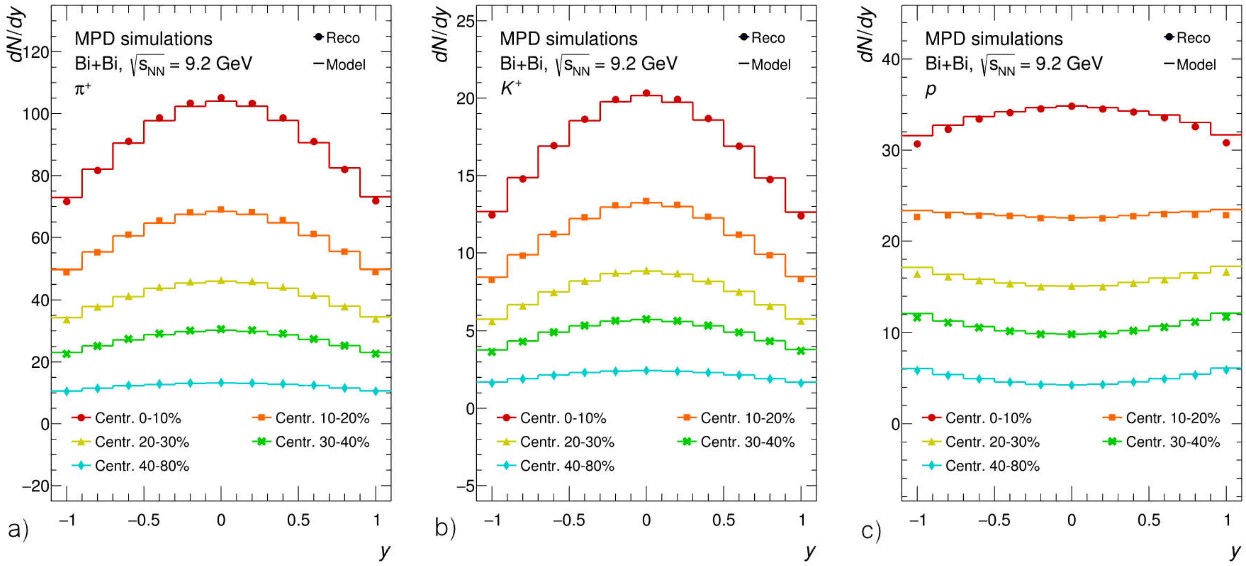

FIGURE 11. Rapidity distributions of a) π^+, b) K$^+$ and c) p in Bi+Bi collisions in different centrality classes. The reconstructed data are shown by symbols while the spectra at generator level are depicted by lines.

Gaussian. Thus, an integrated mean total multiplicity of π, K can be obtained with $\sim$ 10% uncertainty. The situation for protons is more difficult because the shape of their rapidity distributions changes with centrality. The MPD phase space coverage for protons is not sufficient to reconstruct the total (4π) yield of protons without model assumptions that can accurately predict the proton yields near the beam rapidity.

Approach 2 In this case, hadron spectra are measured separately using the particle identification capabilities of the TPC or TOF, and then combined by switching from one to another at a given p_T value. Spectra based on the identification of the TPC ("TPC spectra") consist of particles that are: 1) identified in the TPC within two standard deviations $2\sigma_{TPC}(p_T)$ and not consistent with signals expected for other species within $3\sigma_{TPC}(p_T)$; 2) identified in the TOF within two standard deviations $2\sigma_{TOF}(p_T)$ if the track is matched to TOF. Similarly, spectra based on identification of the TOF ("TOF spectra") consist of particles that are: 1) identified in TOF within two standard deviations $2\sigma_{TOF}(p_T)$ and not consistent with signals expected for other species within $3\sigma_{TOF}(p_T)$; 2) identified in TPC within two standard deviations $2\sigma_{TPC}(p_T)$. The spectra are reconstructed in the momentum ranges where the signal purity exceeds 95%. The main advantage of this approach is that it provides access to measurements of identified hadrons down to as low a transverse momentum as is possible with the existing track reconstruction algorithms in MpdRoot [23]: $p_T > 100$, 150 and 200 MeVc for $\pi^\pm$, K$^\pm$ and $p(\overline{p})$, respectively. The disadvantage is limited coverage at higher momenta due to the imposed strict requirements of high signal purity.

For charged pions, the veto requirement for other species keeps the signal purity close to $\sim 100\%$ throughout the momentum range, but limits the measurement range to $p_T <$ 1 GeVc in both TPC and TOF. For charged kaons, the requirement for high signal purity limits the measurements to $p_T < 0.45(1.5)$ GeVc with TPC (TOF). At higher momenta, the purity of kaons decreases rapidly as a result of the admixture of pions. The proton measurements with TPC or TOF are limited by the veto requirement to $p_T < 1.0$ GeVc and $p_T < 4.0$ GeVc, respectively. The situation is more complicated for antiprotons because of the high baryon asymmetry at NICA energies. The main contamination of the sample of identified antiprotons comes from the backscattered protons, which are misidentified as antiprotons due to an incorrectly determined momentum direction. The purity requirement limits the TPC measurements for antiprotons to transverse momenta from 0.2 GeVc to 0.9 GeVc. Since the TOF has no acceptance for low-p_T protons, measurements with the TOF are not affected by proton contamination. However, the admixture of kaons limits the measurements of the TOF to $p_T < 1.2$ GeVc.

The raw yields ($N^{\rm a}_{\rm raw}$), obtained for particles of type a (a stands for charged pions, kaons or (anti)protons) in different intervals of transverse momentum, are corrected for the reconstruction efficiencies, estimated as a product of acceptance (A) and detector efficiency (ϵ), $A \times \epsilon = N^a_{\rm raw}/N^{\rm a}_{\rm gen}$, where $N^{\rm a}_{\rm gen}$ is the number of primary particles of a given type generated. The evaluated reconstruction efficiencies for the TPC and TOF depend on the particle transverse momentum and are on average a few tenths of a percent. The transition points from TPC-spectra to TOF-spectra are chosen based on an analysis of statistical uncertainties and are set equal to $p_T = 0.95$, 0.4 and 0.7 GeVc for charged pions, kaons, and (anti)protons, respectively.

The feed-down contributions from the decays of heavier hadrons do not exceed $5(10)\%$ for $\pi^+(\pi^-)$ at $p_T < 0.2$ GeVc and are negligible for charged kaons for all momenta. The corresponding contributions for $p(\overline{p})$ vary from 40% to 10% with transverse momentum, with Λ-hyperon decays giving the main contribution. The reconstructed proton yield is also

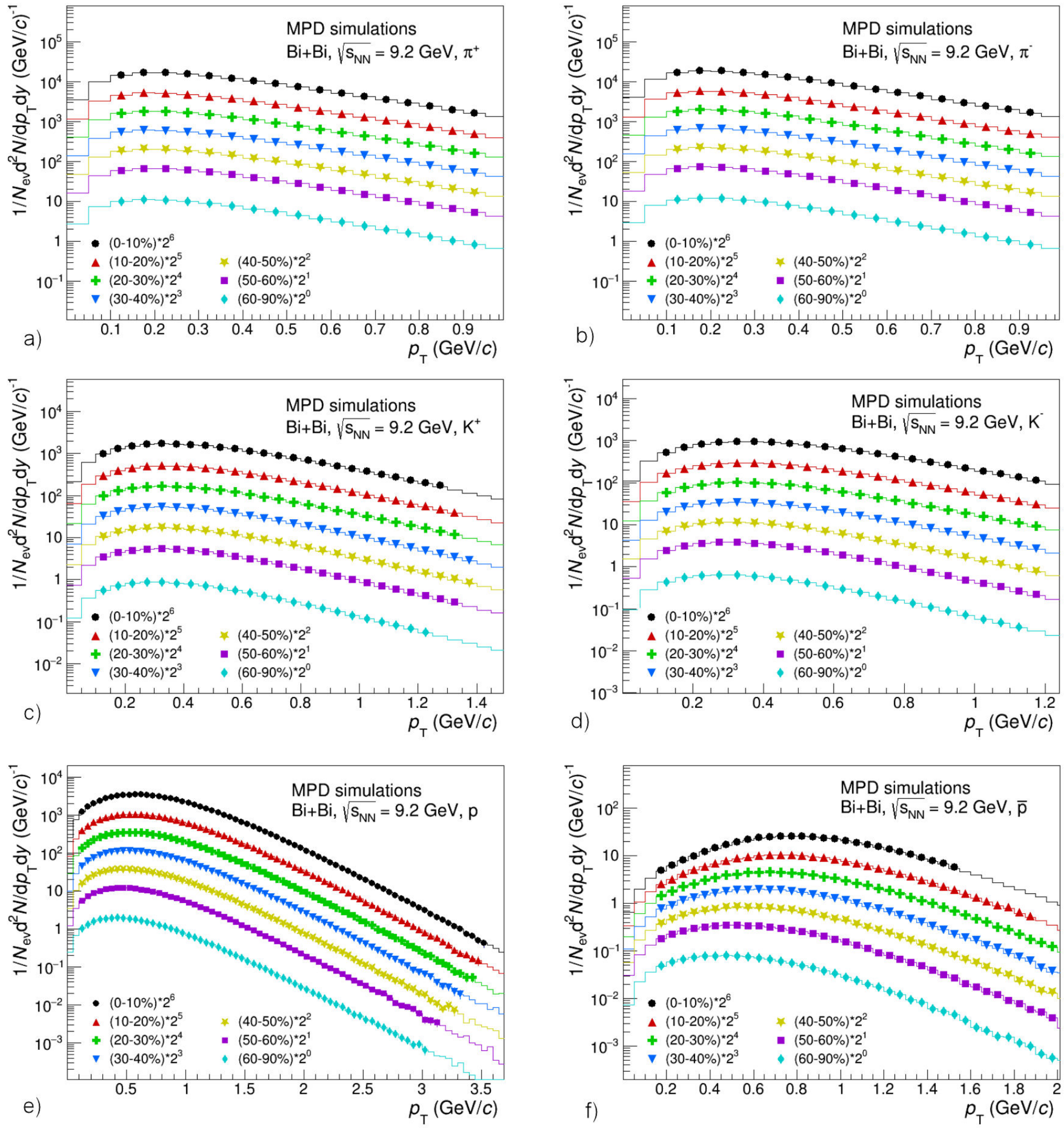

FIGURE 12. The reconstructed (markers) and generated (histograms) transverse momentum spectra for π^+, π^-, K^+, K^-, p and $\overline{p}$ for midcentral ($|y| < 0.5$) Bi+Bi collisions at $\sqrt{s_{NN}} = 9.2$ GeV in different centrality intervals.

significantly contaminated by protons produced in collisions with the beam pipe at $p_T < 0.2$ GeVc. As a result, measurements of the p and $\overline{p}$ spectra are limited to the momentum range $p_T > 0.2$ GeVc.

The fully corrected p_T spectra of charged pions, kaons, and (anti)protons, reconstructed with Approach 2 are shown in Fig. 12 for different centrality intervals. Within the measurement ranges, MPD samples 91% of the production of charged pions with 4% and 5% of the total yield in the unmeasured regions at low and high p_T, respectively. The situation is similar for charged kaons, for which MPD samples $> 93\%$ of the total yield with 1% and $< 7\%$ of the total yield unmeasured at low and high p_T. The best coverage is provided for protons for which more than 98% of the total yield is sampled in the detector with 2% of the remaining yield in the unmeasured region at low p_T. For antiprotons, MPD samples $> 92\%$ of the total yield with 2% and $< 6\%$ of the unmeasured yield at low and high p_T, respectively. The unmeasured yields can be recovered by extrapolating the fits to the measured spectra, similar to that described for Approach 1, with smaller uncertainties due to a wider coverage at low momentum.

The two approaches produce fully consistent results. The first approach provides p_T measurements in a wider momentum range but relies on purity corrections that are model dependent and can be quite significant at higher p_T. When analyzing real data, the corrections should be carefully evaluated in an iterative process by reweighting the particle differential yields in the event generators to the measured ones. However, this is the only possible approach to study the production of charged pions, kaons, and (anti)protons at intermediate and high p_T. The second approach limits p_T measurements to ranges where particle purity exceeds 95%, leaving little room for purity corrections and corresponding uncertainties, making the whole analysis more straightforward. Such measurements have better coverage at low p_T and are best suited to measure particle integrated yields.

5.1.2. *Hyperon reconstruction*

Since the energy threshold for strangeness production in the QGP phase is smaller than in the hadron gas phase, an enhanced production of strange particles (kaons and hyperons) was proposed as a signature of the transition to QGP [36]. Relative strangeness production, tested via the K/π ratio, was observed to be enhanced in central heavy-ion collision at the CERN SPS energies [37]. For hyperons, an increase in the production rate was observed with respect to elementary $p+p$ reactions in a broad energy range [38-40], stronger for particles with larger strangeness content. However, there are other possible explanations for the observed strangeness enhancement such as multi-meson reactions in dense nuclear matter [41], partial chiral symmetry restoration [42], vanishing of the canonical suppression with increasing multiplicity [43] or calculations within the core-corona approach [44]. In addition to the yields, the p_T distributions of the hyperons provide important information on the reaction dynamics.

Due to their small hadronic reaction cross sections, multi-strange hadrons cannot effectively pick up collective flow during the fireball evolution. Therefore, the transverse-momentum spectra of cascades reflect the initial conditions of a collision. The investigation of strange particle production as a function of beam energy and system size remains an essential part of the NICA research program.

Hyperon analysis is performed using the UrQMD event generator (first production in Table I). All events with the reconstructed vertex position within $|z_{\rm vertex}| < 130$ cm are used. Reconstruction of $\Lambda(\overline{\Lambda})$ is carried out using the V0 decay mode $\Lambda \rightarrow p + \pi^-$ ($\overline{\Lambda} \rightarrow \overline{p} + \pi^+$). For a given event, all possible pairs of (anti)protons and charged pions, having $N_{\rm hits}^{\rm TPC} > 20$ per track, are identified. For each pair, the point of closest approach of particle trajectories (*i.e.* a potential decay vertex) is then determined by extrapolating tracks back to the beam axis.

In order to reduce the background from random track crossings (combinatorial background), several cuts are imposed as explained in the text below and illustrated in Fig. 13. These cuts include: a) DCA of decay daughter particles to the

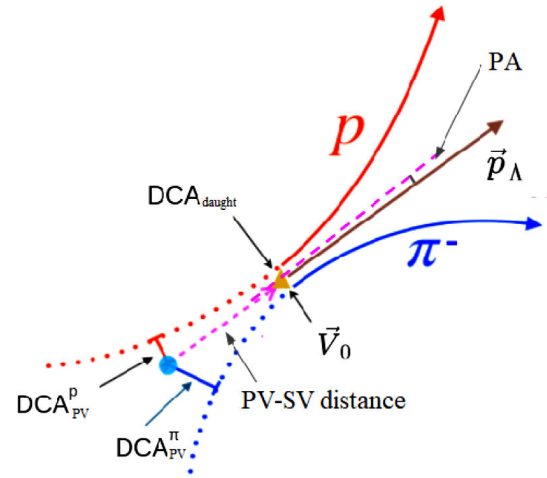

FIGURE 13. Topology of V0 decay shown for the case of $\Lambda \rightarrow p + \pi^-$.

primary vertex (DCA$_{\rm PV}$) - this cut is imposed in the χ^2-space, *i.e.*, after normalization to respective parameter errors; b) quality of the secondary vertex reconstruction ($\chi^2_{\rm vertex}$/NDF); c) DCA between the daughters in the secondary vertex (DCA$_{\rm daught}$); d) the distance between the primary and secondary vertices (PV-SV Distance); e) the value of the pointing angle (PA), defined as the angle between the reconstructed parent particle momentum vector and the line connecting the primary and secondary vertices. The selection criteria have been optimized to achieve the best significance, defined as $S/(S+B)$, where S is the hyperon signal and B is the background under the signal peak. The actual values of the topological cut parameters for $\Lambda(\bar{\Lambda})$ are given in Table II. For each selected pair of daughter particles, the invariant mass of the parent hyperon is calculated. Figure 14 shows the invariant mass distribution for the pairs $p\pi^-$ (left panel) and $\overline{p}\pi^+$ (right panel). In order to extract the raw signal, the background under the peak region has to be estimated. For this purpose, a combined fit of a Gaussian for the signal and a second-order polynomial function for the background is applied. The raw hyperon yields are determined by bin counting in the $\pm 5\sigma$ interval around the measured peak position with subsequent subtraction of the polynomial function integral estimated for the same invariant mass range. The resulting hyperon yield is then corrected for the reconstruction efficiency ($A \times \epsilon$, see Fig. 15), which accounts for signal

TABLE II. Selection criteria for Λ and $\bar{\Lambda}$ reconstruction.

Selection	Λ	$\overline{\Lambda}$
DCA$_{\rm PV}$ (cm)	$> 4.0(\pi^-)$	$> 4.0(\pi^+)$
	$> 2.5(p)$	$> 1.5(\overline{p})$
$\chi^2_{\rm vertex}$/NDF	< 1.75	< 1.75
DCA$_{\rm daught}$ (cm)	< 3.0	< 2.8
PV-SV Distance (cm)	> 2.0	> 2.0
PA (radians)	< 0.08	< 0.14

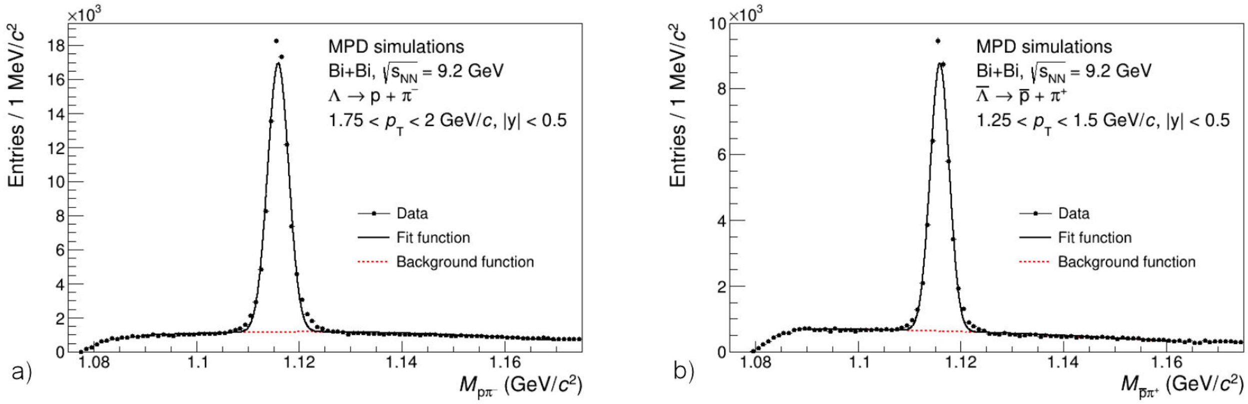

FIGURE 14. a) Invariant mass spectra of (p, π^-) pairs in the transverse momentum interval $1.75 < p_{\rm T} < 2$ GeVc. Reconstructed data are plotted by symbols, the result of a fit using a Gaussian plus a polynomial function of second order is shown by the line. b) Invariant mass spectra of $(\overline{p}, \pi^+)$ pairs in the transverse momentum interval $1.25 < p_{\rm T}$ <1.5 GeVc. Reconstructed data are plotted by symbols, the result of a fit using a Gaussian plus a polynomial function is shown by the line.

losses due to finite detector acceptance, track reconstruction efficiency, and the applied cuts

$$\frac{d^2N}{dydp_{\rm T}} = \frac{1}{N_{\rm ev}}\frac{N_{\rm raw}}{\Delta p_{\rm T}\Delta y}\frac{1}{A\times\epsilon}\frac{1}{\rm BR}, \qquad (5)$$

where $N_{\rm raw}$ is the number of reconstructed particles from the invariant mass distributions, $\Delta p_{\rm T}$ and Δy are the intervals in $p_{\rm T}$ and rapidity, $A \times \epsilon$ is the reconstruction efficiency, BR is the decay branching ratio and $N_{\rm ev}$ is the number of analyzed events in a given centrality interval.

The reconstruction efficiency for Λ as a function of $p_{\rm T}$ is shown in Fig. 15. We found small variations in $A \times \epsilon$ with the centrality of the collision. The reconstructed invariant transverse momentum spectra of Λ and $\overline{\Lambda}$, in centrality selected Bi+Bi collisions, are shown in Fig. 16. The distributions, reconstructed within the rapidity range $|y| < 0.5$, are shown with solid symbols, while the corresponding distributions, calculated at the generator level, are shown with empty symbols.

Both spectra agree within the uncertainties. Due to the very short time scale of the electromagnetic decay $\Sigma^0 \rightarrow \Lambda + \gamma$ ($\sim 10^{-19}$ s), the Λ-hyperons originating in decays of Σ^0 are experimentally indistinguishable from the primary Λ-hyperons. Therefore, the results for the yield of Λ and $\overline{\Lambda}$-hyperon represent the summed contribution from Λ and ($\Sigma^0 \rightarrow \Lambda + \gamma$), $\overline{\Lambda}$ and ($\overline{\Sigma}^0 \rightarrow \overline{\Lambda} + \gamma$), respectively. Corrections for feed-down from weak decays from multi-strange hyperons (Ξ and Ω) were estimated to be approximately 7% for Λ and 24% for $\bar{\Lambda}$. The feed-down contribution is slightly dependent on centrality and was subtracted using the model. The capability of the MPD detector to reconstruct $\Lambda(\overline{\Lambda})$, $\Xi^-(\bar{\Xi}^+)$ and $\Omega^-(\bar{\Omega}^+)$ hyperons in central Au + Au collisions at $\sqrt{s_{NN}} = 9$ GeV was investigated previously in Ref. [45] showing reasonable yields of these particles in 10 weeks of data taking with the expected operational luminosity. However, the yield of multi-strange antihyperons is very low at NICA energies, decreasing systematically with an increasing number of strange quarks. Therefore, in what follows for the 1st stage of heavy-ion collisions at NICA, we perform only an analysis of multi-strange hyperons. Once the Λ-hyperons are reconstructed, the cascade hyperons are reconstructed as well using the decay mode $\Xi^- \rightarrow \Lambda + \pi^-$. The candidate Λ for pairing with π^- is determined requiring the invariant mass to be within $\pm\ 5\sigma$ relative to the nominal value. To improve signal purity, topological selection criteria similar to (a)-(e) described above are applied (see Table III). For example, Fig. 17a) shows an invariant mass distribution for $\Lambda\pi^-$ pairs in the transverse momentum interval $1.0 < p_{\rm T} < 1.5$ GeVc. The reconstruction efficiency for Ξ^- as a function of $p_{\rm T}$ is shown in Fig. 15. In Fig. 17b) shows the reconstructed invariant $p_{\rm T}$ spectra of Ξ^- -hyperons in centrality selected Bi+Bi collisions. The difference between the reconstructed and the generator level spectra is small. The yield of Ω-hyperons in heavy-ion collisions is small, thus, the analysis was performed in a larger rapidity interval ($|y| < 1$) and for a wider centrality selection 0-80%. The selection criteria applied for Ω are given in Table III, the efficiency p_T-dependence is plotted in Fig. 15. In Fig. 18a) shows the

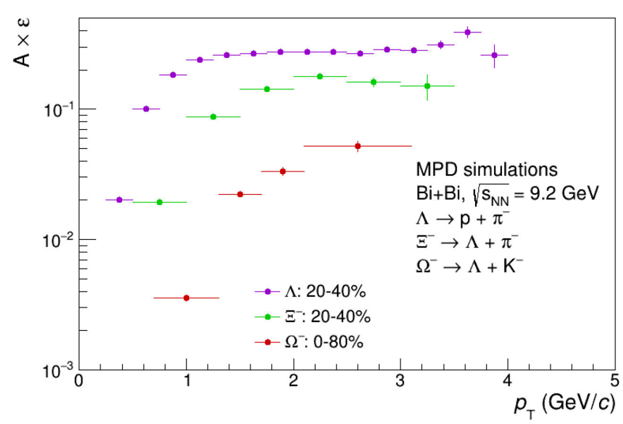

FIGURE 15. The reconstruction efficiency ($A \times \epsilon$) for Λ, Ξ, and Ω at midrapidity ($|\eta| < 0.5$) as functions of $p_{\rm T}$ in centrality selected Bi+Bi collisions.

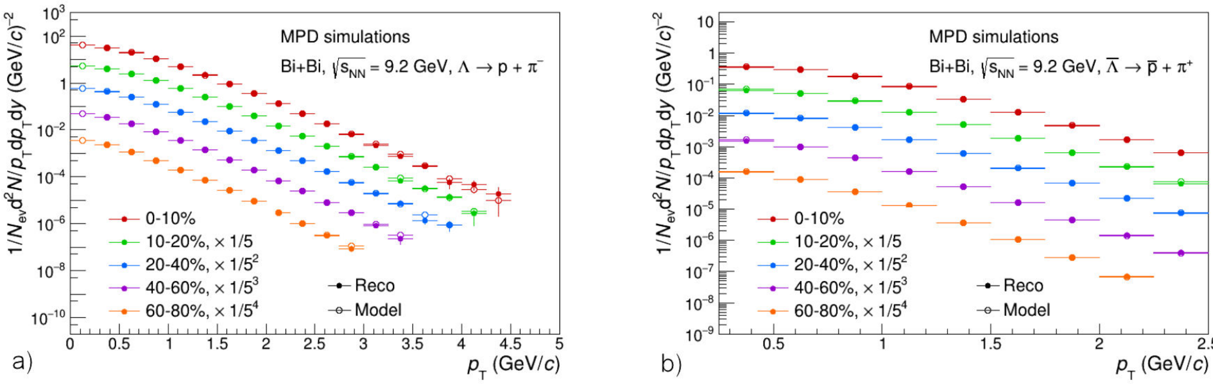

FIGURE 16. a) Midrapidity transverse momentum spectra of Λ in centrality selected Bi+Bicollisions. Reconstructed distributions are shown with solid symbols; empty symbols show the initially generated distributions from the model. b) The same for $\bar{\Lambda}$.

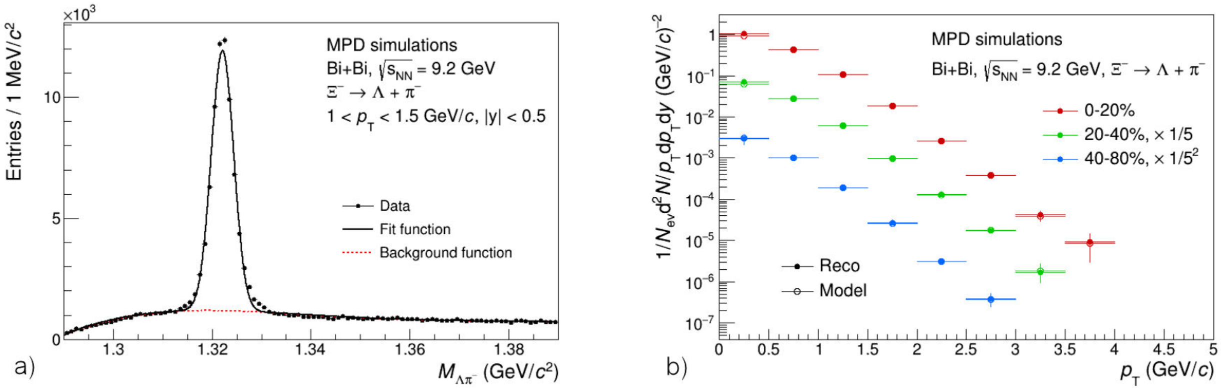

FIGURE 17. a) Invariant mass distribution for $\Lambda\pi^-$ pairs at $1.0 < p_T < 1.5$ GeVc. b) Midrapidity transverse momentum spectra of Ξ^- in centrality selected Bi+Bi collisions. Reconstructed distributions are shown with solid symbols; empty symbols show the initially generated distributions of the model.

TABLE III. Selection criteria used for Ξ^- and Ω^-.

Selection	Ξ^-	Ω^-
$\mathrm{DCA_{PV}}$ (cm)	$> 8.0(\pi^-)$	$> 7.5(\mathrm{K}^-)$
	$> 2.5(\Lambda)$	$> 4.0(\Lambda)$
$\mathrm{DCA_{daught}}$ (cm)	< 0.8	< 0.5
PV-SV Distance (cm)	> 1.0	> 1.0
PA (radians)	< 0.06	< 0.06

invariant shows the invariant mass distribution for (Λ, K^-) pairs in the p_T-interval $0.5 < p_\mathrm{T} < 1.3$ GeVc, while the right panel shows a good agreement of the reconstructed p_T-spectrum of Ω^- in Bi+Bi interactions with the spectrum obtained at generator level.

The hyperon feasibility study shows that measurements of $\Lambda(\bar{\Lambda})$ and Ξ are possible with a data set of several million events. Much larger data sets are needed to measure the production and centrality dependence of (multi-)strange hyperons at NICA energies.

5.1.3. Short-lived hadronic resonances

Measurements of short-lived hadronic resonances such as $\rho(770)^0$, K*(892), $\phi(1020)$, $\Sigma(1385)^\pm$ and $\Lambda(1520)$ at RHIC [46-52] and LHC [53-60] have been used to study enhanced strangeness production, dominant hadronization mechanisms, and vector meson spin alignment. However, resonances are most useful for studying the lifetime and properties of the late hadronic phase [61,62], which may distort signals of the crossover or the restoration of chiral symmetry transition. Measurements of resonance properties in heavy-ion collisions at $\sqrt{s_{NN}} = 7.7 - 5020$ GeV revealed that production of resonances with lifetimes $\tau < 20$ fm/c is suppressed in central collisions, while production of longer-lived resonances like $\phi(1020)$ remains almost unchanged from peripheral to central collisions. The observed modifications show a smooth evolution with the final-state charge particle multiplicity in different collision systems. The suppression of resonance yields in central heavy-ion collisions is explained by the rescattering of daughter particles in the hadronic phase. The modifications occur at multiplicities expected in (semi)central heavy-ion collisions at NICA energies [63]. The yield modifications are also predicted by cascade model calculations at NICA energies [64-66]. This provides a strong incentive for studying resonances in heavy-ion collisions at intermediate energies with the ultimate goal of achieving a comprehensive understanding of the hadronic phase.

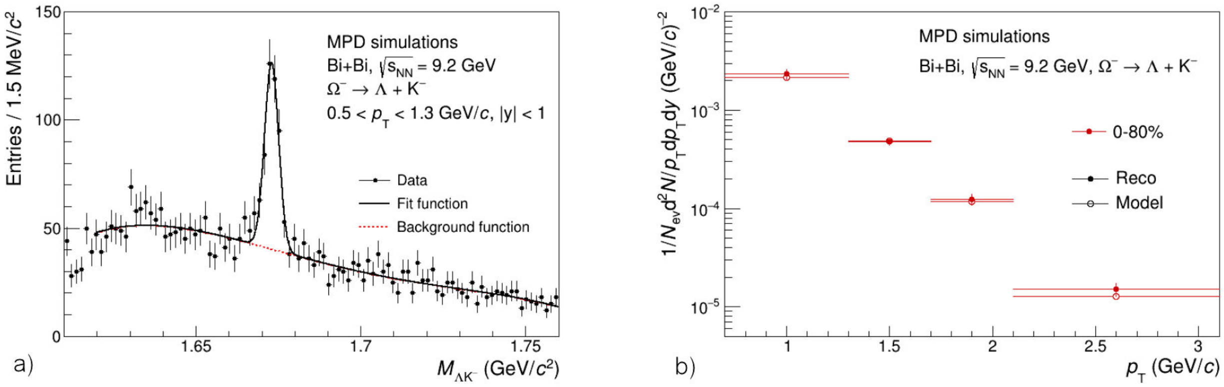

FIGURE 18. a) Invariant mass distribution for (Λ, K^-) pairs at $0.5 < p_\mathrm{T} < 1.3$ GeVc. b) Midrapidity transverse momentum spectrum of Ω^- in 0-80% central Bi+Bi collisions. Reconstructed distributions are shown with solid symbols, empty symbols show the initially generated distributions of the model.

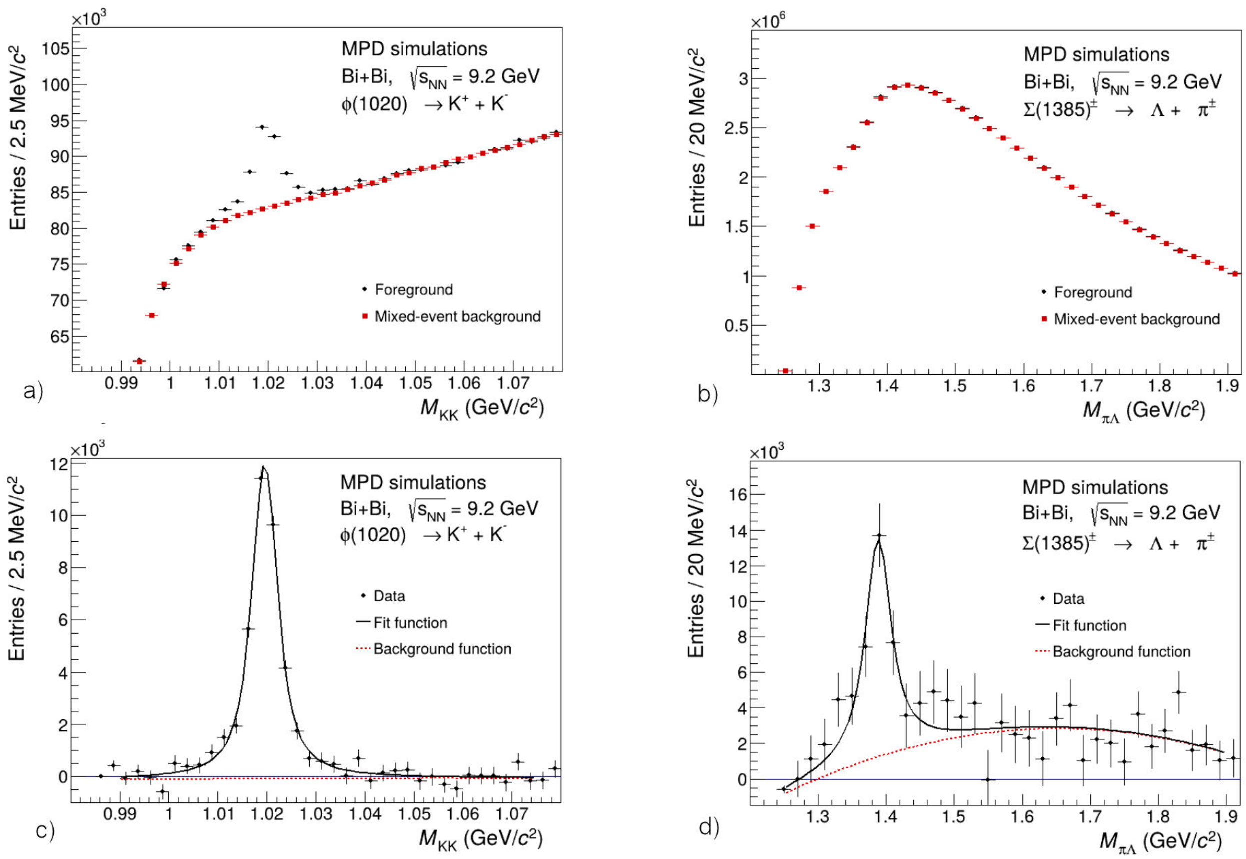

FIGURE 19. a) The invariant mass distributions for $\mathrm{K}^+\mathrm{K}^-$ and b) $\pi^\pm\Lambda$ pairs accumulated for the same and the mixed events in Bi+Bi collision at $\sqrt{s_{NN}} = 9.2$ GeV. The bottom panels show the distributions after subtraction of the mixed-event background. The resulting distributions are fit to a combination of a second-order polynomial and the Voitian function. Examples are shown for 0-10% central Bi+Bi collisions at $\sqrt{s_{NN}} = 9.2$ GeV in the transverse momentum interval 0.2-0.4 (0.4-0.6) GeVc for $\mathrm{K}^+\mathrm{K}^-$ ($\pi^\pm\Lambda$) pairs.

Production 1 of Table I was used to study MPD capabilities to reconstruct short-lived resonances in Bi+Bi collisions at $\sqrt{s_{NN}} = 9.2$ GeV. The UrQMD based simulation was used because this event generator provides reasonable description of the resonance yields and has the ability to stop resonance decay in the final state. This allowed for the decay of resonances in GEANT-4, which is necessary to evaluate the efficiency of the resonance reconstruction and the mass resolution of the detector. The reconstructed vertex had to be within $|z_\mathrm{vertex}| < 130$ cm, and only events with reconstructed centrality in the range 0-91% were accepted in the analysis. Charged daughter particles from resonance decays were treated as primary particles because the vertices of resonance decays are indistinguishable from the primary vertex.

TABLE IV. The topological selection used to reconstruct weak decays of K_s^0 and Λ.

Selection	K_s^0	Λ
χ^2_{vertex}/NDF	3.0	3.0
$\text{DCA}_{\text{daught}}$ (cm)	1.0	1.0
PV-SV Distance (cm)	0.5	0.5
PA (radians)	0.1	0.1
$\text{DCA}^{\pi}_{\text{PV}}$ (cm)	7	7
$\text{DCA}^{p}_{\text{PV}}$ (cm)	-	3

Such particles had to have at least 24 hits (out of a maximum of 53) reconstructed in the TPC and to match to the primary vertex within 3σ. Secondary particles from K_s^0 and Λ decays were required to have at least 10 hits in the TPC. Only tracks with $p_T > 0.1$ GeVc were accepted. The charged hadrons were identified by a 2σ cut in the value of $\langle dE/dx\rangle$ measured in the TPC. If the track was matched with the TOF, the track was additionally required to be identified by a 2σ cut on the measured value of particle velocity β.

The weakly decaying daughter particles ($K_s^0 \to \pi^+ + \pi^-$ and $\Lambda \to p + \pi^-$) were reconstructed by using the topological selections described in Sec. 5.1.2 and summarized in Table IV.

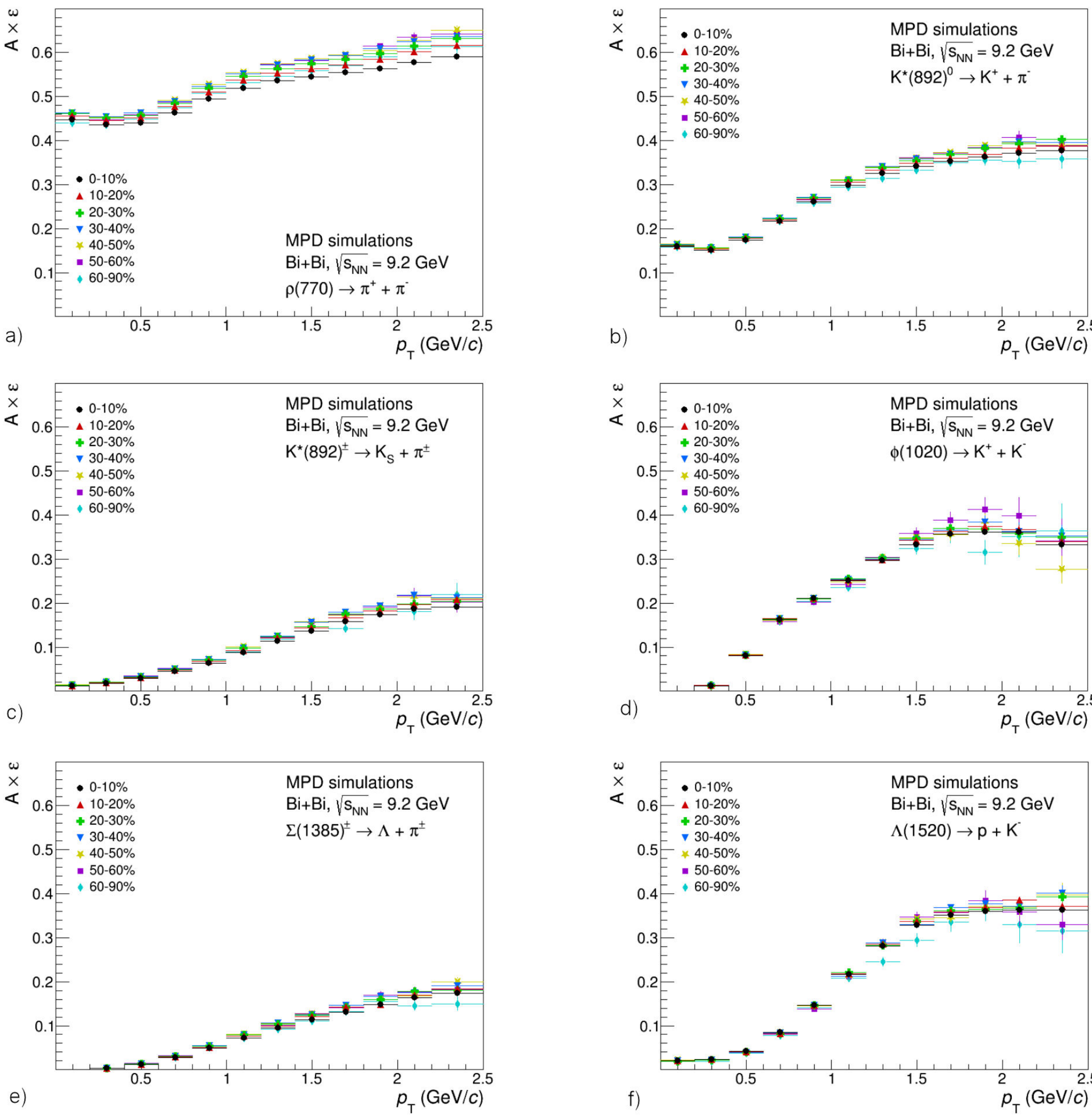

FIGURE 20. Reconstruction efficiencies evaluated for $\rho(770)^0$, $K^*(892)^0$, $K^*(892)^{\pm}$, $\phi(1020)$, $\Sigma(1385)^{\pm}$ and $\Lambda(1520)$ resonances at midrapidity ($|\eta| < 0.5$) as a function of transverse momentum in different centrality Bi+Bicollisions at $\sqrt{s_{NN}} = 9.2$ GeV.

The values were optimized to increase the significance of the reconstructed resonance signals. The pairs $\pi^+\pi^-$ and $p\,\pi^-$ were selected as candidates for K_s^0 and Λ if their reconstructed invariant masses were within 2σ of the expected values, where σ was parametrized as a function of the transverse momentum of the particle. The PDG [67] masses of daughter particles and the reconstructed momenta were used to measure the parent resonances. The candidate daughter particles are paired to accumulate $\mathrm{K}^+\mathrm{K}^-$, $\pi^+\pi^-$, $\pi^+\mathrm{K}^-$, $p\mathrm{K}^-$, $\pi^\pm\mathrm{K}_\mathrm{s}^0$ and $\pi^\pm\Lambda$ invariant mass distributions for different centrality intervals 0-10%, 10-20%, 20-30%, 30-40%, 40-50%, 50-60% and 60-90% at midrapidity $|y| < 0.5$. Examples of $\mathrm{K}^+\mathrm{K}^-$ and $\pi^\pm\Lambda$ invariant mass distributions, accumulated in 0-20% central Bi+Bi collisions at $\sqrt{s_{NN}} = 9.2$ GeV, are shown in the upper panels of Fig. 19 by black symbols.

The accumulated invariant mass distributions contain signals from resonance decays and combinatorial background. The uncorrelated combinatorial background is estimated using a mixed-event approach, where one of the daughter particles is taken for the same event and the other from another event with a similar multiplicity z_vertex and event plane. The invariant mass distributions of the mixed events are then scaled to the invariant mass distributions of the same events at higher masses and then subtracted. The invariant mass distributions of the mixed events are shown by the red symbols in Fig. 19. The distributions remaining after subtraction contain peaks from resonance decays and some remaining correlated background from jets and misreconstructed decays of heavier particles, as shown in the lower panels of Fig. 19.

The remaining background was found to be a smooth function of the mass in the neighborhood of the resonance peaks and can be described with a polynomial. To extract the resonance raw yields, the invariant-mass distributions are fitted to a combination of a second-order polynomial to describe the remaining background and a Voitian function (the Breit-Wigner function convolved with a Gaussian to account for the finite-mass resolution of the detector) for the signal. Examples of the fits are shown in the same plots. The mass resolution of the detector was estimated as a function of transverse momentum and collision centrality for each decay mode studied as the width of a Gaussian fit to the distribution with the difference between the generated and reconstructed resonance masses.

The efficiency of resonance reconstruction at midrapidity in the MPD setup was estimated as $A \times \epsilon = N_\mathrm{rec}/N_\mathrm{gen}$, where N_rec and N_gen are the number of reconstructed and generated resonances. The number of reconstructed resonances is determined after all event- and track-selection cuts, whereas the number of generated resonances accounts for the branching ratios of particular decay channels. The evaluated reconstruction efficiencies for the resonances $\rho(770)^0 \to \pi^+ + \pi^-$, $\mathrm{K}^*(892)^0 \to \mathrm{K}^+ + \pi^-$, $\mathrm{K}^*(892)^\pm \to \pi^\pm + \mathrm{K}_\mathrm{s}^0$, $\phi(1020) \to \mathrm{K}^+ + \mathrm{K}^-$, $\Sigma(1385)^\pm \to \pi^\pm + \Lambda$ and $\Lambda(1520) \to p + \mathrm{K}^-$ are shown in Fig. 20 as functions of transverse momentum and centrality in Bi+Bi collisions at $\sqrt{s_{NN}} = 9.2$ GeV. The estimated efficiencies are much smaller for resonance decays with weakly decaying daughters because more particles need to be reconstructed. The efficiencies decrease at low momentum, but most resonances can be measured from zero transverse momentum. The efficiencies show a modest dependence on event centrality; they are smaller in central collisions because of the higher detector occupancy.

The fully corrected transverse momentum spectra of $\rho(770)^0$, $\mathrm{K}^*(892)^0$, $\mathrm{K}^*(892)^\pm$, $\phi(1020)$, $\Sigma(1385)^\pm$ and $\Lambda(1520)$ resonances are calculated according to Eq. (5) and are shown with markers of different colors in Fig. 21 for different centrality intervals. The obtained spectra are compared to the generated ones, shown by histograms in the same plots. The reconstructed spectra are consistent with those generated within the statistical uncertainties, which confirms the consistency of the analysis chain. To study resonance production, as a function of centrality, a sample of about 10^8 Bi+Bi collisions at $\sqrt{s_{NN}} = 9.2$ GeV will be required. Most resonances, with the exception of $\phi(1020)$, can be measured starting from $p_\mathrm{T} = 0$, which is important to minimize systematic uncertainties in the integrated yield measurements needed for physics studies.

5.1.4. Light nuclei production

The study of the production of light nuclei is of particular interest in view of the puzzling fact that weakly bound objects are abundantly produced inside hot and dense hadronic matter. Light nuclei at near-midrapidity can be formed by coalescence of secondary nucleons located close to each other in space and having small relative momentum. Thus, the process of cluster formation is sensitive not only to the nucleon density in phase space but also to spatial-momentum correlations that appear in the collective velocity field during the fireball evolution. In order to obtain detailed information on the structure of the particle source, detailed measurements of the transverse momentum and rapidity distributions for clusters of different masses at several collision energies and centralities are necessary.

The performance of MPD for the light nuclei measurements was studied using mass production 3 from Table I. The used PHQMD model is a microscopic transport approach for the description of heavy-ion collisions including light (hyper)nuclei production [17]. Particle identification was achieved by combining information about particle energy losses measured in the TPC and time-of-flight measured in the TOF. The overall efficiency correction procedure is similar to that used in the analysis of hadrons (see Sec. 5.1.1 for details). The left panel of Fig. 22 shows the invariant p_T spectra of deuterons in centrality selected Bi+Bi collisions. Reconstructed data are shown by symbols; model distributions are depicted by histograms. Extrapolations to the unmeasured regions of transverse momentum are based on the Blast-Wave fit function (shown by dashed lines).

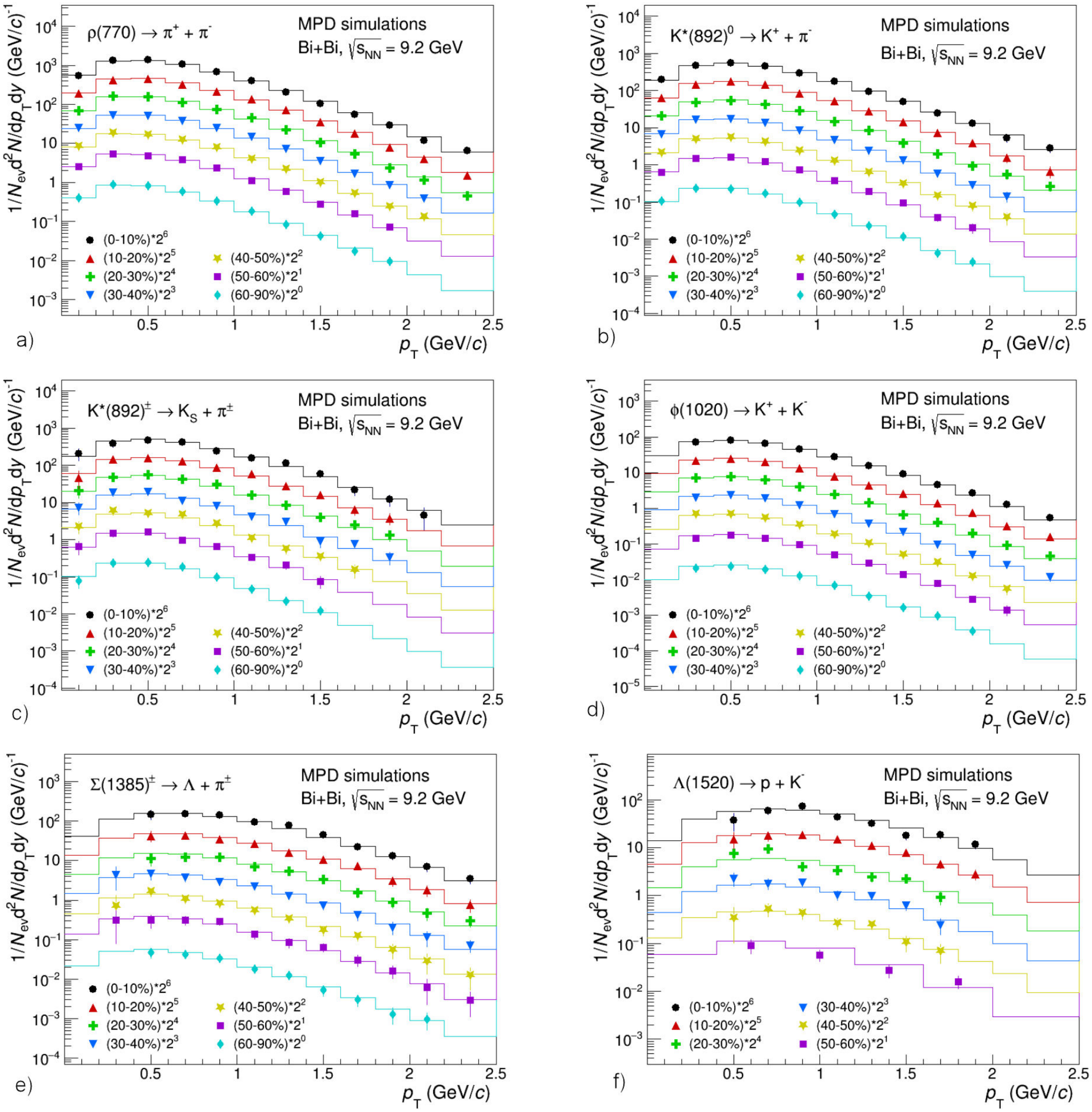

FIGURE 21. The reconstructed (markers) and generated (histograms) transverse momentum spectra for $\rho(770)^0$, $\mathrm{K}^*(892)^0$, $\mathrm{K}^*(892)^{\pm}$, $\phi(1020)$, $\Sigma(1385)^{\pm}$ and $\Lambda(1520)$ resonances for Bi+Bi collisions at $\sqrt{s_{NN}} = 9.2$ GeV in different centrality intervals.

Figure 22a) shows the rapidity distributions of reconstructed protons and light nuclei (d,^{3}He). As can be seen, the acceptance of the MPD allows measurements of cluster yields over the rapidity range $|y| < 1$.

5.1.5. *Hypernuclei*

Hypernuclei are bound nuclear systems consisting of nucleons and hyperons. Therefore, the process of their formation in heavy-ion collisions is determined by hyperon-nucleon correlations in the phase space of the reaction and the magnitude of the nucleon-hyperon potential [68]. The latter is of fundamental importance for astrophysics, since the appearance of hyperon degrees of freedom is expected in the interior of neutron stars [69]. New experimental data on the yields, binding energies, and lifetimes of hypernuclei can provide important information on the nature of the interaction between nucleons and hyperons in dense baryon matter. The NICA energy range is very well suited for such studies because the maximum in the freezeout baryon density and in the strangeness-to-entropy ratio is achieved within this range [70].

To study the MPD characteristics for hypernuclei reconstruction, data from mass production 3 from Table I were used. Reconstruction of hypertritons was carried out using the $^3_\Lambda\mathrm{H} \rightarrow {}^3\mathrm{He} + \pi^-$ decay mode. The daughter particles were

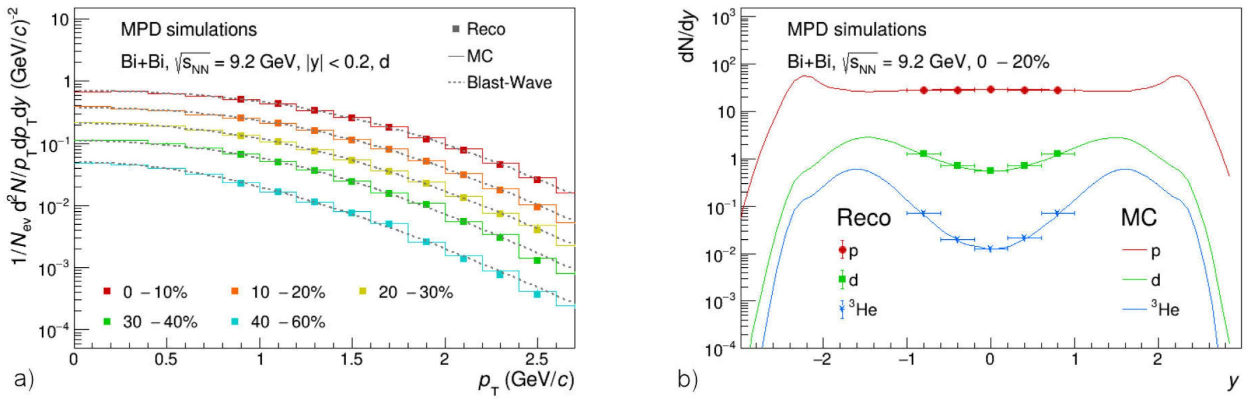

FIGURE 22. a) Invariant p_T-spectra of d in centrality selected Bi+Bi collisions. b) Rapidity distributions of p, d and ^{3}He in 0-20% central Bi+Bi collisions. The reconstructed data are shown by symbols while the model data are drawn by lines.

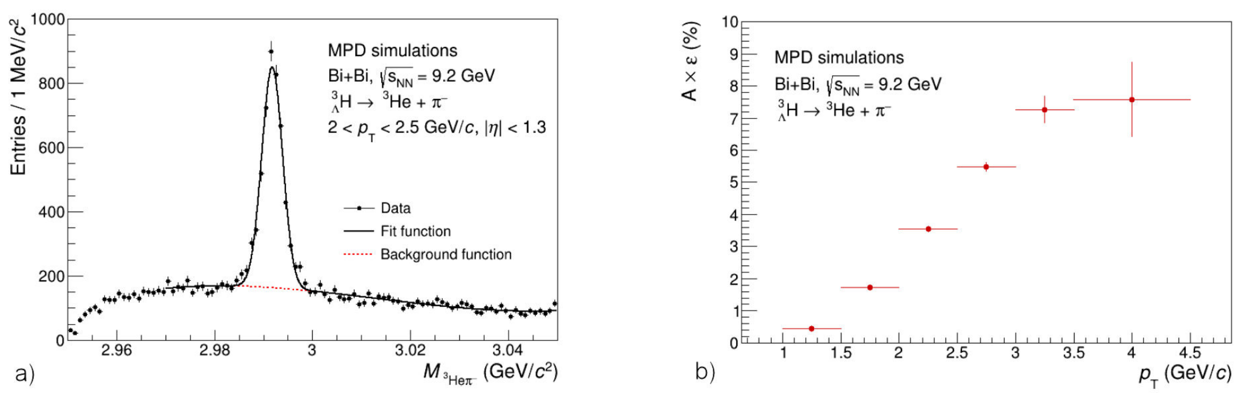

FIGURE 23. a) Invariant mass distribution for ^{3}Heπ^- pairs at $2.0 < p_T < 2.5$ GeVc. Reconstructed data are shown by symbols, the solid line indicates a fit to a Gaussian and a third order polynomial. b) The overall reconstruction efficiency for hypertritons in Bi+Bi collisions at midrapidity ($|\eta| < 0.5$).

identified using information on the ionization energy loss in the gas of the TPC and the mass squared from the TOF. The particle species is considered to be determined if the values of dE/dx and M^2 lie within $\pm 3\sigma$ of the values expected for true protons and pions. To reduce the combinatorial background, topological selections were applied to the reconstructed pairs, similar to those used in the reconstruction of hyperons in Sec. 5.1.2. The invariant mass spectrum of the ^{3}He π^- pairs that passed through each of the selection criteria is shown in Fig. 23a). The distribution was fitted by the sum of a Gaussian distribution for the signal and a third-order polynomial for the background. The signal was determined by histogram bin counting within a $\pm 5\sigma$ window of the Gaussian peak position and subtracting the integral of the background function in the same mass range. The raw yield of hypertritons is then corrected for the reconstruction efficiency, which includes the detector acceptance and signal losses due to the selection criteria and particle identification. The p_T dependence of the evaluated efficiency is shown in Fig. 23b).

Figure 24a) shows the invariant p_T-spectrum of hypertritons from Bi+Bi collisions as evaluated using Eq. (5). Spectra are obtained for the rapidity interval $|y| < 0.5$ without selecting the collision centrality. The reconstructed distribution is shown with solid symbols, while the initially generated distribution of the model is shown with empty symbols. As can be seen in the figure, the agreement between the reconstructed spectra is good for all p_T intervals.

According to the standard method of determining the lifetime, the yield of unstable particles in intervals of proper time τ decreases exponentially,

$$N(\tau) = N(0)\exp\left(-\frac{\tau}{\tau_0}\right) = N(0)\exp\left(-\frac{ML}{cp\tau_0}\right), \quad (6)$$

where the slope parameter τ_0 is the particle lifetime and $\tau = t/\gamma$ is the proper time, $\gamma = 1/\sqrt{1-(v/c)^2}$, with v the velocity, L the decay length, p the particle momentum and $M = 2.991$ GeV/c^2 the hypertriton rest mass [67]. The hypertriton yield was analyzed in several τ intervals in the range [0.1–1.5] ns. Figure 24b) shows the fully corrected hypertriton yields as a function of proper-time τ. A fit of the obtained distribution using Eq. (6) is shown as a line. The slope parameter (lifetime) of 265 ± 4 ps agrees well with the expected value of the lifetime used in the event generator, 263 ps.

According to simulation-based estimates of the MPD efficiency for hypertritons and model predictions on (hyper)-

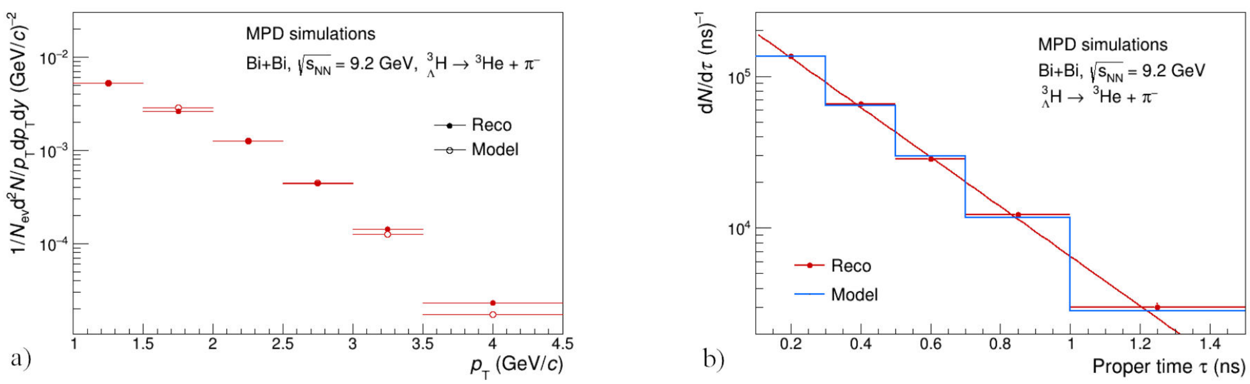

FIGURE 24. a) Invariant yield distribution for hypertritons. Reconstructed and generated data are shown with triangles and rectangles, respectively. b) Distribution of the number of hypertritons in intervals of proper time τ. The blue and red histograms represent the generated and reconstructed distributions, respectively, the line shows the fit according to Eq. (6).

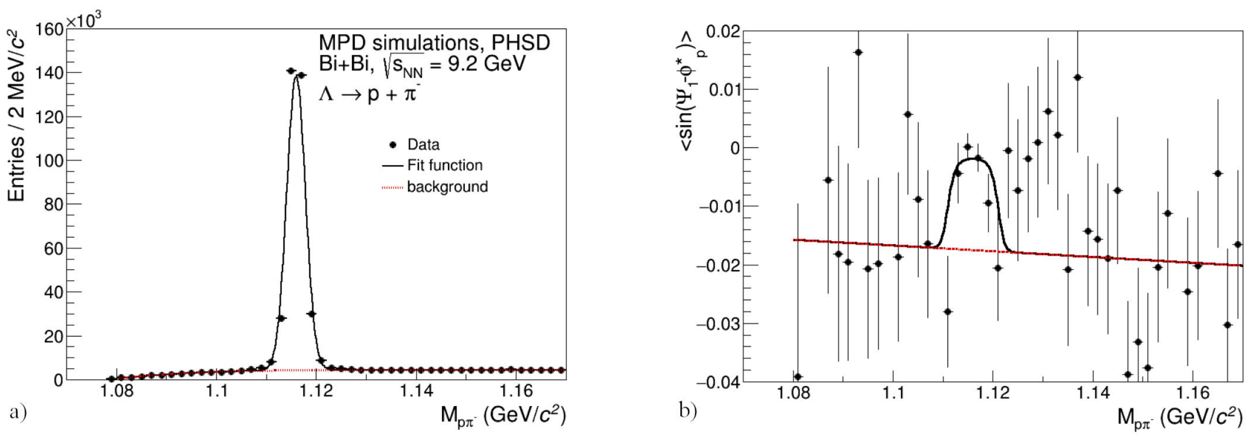

FIGURE 25. a) Invariant mass distribution and b) global polarization distribution $\langle\sin(\Psi_1-\phi_{\rm p}^*)\rangle(M_{{\rm p}\pi})$ for Λ particles at $0.5 < p_{\rm T} < 3$ GeVc for 20-50% central Bi+Bi collisions at $\sqrt{s_{NN}} = 9.2$ GeV. Reconstructed data are plotted by black symbols, the fit results are shown by the solid black line for the signal and red dotted line for background.

nuclei yields, about 10^3 hypertritons can be registered in one week of data collection of Bi+Bi collisions at $\sqrt{s_{NN}} = 9.2$ GeV with luminosity $L \approx 10^{25}$ cm^{-2}s^{-1}.

5.2. Hyperon global polarization

Global spin polarization (P_Λ) of Λ and $\overline{\Lambda}$ hyperons was found and measured in relativistic heavy-ion collisions over a broad collision energy range [71-73]. The data indicate a trend of increasing P_Λ with decreasing collision energy from 1-2% at $\sqrt{s_{NN}}$ = 200 GeV to 5-7% at $\sqrt{s_{NN}}$ = 3 GeV. Different scenarios for the global polarization mechanism are predicted by phenomenological [74,75] and MC hydrodynamic and transport models, highlighting the importance of collecting new experimental data [76,77]. Here we report on the MPD performance analysis of global polarization of Λ-hyperons. Data from mass production number 4 in Table I served as the basis for this study, since the hyperon global polarization was included in the PHSD model [78,79]. The procedure was developed in Ref. [34] to transfer the hyperon spin polarization signal from the transport code to the final moment distribution of particles after weak decays. This allowed us to investigate the reconstruction of the spin signal within the detector simulation. The global polarization observable P_Λ is defined as [71-73,80]

$$P_\Lambda = \frac{8}{\pi\alpha_\Lambda}\frac{\langle\sin(\Psi_1-\phi_{\rm p}^*)\rangle}{R(\Psi_1)}. \quad (7)$$

Here $\alpha_\Lambda = 0.732 \pm 0.014$ [67] is the Λ decay parameter, Ψ_1 the first-order event plane angle from FHCAL, $\phi_{\rm p}^*$ the azimuthal angle of the proton in the Λ rest frame, $R(\Psi_1)$ the resolution of the first-order event plane angle and the brackets denote the average over all produced Λ hyperons.

The protons and pions measured in the TPC were used to reconstruct Λ hyperons, which decay through $\Lambda \to p + \pi^-$ with a branching ratio of 63.9%. The Λ candidates have been reconstructed using the invariant mass technique.

The combinatorial background from uncorrelated particles has been reduced by the selection criteria based on the decay topology with quality assurance selections, such as the primary and secondary decay vertex positions, the DCA of the daughter particles to the primary vertex, the DCA of the mother particle to the primary vertex, and the DCA between the daughter tracks; see details in Sec. 5.1.2. As an example, the upper panel of Fig. 25 shows the invariant mass distribution for Λ-particles with $0.5 < p_{\rm T} < 3$ GeVc for 20-50% central Bi+Bi collisions at $\sqrt{s_{NN}} = 9.2$ GeV.

The background region is fitted with a second-order polynomial while the signal is fitted with a Gaussian distribution. From these fits, the background $f^{\rm B}(M_{\rm p\pi})$ and signal $f^{\rm S}(M_{\rm p\pi})$ fractions are extracted as functions of invariant mass. The selected sample $P_{\Lambda}^{\rm all} = \langle \sin(\Psi_1 - \phi_{\rm p}^*)\rangle(M_{\rm p\pi})$ contains both the signal $P_{\Lambda}^{\rm S} = \langle \sin(\Psi_1 - \phi_{\rm p}^*)\rangle^{\rm S}$ and the combinatorial background contribution $P_{\Lambda}^{\rm B}(M_{\rm p\pi}) = \langle \sin(\Psi_1 - \phi_{\rm p}^*)\rangle^{\rm B}(M_{\rm p\pi})$. The distribution $P_{\Lambda}(M_{\rm p\pi})$ is fitted as a function of invariant mass $M_{\rm p\pi}$ (invariant mass fit method) [71-73,80], according to

$$P_{\Lambda}^{\rm all}(M_{\rm p\pi}) = f^{\rm B}(M_{\rm p\pi})P_{\Lambda}^{\rm B}(M_{\rm p\pi}) + f^{\rm S}(M_{\rm p\pi})P_{\Lambda}^{S}, \quad (8)$$

to extract the signal contribution $P_{\Lambda}^{\rm S}$ to the measured polarization signal, see the bottom panel of Fig. 25. That is, the background $P_{\Lambda}^{\rm B}(M_{\rm p\pi})$ was parametrized as a linear function of $M_{\rm p\pi}$ and $P_{\Lambda}^{\rm S}$ is taken as a fit parameter. The choice of a linear function to describe $P_{\Lambda}^{\rm B}(M_{\rm p\pi})$ is based on the assumption that the background is a smooth function of the invariant mass [81], as well as on previous measurements of global polarization at various collision energies [82-84]. The results of fitting with different background estimation methods are consistent with each other within uncertainties, and the difference is treated as a systematic uncertainty. Figure 26 presents the resulting values of global polarization $P_{\Lambda} = P_{\Lambda}^{\rm S}/R(\Psi_1)$ as a function of centrality (upper panel) for Λ particles at $0.5 < p_{\rm T} < 3$ GeVc, as a function of transverse momentum $p_{\rm T}$ (central panel) and rapidity y (lower panel) for 20-50% central Bi+Bi collisions at $\sqrt{s_{NN}} = 9.2$ GeV. Good agreement is observed between the P_{Λ} results obtained from the analysis of fully reconstructed data 'Reco' and generated 'MC' PHSD model events. The statistics analyzed of 15 M events allow us to perform differential measurements of Λ global polarization in mid-central Bi+Bi collisions only. The more detailed $p_{\rm T}$-differential studies as a function of centrality and rapidity, as well as the measurements for $\bar{\Lambda}$-hyperons, will require a larger data sample of up to 200-300 M of minimum bias events.

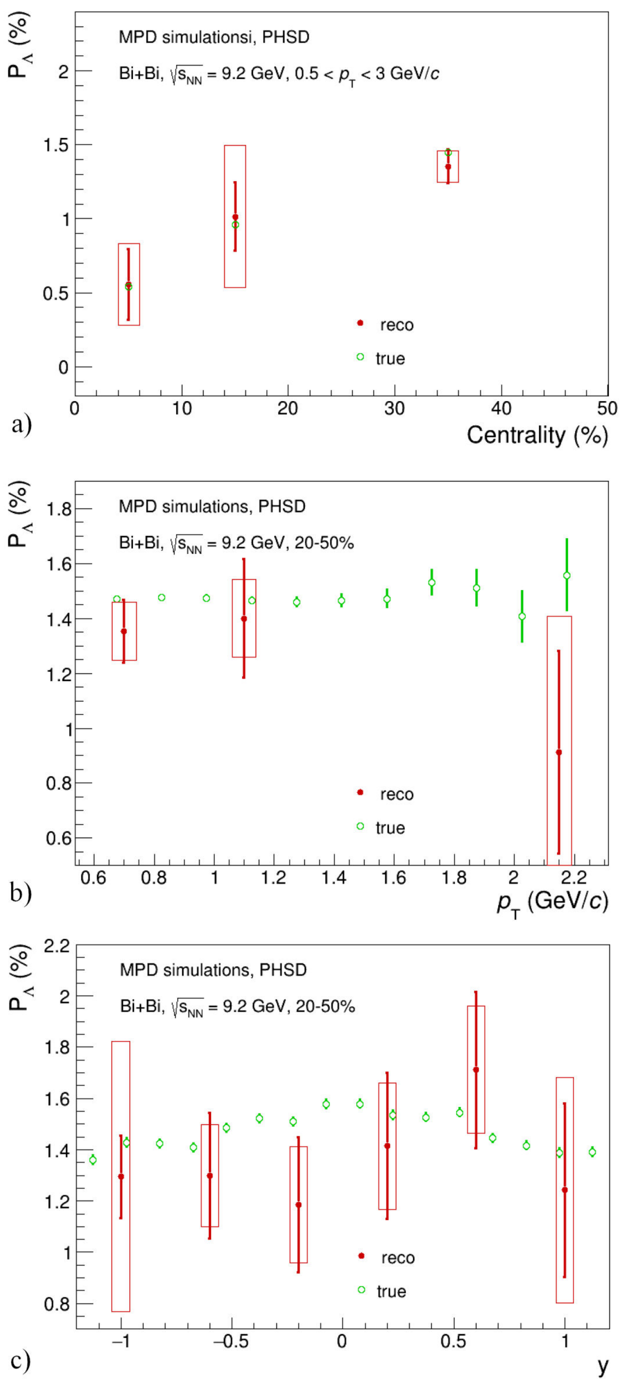

FIGURE 26. a) Global polarization of Λ as a function of centrality in Bi+Bi collisions at $\sqrt{s_{NN}} = 9.2$ GeV. b) The same as a function of $p_{\rm T}$. c) The same as a function of rapidity y. Open and closed markers correspond to generated and reconstructed data, respectively.

5.3. Anisotropic flow

The sensitivity of the azimuthal anisotropic collective flow to the equation of state (EoS) and the transport properties of strongly interacting matter makes it one of the promising observables in relativistic heavy-ion experiments [33,85-87].

The collective flow (assuming a perfect event plane resolution) is usually quantified by the Fourier coefficients $v_{\rm n}$ in the expansion of the particle azimuthal distribution relative to the collision symmetry plane given by the angle $\Psi_{\rm n}$ [33,85], see Sec. 4.3 for details. In this section, we discuss the anticipated performance of the MPD detector for differential measurements of the directed (v_1), elliptic (v_2) and triangular (v_3) flow of identified hadrons in Bi+Bi collisions at $\sqrt{s_{NN}} = 9.2$ GeV [11,30,31]. Although theoretical models can successfully describe flow observables at RHIC and LHC energies, none of them can quantitatively describe the existing $v_{\rm n}$ measurements in the NICA energy range $\sqrt{s_{NN}} = 4 - 11$ GeV [11]. Therefore, we have used two models (productions number 1 and 5 listed in Table I) to simulate minimum bias Bi+Bi collisions: the viscous hydro

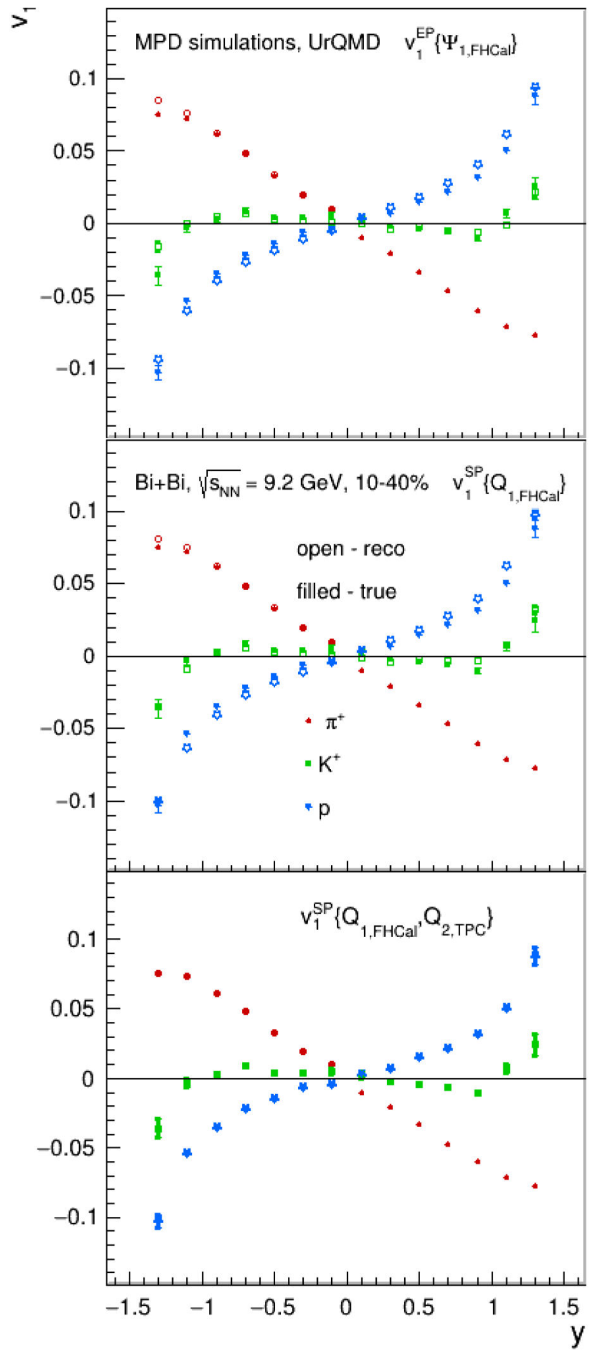

FIGURE 27. Directed flow $v_1(y)$ of identified charged hadrons as functions of rapidity in 10-40% central Bi+Bi collisions at $\sqrt{s_{NN}} = 9.2$ GeV for different methods of flow analysis of fully reconstructed events (filled markers) and generated UrQMD events (open markers).

+ hadronic cascade vHLLE+UrQMD hybrid model [20,21] with QGP formation and the cascade version of UrQMD [14,15], which is a purely hadronic transport model. The initial parameters of the vHLLE+UrQMD model were tuned for different collision energies in order to reproduce basic experimental bulk observables in the RHIC Beam Energy Scan: (pseudo)rapidity distributions, transverse momentum spectra, and elliptic flow coefficient for inclusive charged hadrons [20,21,88]. We refer to the v_n results obtained from the flow analysis of the generated model events as 'true', whereas 'reco' denotes the v_n results derived from the flow analysis of the fully reconstructed events.

Figure 27 shows the rapidity dependence of directed $v_1(y)$ flow of charged pions (triangles), kaons (boxes) and protons (circles) for 10-40% central Bi+Bi collisions at $\sqrt{s_{NN}} = 9.2$ GeV from the analysis of UrQMD model events. A momentum-dependent $\pm 2\sigma$ cut around each peak in the mass-squared mass^2 distribution was used to identify pions, kaons and protons. The figure shows results obtained with three different analysis methods with respect to the flow vector $Q_1 = Q_{1,\text{FHCAL}}$ of spectator fragments detected in FHCAL, the event plane method $v_1^{\text{EP}}(\Psi_{1,\text{FHCAL}})$ (upper panel), the scalar product method $v_1^{\text{SP}}(Q_{1,\text{FHCAL}})$ (middle panel), and the scalar product method using mixed harmonics $v_1^{\text{SP}}(Q_{1,\text{FHCAL}}, Q_{2,\text{TPC}})$ (lower panel). For all species of particles, the directed flow v_1 crosses zero at midrapidity and the reconstructed values 'reco' of v_1 (open symbols) are fully consistent with the generated 'true' values (filled symbols). Figure 28 shows the results of the p_{T}-differential elliptic-flow, v_2, measurements for charged pions (triangles), kaons (boxes) and protons (circles) in 10-40% central Bi+Bi collisions.

The large and uniform acceptance of the TPC allows us to use multiparticle methods, such as direct cumulants, for elliptic-flow measurements. The top panel of Fig. 28 shows the four-particle $v_2\{4\}$. The other panels show the two-particle methods: b) two particle cumulants $v_2\{2\}$, c) scalar product method using TPC tracks values for reconstructed and generated signals is observed for all particle species and flow analysis methods. Different flow measurement methods have different degrees of sensitivity to flow fluctuations and to so-called non-flow correlations [31,85,89]. They include transverse momentum conservation, small azimuthal angle correlations due to final-state interactions, resonance decays, and quantum correlations due to the Hanbury Brown–Twiss (HBT) effect [85].

The main cause of non-flow effects is few particle correlations, so estimates of the v_2 flow coefficients based on four-particle cumulants $v_2\{4\}$ have the benefit of great suppression of non-flow effects contribution. To suppress the non-flow effects in two-particle methods, we have applied the pseudo-rapidity gaps $\Delta\eta$ between sub-events: $|\Delta\eta| > 0.1$ between the two TPC sub-events for $v_2\{2\}$, $v_2^{\text{SP}}(Q_{2,\text{TPC}})$, $v_2^{\text{EP}}(\Psi_{2,\text{TPC}})$ and $|\Delta\eta| > 0.5$ between the TPC and the FHCAL detectors for $v_2^{\text{EP}}(\Psi_{1,\text{FHCAL}})$.

The residual contribution of non-flow correlations was found to be 1-7% for $p_T > 1.5$ GeV/c for the two-particle methods with $|\Delta\eta| > 0.1$ and it was found that it is negligible for the two-particle methods with $|\Delta\eta| > 0.5$ and the four-particle cumulant method.

Different flow measurement methods have different degrees of sensitivity to v_2 fluctuations σ_{v_2}: $\sigma_{v_2}^2 = \langle v_2^2\rangle - \langle v_2\rangle^2$. For a Gaussian model of fluctuations, one can expect [85]:

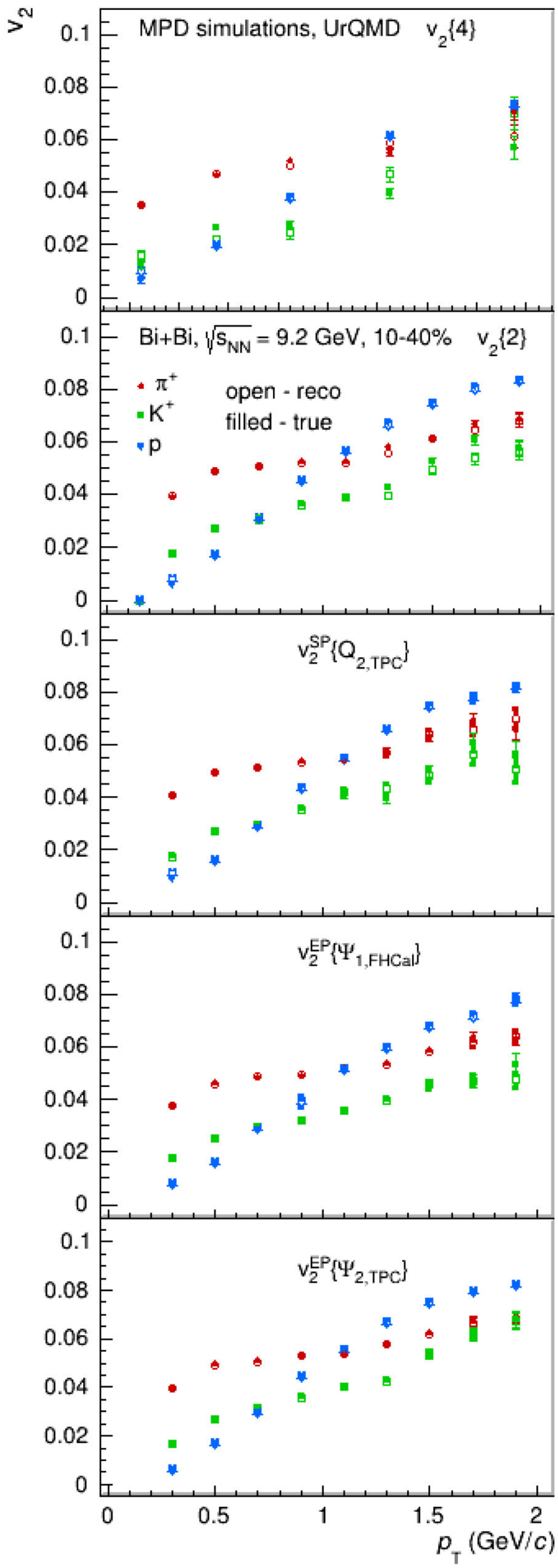

FIGURE 28. Elliptic flow $v_2(p_T)$ of identified charged hadrons as a function of p_T in 10-40% central Bi+Bi collisions at $\sqrt{s_{NN}} =$ 9.2 GeV for different methods of flow analysis of fully reconstructed events (filled markers) and generated UrQMD events (open markers).

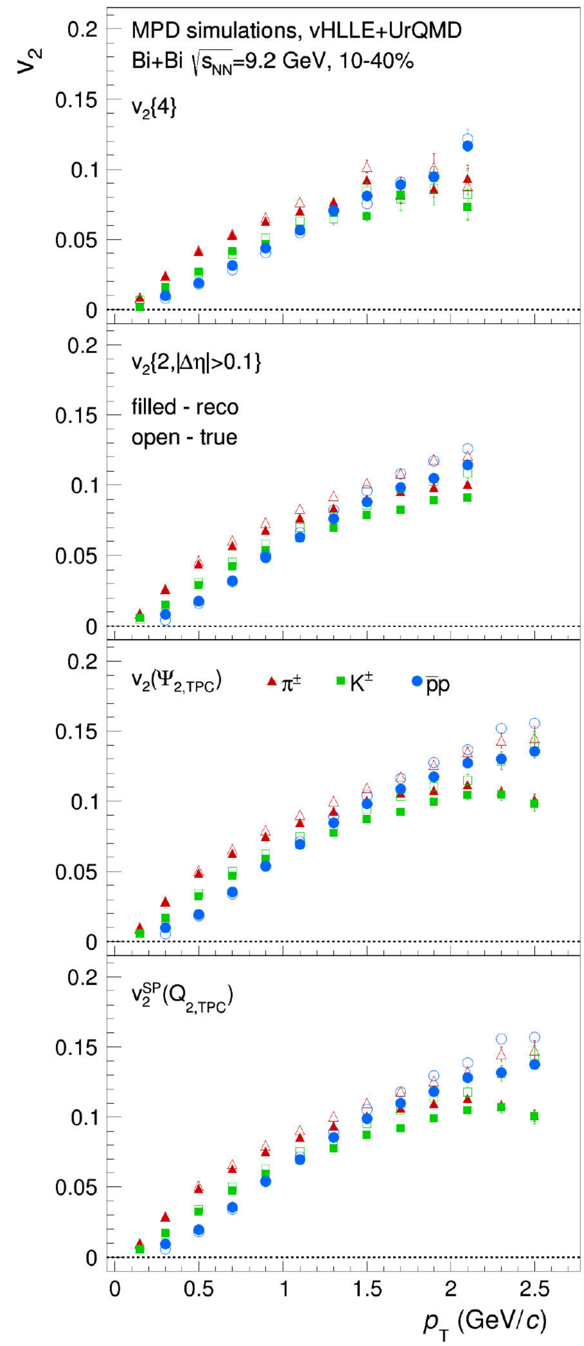

FIGURE 29. Elliptic flow $v_2(p_T)$ of identified charged hadrons as a function of p_T in 10-40% central Bi+Bi collisions at $\sqrt{s_{NN}} =$ 9.2 GeV for different methods of flow analysis of fully reconstructed events (filled markers) and generated vHLLE+UrQMD model events (open markers).

$v_2\{2\} = \langle v_2 \rangle + 0.5\sigma_{v_2}^2 / \langle v_2 \rangle$, $v_2\{4\} = \langle v_2 \rangle - 0.5\sigma_{v_2}^2 / \langle v_2 \rangle$. Our previous work demonstrates that the participant eccentricity fluctuations, in the initial geometry of the overlap region of two colliding nuclei, come mainly from v_2 flow fluctuations for colliding heavy-ion systems (Au+Au or Bi+Bi) at $\sqrt{s_{NN}} > 7$ GeV [31,89]. Consequently, the values of $v_2\{\Psi_{1,\mathrm{FHCAL}}\}$ measured with respect to the first-order event plane $\Psi_{1,\mathrm{FHCAL}}$ will consistently be smaller than the values

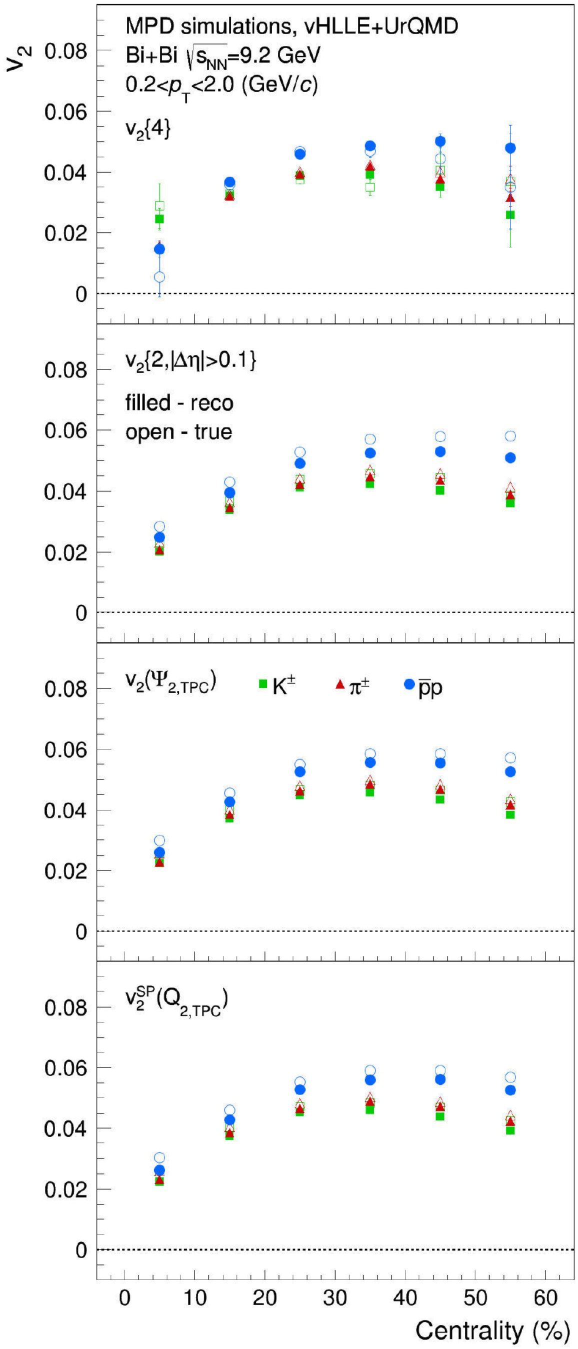

FIGURE 30. Elliptic flow v_2 of identified charged hadrons as a function of centrality in Bi+Bicollisions at $\sqrt{s_{NN}} = 9.2$ GeV for different methods of flow analysis of fully reconstructed events (filled markers) and generated vHLLE+UrQMD model events (open markers).

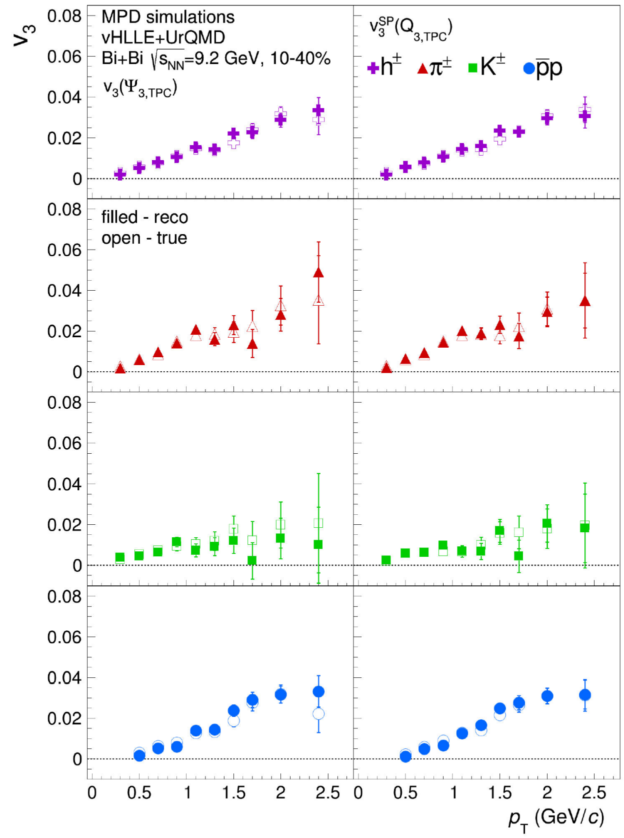

FIGURE 31. Triangular flow $v_3(p_T)$ of identified hadrons as function of transverse momentum in 10-40% central Bi+Bi collisions at $\sqrt{s_{NN}} = 9.2$ GeV for different methods of flow analysis of fully reconstructed events (filled markers) and generated events with the vHLLE+UrQMD model (open markers).

of $v_2\{\Psi_{2,\mathrm{TPC}}\}$ measured in relation to the participant plane $\Psi_{2,\mathrm{TPC}}$: $v_2\{\Psi_{1,\mathrm{FHCAL}}\} \simeq \langle v_2\rangle, v_2\{\Psi_{2,\mathrm{TPC}}\} \simeq \langle v_2\rangle + 0.5\sigma_{v_2^2}/\langle v_2\rangle$.

Figure 29 shows the performance for the measurements of v_2 as a function of p_T of identified charged pions (triangles), kaons (boxes), and protons (circles) from 10-40% central Bi+Bi collisions for reconstructed and generated vHLLE+UrQMD model events. Good agreement is observed between the v_2 results.

Due to the lack of spectators in the vHLLE+UrQMD model, we can not test the event plane method using the first-order event plane from spectators $v_2^{EP}(\Psi_{1,\mathrm{FHCAL}})$. Figure 30 shows the performance for the measurements of the centrality dependence of the elliptic flow v_2 of identified hadrons for different flow analysis methods. The conclusions from the comparison of the results of v_2 are very similar. The present statistics of 50 M minimum bias events are not sufficient for a statistically significant four-particle cumulant $v_2\{4\}$ results for 0-10% central Bi+Bi collisions. The triangular (v_3) flow of hadrons is predicted to be more sensitive (than v_2) to viscous damping and may be a good observable for investigating the formation of a QGP and pressure gradients in the early phase [21,90].

The calculations of the hybrid model show that the hydrodynamically generated v_3 signal disappears at low collision energies of $\sqrt{s_{NN}} = 5-7$ GeV and there is no v_3 signal generated in the hadronic phase [21,90]. Figure 31 shows the performance for the measurements of p_T of v_3 of identified charged hadrons in Bi+Bi collisions at $\sqrt{s_{NN}} = 9.2$ GeV for different methods of flow analysis of fully reconstructed

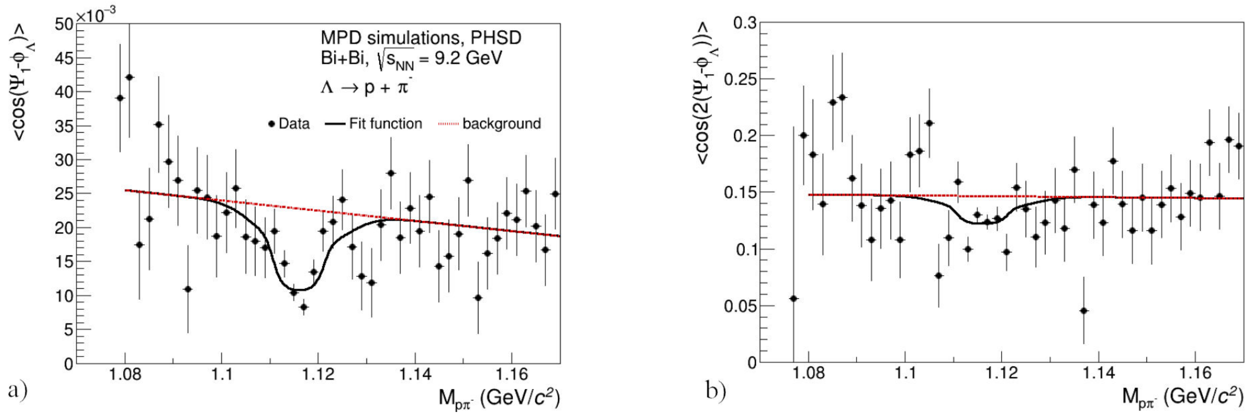

FIGURE 32. a) The demonstration of the invariant-mass fit method to extract the v_1 and b) v_2 signal for Λ particles produced in 20-50% central Bi+Bi collisions at $\sqrt{s_{NN}} = 9.2$ GeV. Reconstructed data are plotted by black symbols, fit results are shown by the colored lines.

events (filled markers) and generated vHLLE+UrQMD events (open markers). The present statistics allows us to check the event plane method using the event plane from the TPC $v_3^{\rm EP}(\Psi_{3,\rm TPC})$. In general, a good agreement is observed between the v_3 results from the analysis of fully reconstructed and generated model data.

For V^0 particles, such as K_s^0 and Λ, the invariant mass fit method [30] can be applied to separate the $v_{\rm n}^{\rm S}$ value of the signal from the $v_{\rm n}^{\rm B}$ of combinatorial background. As an example, Fig. 32 demonstrates the invariant mass fit method to extract the directed $v_1^{\rm S}$ (left panel) and elliptic $v_2^{\rm S}$ (right panel) flow signals for Λ particles produced in 20-50% central Bi+Bi collisions at $\sqrt{s_{NN}} = 9.2$ GeV. The method involves calculating the $v_n^{\rm all} = \langle \cos n(\Psi_1 - \phi_\Lambda)\rangle(M_{\rm p\pi})$ of the same-event distribution as a function of the invariant mass $M_{\rm p\pi}$ (denoted by black symbols in Fig. 32) and then fitting the resulting $v_n^{\rm all}(M_{\rm p\pi})$ distribution using

$$v_n^{\rm all}(M_{\rm p\pi}) = f^{\rm B}(M_{\rm p\pi})v_n^{\rm B}(M_{\rm p\pi}) + f^{\rm S}(M_{\rm p\pi})v_n^S, \qquad (9)$$

where $f^{\rm B}(M_{\rm p\pi})$ and $f^{\rm S}(M_{\rm p\pi})$ are the background and the signal fractions, respectively. The background $v_n^{\rm B}(M_{\rm p\pi})$ is parametrized as a linear function of $M_{\rm p\pi}$ and $v_n^{\rm S}$ is taken as a fit parameter, see Fig. 32. Figure 39 presents the resulting values for directed v_1 (left) and elliptic v_2 (right) flow of Λ hyperons as a function of pseudorapidity η and transverse momentum $p_{\rm T}$ in 20-50% central Bi+Bi collisions at $\sqrt{s_{NN}} = 9.2$ GeV for the event plane method of analysis of fully reconstructed events (filled markers) and generated PHSD model events (open markers).

Current studies show that the MPD is capable of providing detailed differential measurements of directed (v_1), elliptic (v_2), and triangular (v_3) flows of identified hadrons produced in Bi+Bi collisions at $\sqrt{s_{NN}} = 9.2$ GeV with high accuracy.

5.4. Femtoscopy and correlations

Femtoscopy serves as a tool for measuring the spatio-temporal dimensions of the systems created in particle or nuclear collisions.

These measurements are made possible by the effects of quantum statistics and final-state interactions, which induce momentum correlations between two or more particles at small relative momenta in their center-of-mass system. By studying the shape of the fireball formed during heavy-ion collisions, valuable insights into the nature of the transition between the hadron phase and the quark-gluon plasma can be gained [91-93]. Given that pions are among the most copiously produced particles in high-energy reactions, femtoscopic studies concentrate mainly, although not exclusively, on correlation studies of these particles. In this section, we present feasibility studies for two-pion correlation functions performed using UrQMD simulations.

5.4.1. Femtoscopic correlations of charged pions

From a theoretical perspective, the correlation function (CF) is defined as the ratio of the two-particle production cross-section to the product of the single-particle cross-sections. Experimentally the CF can be measured as the ratio $C(q) = A(q)/B(q)$, where $A(q)$ is the distribution of pairs from the same event and $B(q)$ represents the reference distribution of pairs from mixed events [94,95]. The quantity $q_{\rm inv}$ denotes the Lorentz-invariant momentum difference, defined as $q_{\rm inv} = \sqrt{q_0^2 - \mathbf{q}^2}$.

One-dimensional (1D) analyses of pion femtoscopy are challenging because of the non-Gaussian nature of the source, caused by long-lived resonance contributions. Therefore, an exponential Bowler-Sinyukov function (neglecting the Coulomb interaction) is commonly employed to fit the pion CF [96]

$$C(q) = 1 + \lambda \exp(-Rq), \qquad (10)$$

where λ indicates the correlation strength and R the one-dimensional source radius. More general Lévy shapes have also been recently explored [97-100].

In three-dimensional (3D) analyses performed in the Longitudinally Co-Moving System (LCMS) [91,92], information about the size and shape of the particle-emitting source can be extracted using the 3D Bowler-Sinyukov formula that, for a Gaussian-like source and ignoring the Coulomb correction, takes the form [101,102]

$$C(q_{\rm out}, q_{\rm side}, q_{\rm long}) = 1+\lambda e^{(-q^2_{\rm out}R^2_{\rm out}-q^2_{\rm side}R^2_{\rm side}-q^2_{\rm long}R^2_{\rm long})}. \quad (11)$$

In the LCMS, the vector q is decomposed into three components: $q_{\rm out}$ (in the direction of the average transverse pair momentum), $q_{\rm long}$ (in the direction of the beam) and $q_{\rm side}$ (perpendicular to both directions). This parameterization allows us to measure all three independent combinations of four space-time dimensions of the source.

Here we analyze MC data obtained from centralized production 1 in Table I, using the UrQMD model. We discuss the effects that influence the femtoscopic correlations from the experimental point of view. The most significant factors in this context are the two-track effects and the resolution of momentum.

In femtoscopic studies of two identical charged particles, track pairs with similar momenta and emission angles from the reaction region are subject to specific reconstruction effects. Track merging occurs when two spatially close tracks are incorrectly reconstructed as one, leading to inefficiency in the reconstruction of close pairs. In contrast, track splitting occurs when a single track is erroneously reconstructed as two tracks that are very close to each other. This results in a false enhancement of close pairs in the correlation function, particularly in the region of femtoscopic effects at small momentum differences. Consequently, the extracted radii and the λ parameters can be affected.

Since two-track effects occur at small angular distances, restrictions on the azimuthal angle $\Delta\phi^*$ and the polar angle $\Delta\eta$ between tracks are generally applied [103]. The angle ϕ^* is defined as the azimuthal angle ϕ of a particle with transverse momentum $p_{\rm T}$ and charge ze at some radius $\mathcal{R}$ within the TPC in a magnetic field $\mathcal{B}$,

$$\phi* = \phi + \arcsin(zeB_Z\mathcal{R}/2p_{\rm T}). \quad (12)$$

The $\Delta\eta$ $\Delta\phi^*$ distribution of pion pairs, normalized to a mixed event sample, is shown in the left panel of Fig. 40. The $\Delta\phi^*$ projection is shown in the middle panel and the $\Delta\eta$ projection is shown in the right panel. A region of inefficiency due to two-track effects is clearly visible at low $\Delta\phi^*$ and $\Delta\eta$. The width of this inefficiency region depends on the detector geometry and the two-track reconstruction efficiency [104].

Finite track momentum resolution causes the reconstructed relative momentum of a pair to differ from the true value. This can be taken into account in the theoretical function using the response matrix [105]. An example of such a matrix, that correlates the UrQMD generated relative momentum $q_{\rm model}$ with the reconstructed relative momentum $q_{\rm rec}$, is shown in the upper panel of Fig. 33. The width of the smearing effect (σ_q) is estimated to be about 4.5 MeVc in the region of the femtoscopic effect, this is shown in lower panel of Fig. 33.

The 1D CFs were studied in three intervals of pair transverse momentum $k_{\rm T}$ ($k_{\rm T} = |\mathbf{p}_{\rm T,1}+\mathbf{p}_{\rm T,2}|/2$): 0.15-0.25, 0.25-0.35, and 0.35-0.45 GeVc, as well as three centrality classes: 0-10%, 10-30%, and 30-50%.

The fits were performed using Eq. (10). Figure 34 shows the pion CFs as a function of the invariant pair relative momentum $q_{\rm inv}$. The solid blue line represents the CF with particle momenta from the UrQMD model. The open circles correspond to the CF with reconstructed pion track momenta for tracks with a number of hits greater than or equal to 40.

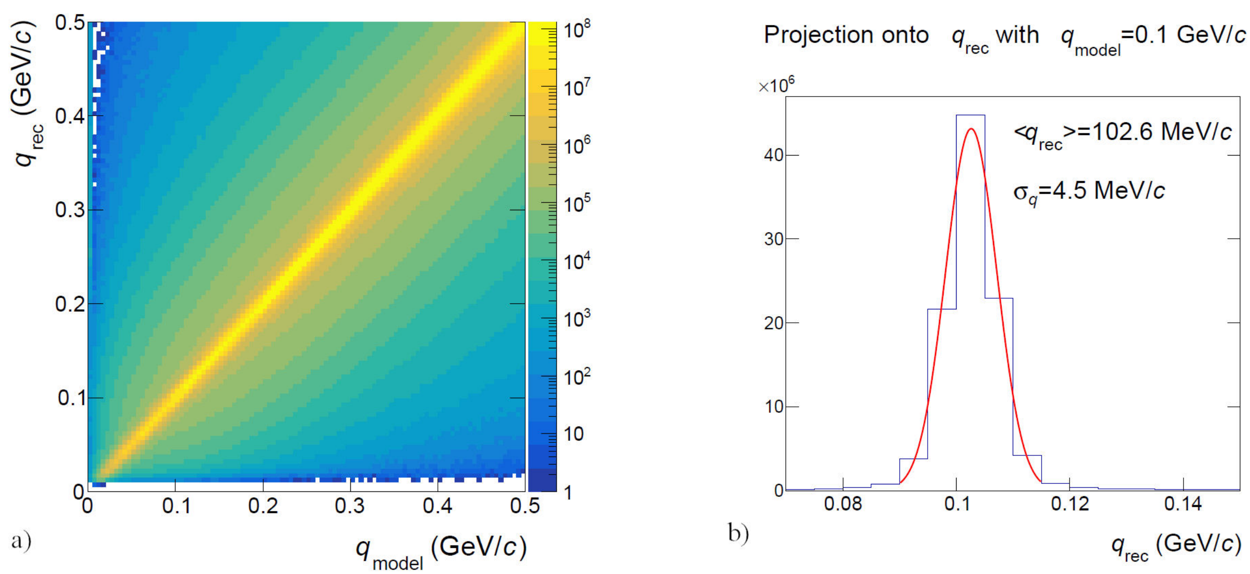

FIGURE 33. Effect of finite momentum resolution for the two particle relative momentum q. The upper panel shows, with different colors, the number of correlated pair relative momenta, quantified in the vertical scale on the right side of the plot. The lower panel shows the projection on the $q_{\rm rec}$ axis and corresponds to a distribution with a width of 4.5 MeVc.

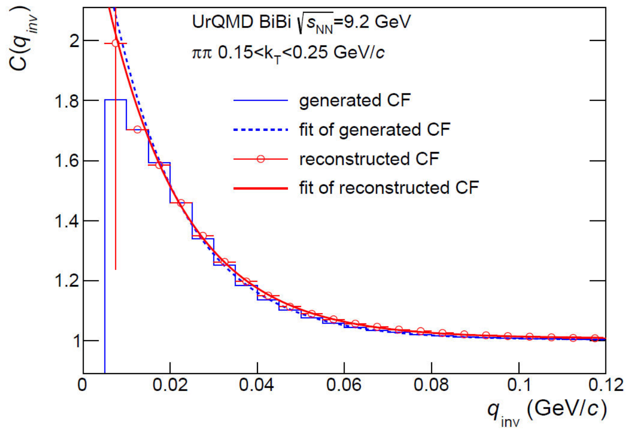

FIGURE 34. Example of simulated pion CFs fitted as function of the invariant pair relative momentum $q_{\rm inv}$. The CFs were fitted using Eq. (10).

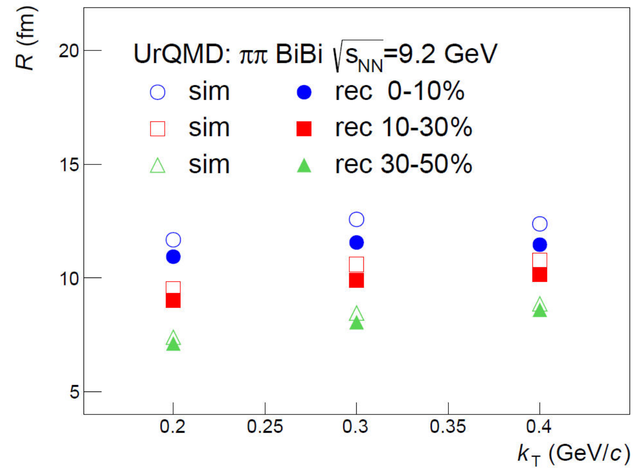

FIGURE 35. The one-dimensional radii extracted from the CFs for charged identical pions versus $k_{\rm T}$. Empty and full symbols show results for the simulated and reconstructed CFs.

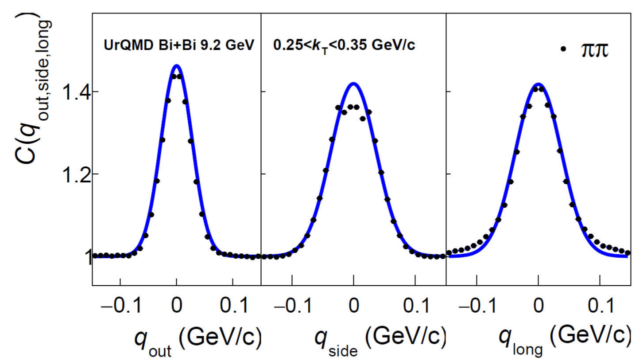

FIGURE 36. Three-dimensional two-pion correlation function projections onto the out (left), side (middle), and long (right) directions with $0.25 < k_{\rm T} < 0.35$ GeVc for 0–10 % central Bi+Bi collisions at $\sqrt{s_{NN}} = 9.2$ GeV. Solid lines represent projections of the three-dimensional fit with Eq. (11) on the corresponding axis.

Both CFs were obtained with cuts to exclude two-track inefficiency effects: $|\Delta\eta| < 0.07$ and $|\Delta\phi^*| < 0.07$, as determined from Fig. 40. Notice that there is some disagreement between the generated and reconstructed CFs in Fig. 34 in the region $q_{\rm inv} < 0.01$ GeVc, attributed to the two-track cut effects. The curves in the figure are for fits to the CFs using Eq. (10). The radius of the reconstructed correlation function is approximately 6% smaller than that of the initial ideal CF due to the distortion caused by the resolution of the momentum. While it is possible to correct for momentum smearing using deconvolution methods for real data, the corrections are delicate, especially in the low-q region since they often amplify statistical noise, and require excellent modeling of detector response and careful control of non-Gaussian tails in the resolution. This is why in actual data analysis these corrections are usually not applied directly to the correlation function. Instead, the effect is quantified using simulations and included in the systematic uncertainties. This is the procedure that we will follow when the analysis is performed with real data.

Figure 35 shows the extracted radii, R, as a function of $k_{\rm T}$ for the centrality intervals 0-10%, 10-30%, and 30-50%. The fit used to obtain the values of R was performed for both the reconstructed correlation function (solid symbols) and the true correlation function from the UrQMD model (open symbols). The exponential radius is almost flat as a function of $k_{\rm T}$. The variation of the radius with centrality is consistent with the geometric interpretation of the collisions. The maximum deviation between the reconstructed radii and the model radii is observed to be approximately 8%, while the minimum deviation is around 3%. The reduction in the reconstructed radii, compared to the model ones, is primarily attributed to the effects of momentum resolution.

The 3D $\pi\pi$ correlations were fitted for two $k_{\rm T}$ intervals: 0.15-0.25 and 0.25-0.35 GeVc, as well as for three classes of centrality: 0-10%, 10-30%, and 30-50%. The fits were performed using Eq. (11). Figure 36 shows the 3D CF projections for the first $k_{\rm T}$ interval in the out (left), side (middle), and long (right) directions. These correlation functions were obtained for 0-10% central Bi+Bi collisions at $\sqrt{s_{NN}} = 9.2$ GeV, as simulated in the UrQMD model. The projections of the fitted function, according to Eq. (11), are also shown in the figure. Deviations of the CF from the fit function at small relative momenta are associated with the application of two-track cuts.

Figure 37 shows the extracted out-side-long radii of pions for two different $k_{\rm T}$ intervals: (0.15-0.25) and (0.25-0.35) GeVc, along with three centrality classes: 0-10%, 10-30%, and 30-50%. The fit was performed for both the reconstructed correlation function (solid symbols) and the true UrQMD model correlation function (empty symbols). The reconstructed radii are smaller than the model ones, primarily due to finite momentum resolution. It is evident from Fig. 37 that the radii in all directions decrease with increasing transverse momentum of the pair. This behavior can be attributed to the presence of radial flow [106,107].

The centrality dependence of the out-side-long radii is related to a simple geometric picture of ion collisions. The pa-

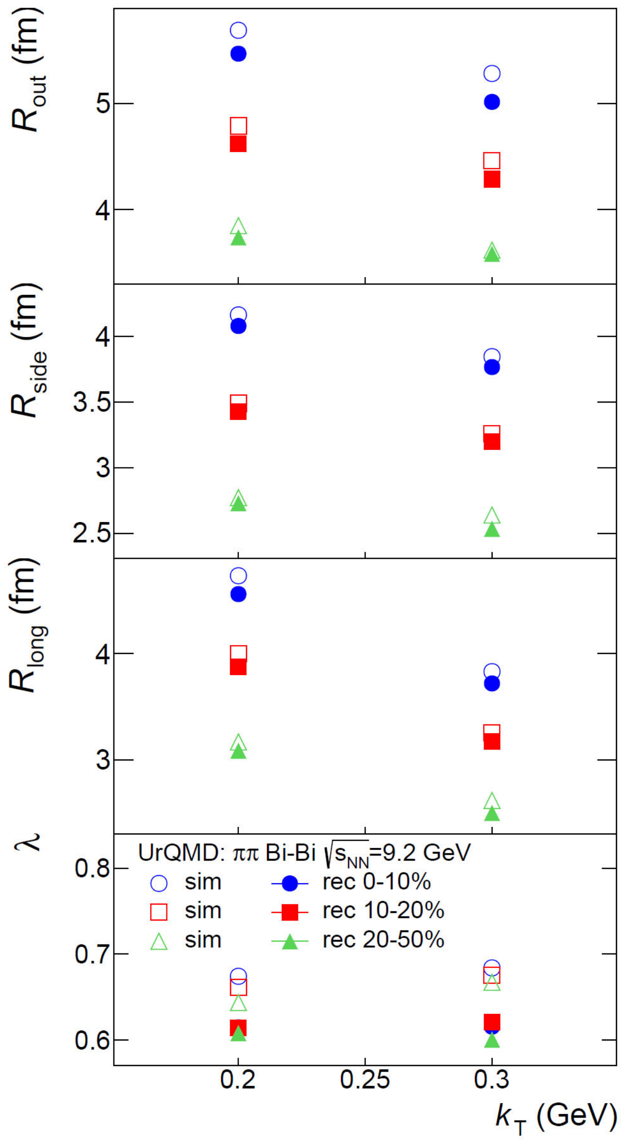

FIGURE 37. The terms $R_{\rm out}$, $R_{\rm side}$, and $R_{\rm long}$ and λ versus $k_{\rm T}$ for 0–10 %, 10–30 %, 30–50 % central Bi+Bi collisions at $\sqrt{s_{NN}}$ = 9.2 GeV. Empty and full symbols show results for the simulated and reconstructed CFs.

rameter λ equals unity in the ideal case of a Gaussian spherical source consisting only of primary particles emitted randomly from the source. The correlation strength λ is less than 0.7 for the model, which could be due to the influence of long-lived resonances and a non-ideal Gaussian source distribution. The value of the parameter λ for the reconstructed CF is lower than that of the model CF, mainly due to finite momentum resolution and the distortion of the CF resulting from two-track cuts.

5.4.2. *Charged balance function*

The charge balance function (CBF) has been proposed as a convenient measure of the correlation between oppositely charged particles [108]. It provides valuable insight into the charged particle production mechanism and can address the fundamental question concerning the hadronization process in nuclear collisions at relativistic energies [109]. The final degree of correlations is reflected in the balance function and consequently in its width. It is defined as

$$B(\Delta y) = \frac{1}{2}\left\{ \frac{\langle N^{+-}(\Delta y)\rangle - \langle N^{++}(\Delta y)\rangle}{\langle N^{+}\rangle} + \frac{\langle N^{-+}(\Delta y)\rangle - \langle N^{--}(\Delta y)\rangle}{\langle N^{-}\rangle} \right\}, \qquad (13)$$

where $\langle N^{+-}(\Delta y)\rangle$ is the average number of opposite-charge pairs with particles separated by a relative rapidity Δy, and similarly for $\langle N^{-+}(\Delta y)\rangle$, $\langle N^{++}(\Delta y)\rangle$, and $\langle N^{--}(\Delta y)\rangle$. $\langle N^{+}\rangle$ and $\langle N^{-}\rangle$ are the numbers of positively and negatively charged particles in the rapidity interval, over all events. The charge balance function $B(\Delta\varphi)$, as a function of the relative azimuthal angle $\Delta\varphi$, is defined similarly [108]. $\langle N^{+-}\rangle$ and $\langle N^{-+}\rangle$ are equal for inclusive CBFs, however, they may differ for partial CBFs. The analysis of partial CBFs is currently outside the scope of the present study. The width of the balance function distribution is defined as

$$\langle \Delta y\rangle = \frac{\sum_{\rm i} B_{\rm i}\Delta y_{\rm i}}{\sum_{\rm i} B_{\rm i}}, \qquad (14)$$

where $B_{\rm i} = B(\Delta y_{\rm i})$ is the balance function value for each bin, with the sum running over all bins. The CBF width is sensitive to the duration of electric charge separation, and thus provides information on the hadronization time and may be used to extract information about the space-time characteristics of the particle emitting source. In a hydrodynamic approach, the width is proportional to the inverse strength of the collective radial flow in the system, allowing to estimate collective effects as well.

CBFs for heavy-ion collisions were experimentally studied at SPS [110], RHIC [111,112], and LHC [113-115]. Two interesting experimental observations were made: the balance function width increases with the increase of the centrality, and the width decreases while the energy of the beam increases.

The CBF modeling for MPD conditions was performed using UrQMD-based production number 1 from Table I. The tracks were selected according to cuts similar to those used in the analysis of the STAR experiment [112]: $0.2 < p_{\rm T} <$ 2 GeVc and $|\eta| < 1$. The tracks were required to have at least 15 hits in the TPC and be matched to the primary vertex with DCA$<$ 3 cm. The primary vertex was restricted to be positioned within 30 cm along the beam axis and within 2 cm in the transverse direction. Both, rapidity and azimuthal CBFs for inclusive and identified charged hadrons, were analyzed at $\sqrt{s_{NN}} = 9.2$ eV in Bi+Bi collisions in the 0-80% centrality class. Figure 38 shows the width of the pseudo-rapidity and azimuthal charge balance function for inclusive charged

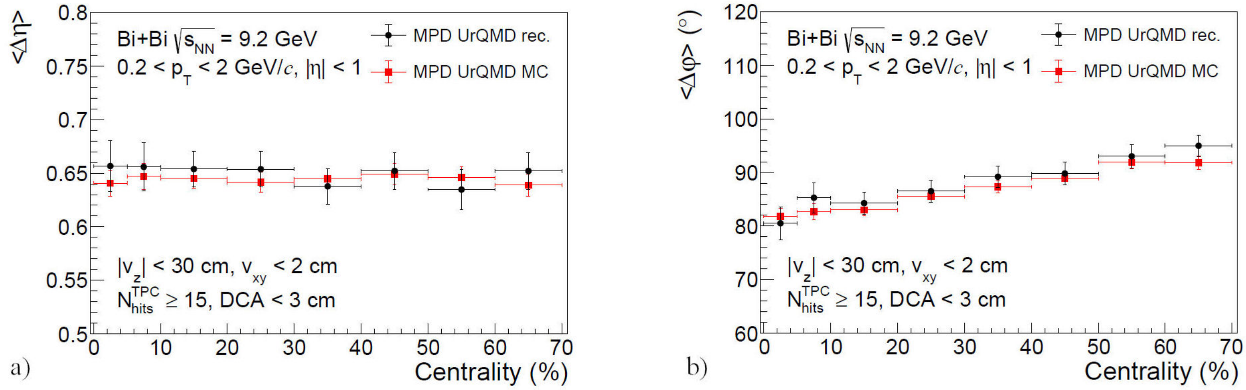

FIGURE 38. The pseudo-rapidity (left) and azimuthal (right) charge balance function width for inclusive charged hadrons. Black circles represent the widths obtained from reconstructed events whereas red squares represent the widths obtained at generator level (UrQMD data).

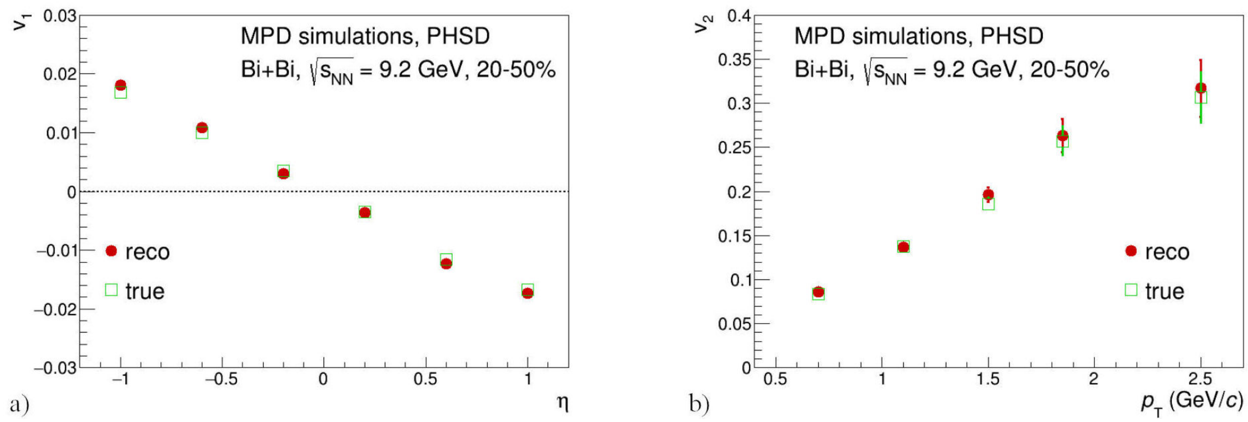

FIGURE 39. a) Directed v_1 and b) elliptic v_2 flow of Λ hyperons as a function of pseudorapidity η and transverse momentum p_{T} in 20-50% central Bi+Bi collisions at $\sqrt{s_{NN}} = 9.2$ GeV for the event plane method of the analysis of fully reconstructed events (filled markers) and generated PHSD model events (open markers).

hadrons, where black circles represent the widths obtained from reconstructed events, and red squares the generator-level UrQMD data. Notice that the CBFs shown in Fig. 38 are not significantly affected neither by the finite momentum resolution nor by particle identification effects. This observable is considered robustly resistant to common detector inefficiencies due to the fact that only the correct determination of the electric charge is essential, which is done with very good accuracy.

The CBFs were corrected to account for the charge imbalance that is present (owing to the finite values of baryon, strangeness, and isospin chemical potentials) at NICA energies, using the event mixing technique [112]. This technique requires to calculate an additional set of CBFs composed of tracks that are selected from different events. These mixed CBFs can be subtracted from the same-event CBFs, to remove distortions due to charge imbalance. To estimate the reconstruction efficiency, the reconstructed widths were compared to those obtained at the generator level.

In summary, femtoscopic and correlation studies are useful tools to reveal the spacetime properties of the particle-emitting source in relativistic heavy-ion collisions. We have shown that the MPD momentum resolution allows carrying out this kind of study, providing an agreement within statistical uncertainties between the reconstructed and model parameters.

5.5. Electromagnetic signals and neutral mesons

Electromagnetic signals – photons and electrons – provide the possibility to measure spectra and correlations of neutral mesons, direct photons and dilepton pairs. Neutral mesons can be reliably identified in a wide momentum range and complement measurements of charged identified hadrons. Direct photons are the photons not originated from decays of final state hadrons, but produced in electromagnetic interactions in the course of the collision. Direct photons escape the hot fireball and deliver information about temperature, development of the collective flow and space-time dimensions of the system at all stages of the collision, including the hottest one. Dileptons similar to (real) direct photons allow us to probe the hot matter, but in addition, reflect in-medium modifications of vector meson properties. This makes them sensitive to both the deconfinement and chiral symmetry restora-

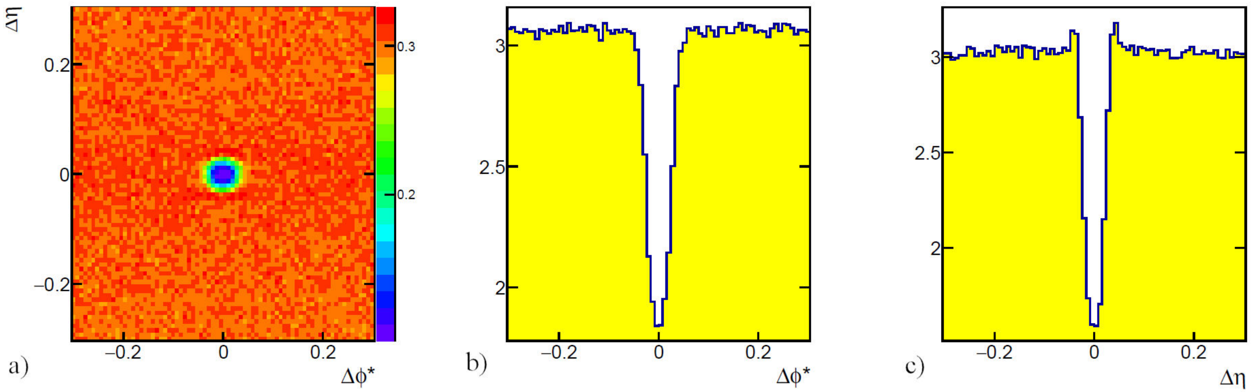

FIGURE 40. a) Two-dimensional $\Delta\eta$ $\Delta\phi^*$ distributions for reconstructed tracks. b) Projections in $\Delta\phi^*$ and c) $\Delta\eta$.

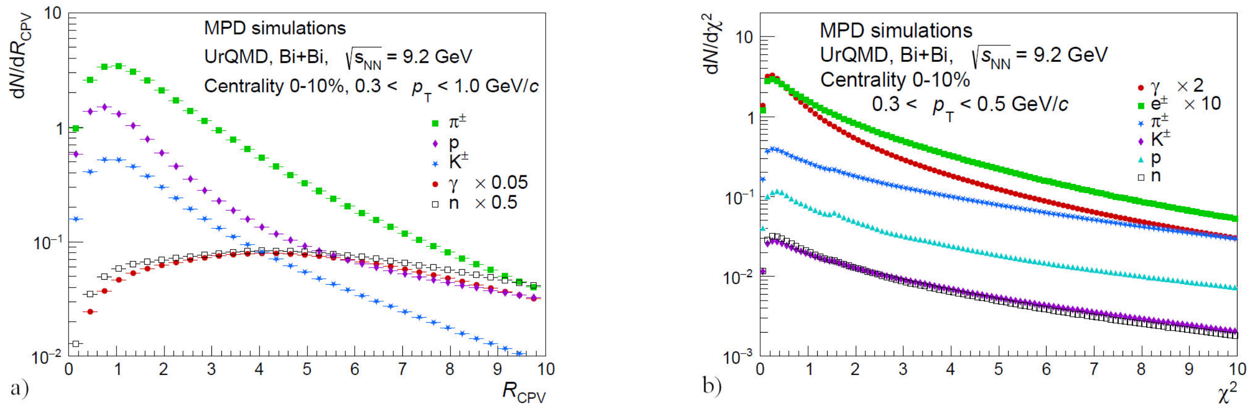

FIGURE 41. a) Distance to closest track in units of standard deviations for clusters produced by different particles. b) Shower shape fit parameter distribution for different kinds of clusters.

tion phase transitions. In this section, we review the MPD capabilities for the measurements of photons, neutral mesons and dielectrons in Bi+Bi collisions at $\sqrt{s_{NN}} = 9.2$ GeV.

5.5.1. *Photons*

Direct photons can be emitted either in hard processes involving partons of incoming nucleons (*prompt* direct photons) or as the thermal emission of hot quark or hadron matter (*thermal* direct photons). Prompt photon production at NICA energies probes nucleon structure functions in a high x_{Bj} region where they are relatively poorly constrained [116]. Predictions for the thermal direct photon yields in heavy-ion collisions at NICA energies are very scarce. One of them is based on hydrodynamic calculations combined with the UrQMD model [116]. Another one is based on the phenomenological extrapolation of available experimental results [117]. The two approaches provide similar predictions. The expected contribution of direct photons to the inclusive spectrum is on the level of 5-10% at $p_{\mathrm{T}} \sim 1$ GeVc which makes their reconstruction challenging but yet a realistic experimental task.

Photons in the MPD can be reconstructed in two ways, either in the electromagnetic calorimeter (ECAL) or converted in the material of the beam pipe or inner walls of the TPC and reconstructed as a pair of e^+e^- tracks in the tracking system.

To reconstruct photons in ECAL, a clusterization procedure is used. It selects a seed cell with the energy above the threshold $E_{\mathrm{seed}} = 30$ MeV and adds all cells with common side and energy exceeding a minimal energy threshold of 5 MeV. If the cluster has more than one local maximum, an unfolding procedure is applied based on the fitting energy depositions in all cells with electromagnetic shower shapes with local positions and energies considered as free parameters. The energy of a cluster is calculated as a sum of the energies of the cells. The coordinates of a cluster both in z and ϕ directions are assigned to the "centers of gravity" calculated with logarithmic weights, similar to *e.g.* calorimeters in the ALICE experiment [118]

$$\langle x\rangle = \frac{\sum w_i x_i}{\sum w_i}, \quad w_i = \max\left(0, \log\left(\frac{E_i}{E}\right) + 5.5\right), \tag{15}$$

where the cut-off parameter 5.5 is chosen as large as possible with expected electronic noise.

Photon identification in the ECAL is performed based on three independent criteria: time-of-flight, neutrality and shower shape. The time-of-flight is based on the good time resolution of the ECAL which was estimated in beam tests [119] to reach about 250 ps at $E_{\mathrm{clu}} > 500$ MeV. The neutrality of a cluster is estimated by calculating the distance to the closest track reconstructed in the TPC and extrapolated

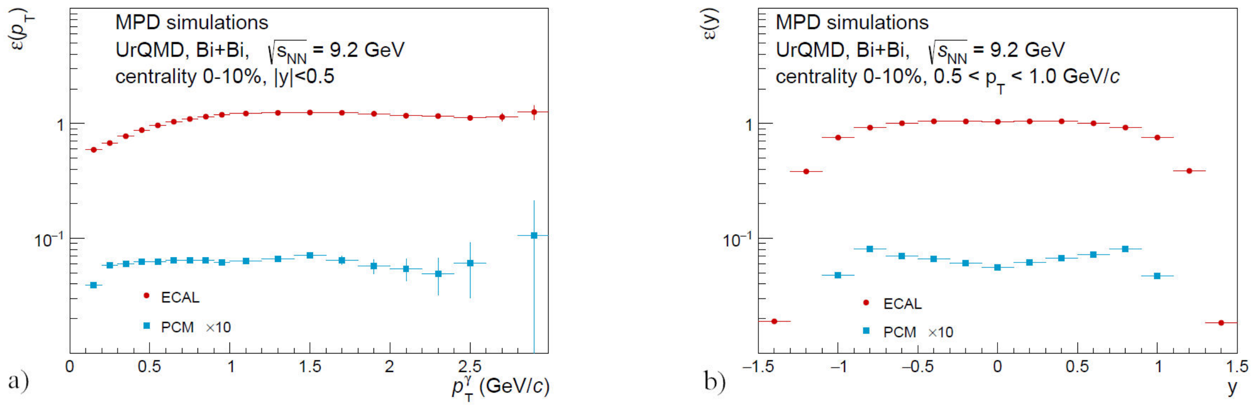

FIGURE 42. a) Inclusive photon reconstruction efficiency in the ECAL and PCM method as a function of photon p_{T}^{γ}. b) Inclusive photon reconstruction efficiency in the ECAL and PCM method as a function of rapidity.

to the ECAL surface. The width of this distribution is parametrized and the distance between cluster and extrapolated track RCPV is provided in units of σ, see Fig. 41a). Clusters, associated with charged particles, have maxima at $R_{\mathrm{CPV}} \sim 1$, while photon and neutron clusters have wider distributions from random associations between clusters and tracks.

The third photon identification criterion is based on the shape of the cluster: hadrons produce either clusters with very small dispersion in the case of minimum ionizing particles or clusters with large dispersion in the case of strong hadronic interaction. Photons and electrons, on the contrary, produce compact clusters. Quantitatively, the comparison can be done in two approaches, either by evaluating eigenvalues of the dispersion matrix

$$M_{\mathrm{ij}} = \frac{\sum_{\mathrm{k}}(x_{\mathrm{i,k}} - \langle x_{\mathrm{i}} \rangle)(x_{\mathrm{j,k}} - \langle x_{\mathrm{j}} \rangle) w_{\mathrm{k}}}{\sum_{\mathrm{k}} w_{\mathrm{k}}}, \qquad (16)$$

where $x_{\mathrm{i,k}}$ is the i-th coordinate in the ECAL surface of the cell with number k and w_{k} is the logarithmic weight, the same as in Eq. (15). An alternative approach calculates the result of the fit of the energy distribution within the clusters with the expected shape of the electromagnetic shower and returns the χ^2, which can also be used to separate photon and hadron showers, as shown in Fig. 41b). Nonelectromagnetic clusters have wider distributions, a feature that is used for photon or electron selection.

The second method of the photon reconstruction in the MPD is the Photon Conversion Method (PCM). It is based on reconstruction of e^+e^- pairs created in photon conversion in the material of the beam pipe or of the inner vessels of the TPC. Electron and positron tracks are identified in the TPC, requiring the measured specific ionization losses dE/dx to be within $3\sigma^{e}_{\mathrm{TPC}}(p_{\mathrm{T}})$ of the values expected for electrons. If the tracks match the TOF, their measured velocities are required to be consistent with the electron signals within $3\sigma^{e}_{\mathrm{TOF}}(p_{\mathrm{T}})$. Then the two dentified tracks are combined with a Kalman Filter for a V^0 particle. A set of topological selections are considered and used to select true conversion pairs: $\chi^2 < 10$, the DCA of two tracks (DCA < 2.8 cm), the Cosine of Pointing Angle (CPA) between pair momentum and direction from conversion vertex to the primary vertex (CPA > 0.98), the angle between perpendicular to the pair plane and the magnetic field ($|\psi| < 0.275$).

A comparison of the efficiency of photon reconstruction for the two methods, as a function of transverse momentum and rapidity, is shown in Fig. 42. The photon reconstruction efficiency in the ECAL is close to unity at sufficiently large p_{T} and decreases to $\sim$ 70% at $p_{\mathrm{T}} = 0.1$ GeVc. At $p_{\mathrm{T}} \sim 1$ GeVc the reconstruction efficiency even exceeds unity due to the finite energy resolution and the shape of the inclusive photon spectrum. The efficiency of the PCM method is approximately 100 times lower (take note of the scale factor for the PCM case) due to the small conversion probability up to the middle of TPC and relatively strict selection criteria. With a primary vertex selection within $|z_{\mathrm{vertex}}| < 50$ cm used in this analysis, the ECAL allows re-construct photons within rapidity $|y| < 1$ with almost constant efficiency and up to $|y| < 1.3$ with reduced efficiency. The efficiency of the PCM method shows some rapidity dependence due to the acceptance of the TPC and allows for a photon reconstruction within $|y| < 1$.

5.5.2. *Differential p_T spectra for π^0 and η mesons*

Spectra of neutral π^0, η and other mesons can be measured with high precision through their two-photon decay channels.

Neutral meson spectra help test the thermal and chemical equilibrium in the hot fireball, its collective radial expansion, and other general properties of the system. In addition, combining neutral mesons with charged tracks provides a way to reconstruct short-lived hadronic resonances and to study strangeness production. Furthermore, increased fluctuations in the relative yield of neutral and charged mesons may indicate the presence of a pion Bose-Einstein condensate [120], or of the Critical End Point [121].

The production of π^0 and η mesons was measured in the $\pi^0(\eta) \to \gamma + \gamma$ decay channel at mid-rapidity $|y| < 0.5$ in

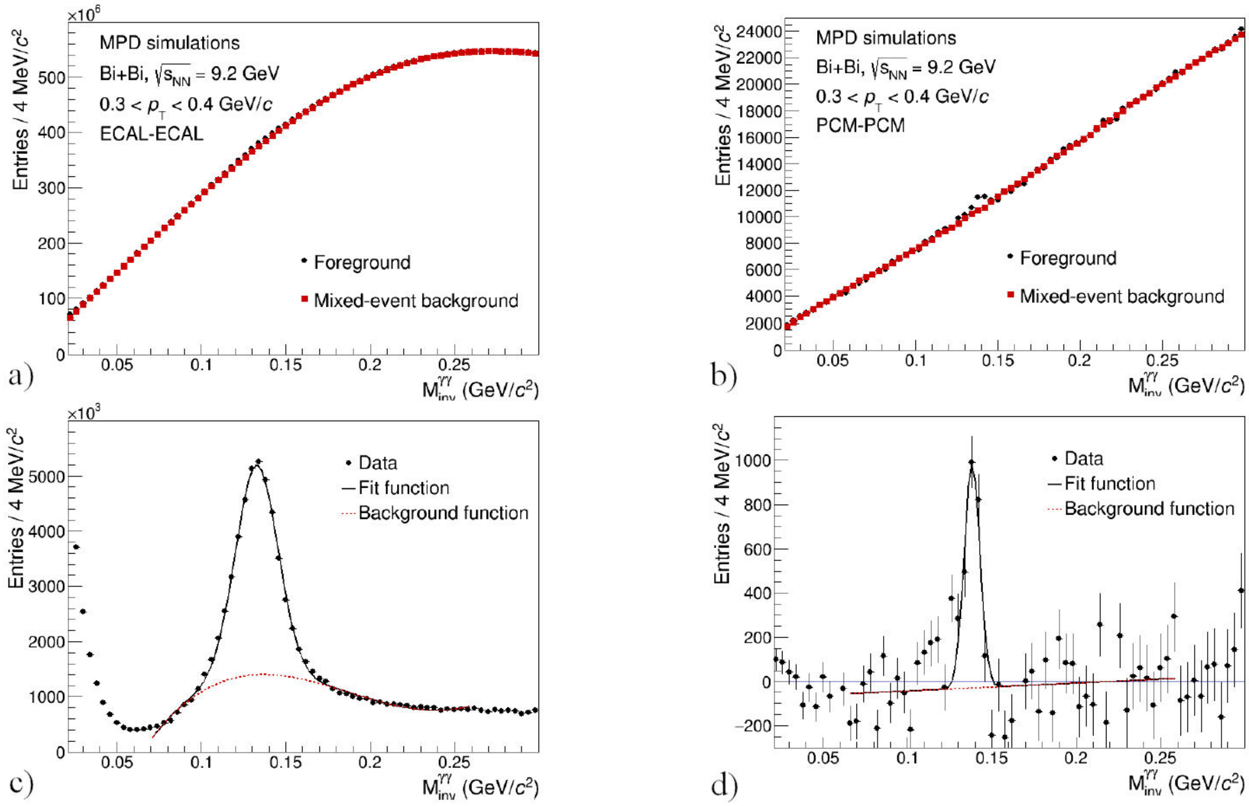

FIGURE 43. Invariant mass distributions for $\gamma\gamma$ pairs before a) b) and after c) d) subtraction of the mixed-event background. The plots on the left and right are for ECAL-ECAL and PCM-PCM combinations, respectively. Examples are shown for minimum bias Bi+Bi collisions at $\sqrt{s_{\rm NN}} = 9.2$ GeV. Solid and dashed red curves represent fits to the function described in the text.

Bi+Bi collisions at $\sqrt{s_{\rm NN}} = 9.2$ GeV using the data of mass production 1 from Table I. The main detector subsystems used in this analysis are the ECAL, the TPC and the TOF detectors. Only events with a reconstructed vertex lying within $|z_{\rm vertex}| < 100$ cm and centrality in a range 0-90% were accepted. The number of analyzed minimum bias events is equal to about 4×10^7 collisions. The available statistics are sufficient only to measure the centrality-dependent production of π^0 mesons in fine-momentum bins and to estimate the η meson production in minimum-bias collisions.

The two approaches described above were used for the reconstruction of photons: photon measurements in the ECAL or photon conversion method. The calorimeter-reconstructed clusters were selected as photon candidates if they satisfied minimum selections: $E_\gamma > 0.075$ GeV, the number of towers in the cluster is greater than one, the shower shape is consistent with the shape expected for electromagnetic signal, χ^2/NDF < 4, the time-of-flight is less than 2 ns. Photon conversion pairs were selected as described in the previous section.

The yields of π^0 and η mesons for each $p_{\rm T}$ and the centrality interval are measured by calculating the invariant mass distributions of photon pairs at midrapidity $|y| < 0.5$ in different combinations: ECAL-ECAL, ECAL-PCM, PCM-PCM. The combinatorial background is estimated using a mixed-event method, when one of the photons is taken from the current event and the second is taken from another event with similar topology (the difference in $z_{\rm vertex}$ and event centrality does not exceed 20 cm and 10%, respectively). The mixed-event invariant distributions are scaled to the same event distributions at high masses where the contribution of correlated pairs is minimum. Examples of invariant mass distributions before and after subtracting the mixed-event background are shown in Fig. 43. After subtraction, the resulting distributions contain the remaining correlated background from minijets and pairs from misreconstructed hadronic decays, which have a smooth dependence on the mass. The remaining background is parametrized with a polynomial, while contributions from decays of neutral mesons are described with a Gaussian function. Parameters of the Gaussian and polynomial functions are kept free in fits to the invariant mass distributions. The extracted mass and width values for the π^0 and η mesons are found to be consistent with the expected values within uncertainties. Examples of the fits are presented in the same figure. The meson yields are estimated either as integrals of Gaussian functions or by bin counting in the mass range $|m - M_{\rm rec}| < 3\sigma_{\rm rec}$ followed by the subtraction of the polynomial integral in the same range. The values of $M_{\rm rec}$ and $\sigma_{\rm rec}$ are the mass and width of the neutral meson extracted from the fit.

The same data sample was used to evaluate the reconstruction efficiencies for the π^0 and η mesons in the π^0 or $\eta \to \gamma + \gamma$ decay channel, as well as to estimate the expected

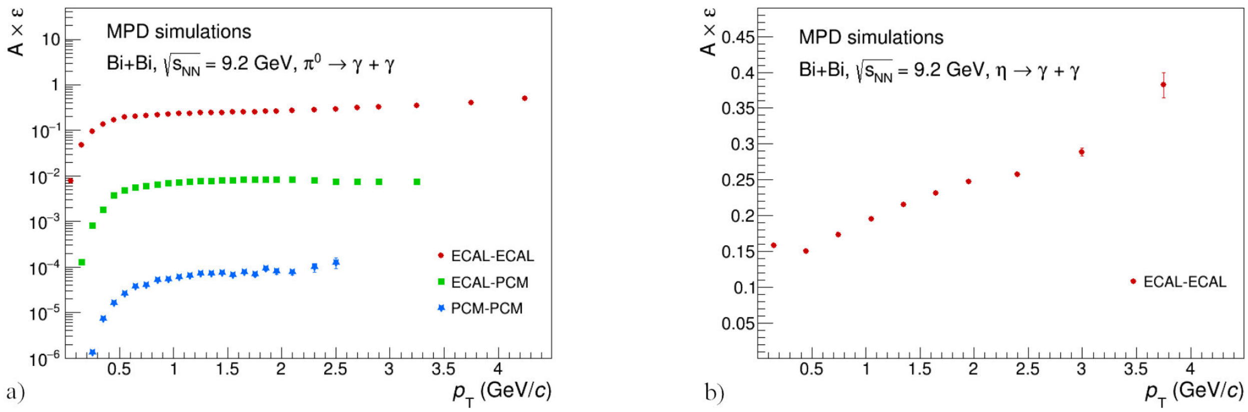

FIGURE 44. Reconstruction efficiency $A \times \varepsilon$ evaluated for π^0 and η mesons in the $\pi^0(\eta) \to \gamma + \gamma$ decay channel in Bi+Bi collisions at $\sqrt{s_{\rm NN}} = 9.2$ GeV.

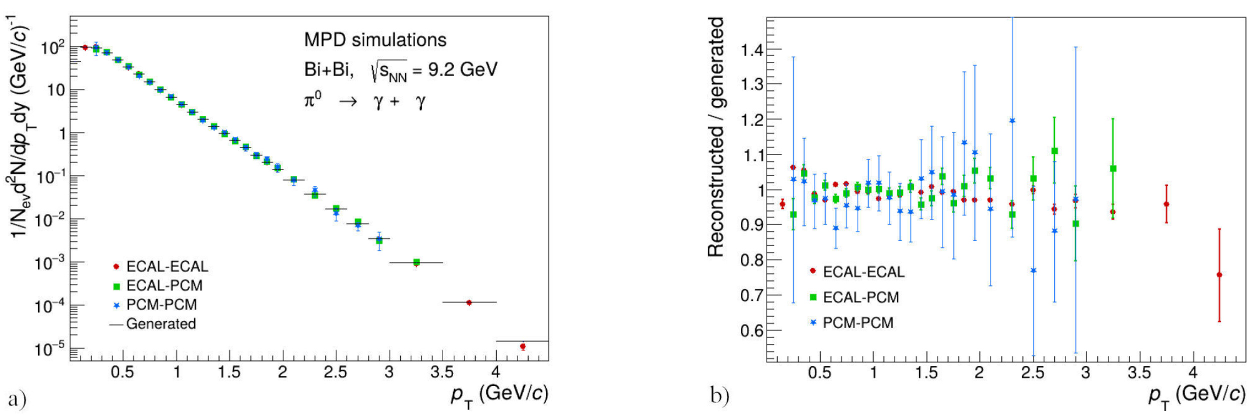

FIGURE 45. a) Differential production spectra and b) their ratio to the truly generated one for π^0 mesons in minimum bias Bi+Bi collisions at $\sqrt{s_{\rm NN}} = 9.2$ GeV. Results are shown for different photon selections: ECAL-ECAL, ECAL-PCM and PCM-PCM, see text for details.

masses and widths of the reconstructed signals. For each analyzed $p_{\rm T}$ and centrality interval, the efficiencies $A \times \varepsilon$ are calculated as the ratio $N_{\rm rec}/N_{\rm gen}$, where $N_{\rm rec}$ is the number of reconstructed particles in the $\gamma + \gamma$ channel, after all event and track selection cuts, and $N_{\rm gen}$ is the number of generated mesons within $|y| < 0.5$ decaying in the $\pi^0(\eta) \to \gamma + \gamma$ channel. Examples of efficiencies evaluated for the π^0 and η mesons for minimum bias Bi+Bi collisions as a function of transverse momentum are shown in Fig. 44. The difference at low $p_{\rm T}$ between the efficiencies for π^0 and η mesons, reconstructed using the same photon selections, is due to the different masses of the particles and hence mean energies of decay photons at the same $p_{\rm T}$ of parent mesons. Quite a large difference is observed for the reconstruction efficiencies of π^0 with different methods explained by the rather small probability of photon conversion in the detector materials with a total radiation length of $X/X_0 \sim 4.5\%$. The evaluated efficiencies show a rather modest dependence on the centrality of the event.

The fully corrected yields evaluated according to Eq. (5) for π^0 meson in minimum bias Bi+Bi collisions at $\sqrt{s_{NN}} = 9.2$ GeV with three different reconstruction methods are shown in Fig. 45. The spectra agree with each other and with the truly generated one within uncertainties. The momentum coverage for the measured spectra is comparable. Figures 43 and 44 clearly demonstrate the difference between the methods. The ECAL-ECAL method has the highest efficiency, but measurements at low momenta are characterized by a rather poor energy resolution and a significant hadronic and combinatorial background. In contrast, the PCM-PCM approach takes advantage of the much better energy resolution of the tracking system and the superior purity of photon reconstruction at low momenta, resulting in much narrower reconstructed peaks and lower background. However, the method suffers from low efficiency as a result of a small photon conversion probability. The hybrid ECAL-PCM method occupies an intermediate position, sharing the advantages and disadvantages of the above two methods. Measurements with the ECAL-ECAL and ECAL-PCM methods allow us to study the dependence of π^0 production on centrality. The statistics of the PCM-PCM method do not allow for such a detailed study with the available data set. Measurements with the ECAL-ECAL have a smaller statistical uncertainty and are used hereafter by default. However, measurements with ECAL-PCM and PCM-PCM are important, especially at low momentum, to study the performance and systematic

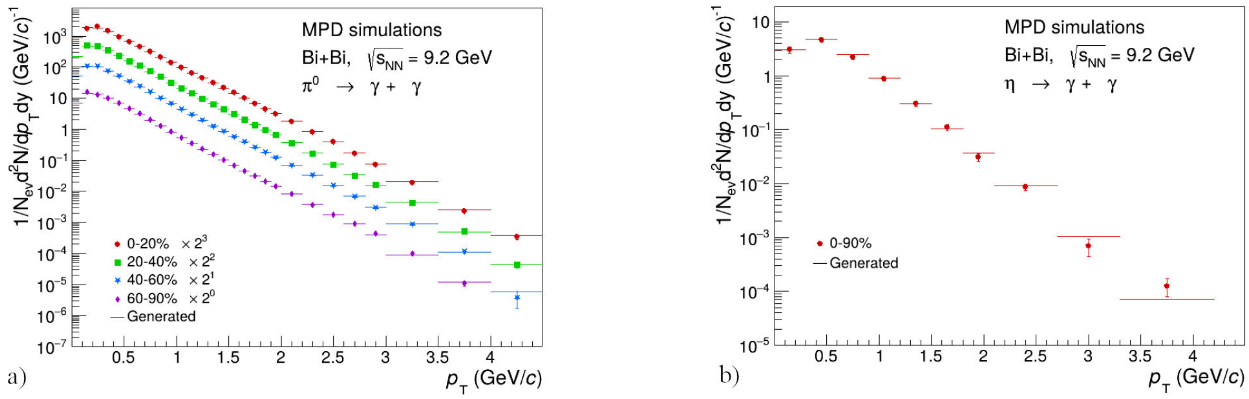

FIGURE 46. Differential production spectra for π^0 and η mesons in Bi+Bicollisions at $\sqrt{s_{\rm NN}} = 9.2$ GeV. Results for π^0 meson are shown in different centrality intervals. The measured points are compared to the true ones shown with histograms.

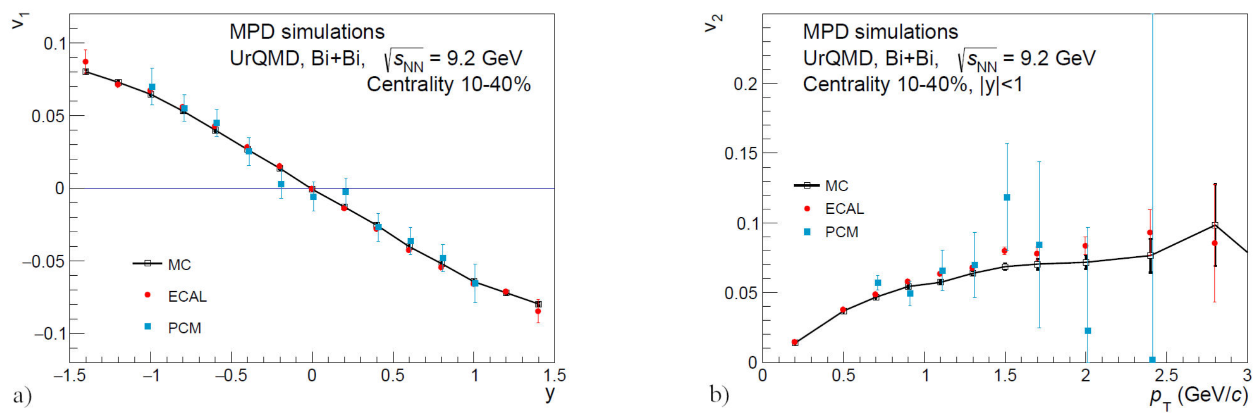

FIGURE 47. a) Inclusive photon directed collective flow vs. rapidity. b) Inclusive photon elliptic collective flow vs. $p_{\rm T}$.

effects in the calorimeter. The available statistics are sufficient to measure only the production of centrality-integrated η mesons using the ECAL-ECAL method.

The differential yields measured for the π^0 and η mesons as a function of transverse momentum in centrality-differential Bi+Bi collisions at $\sqrt{s_{\rm NN}} = 9.2$ GeV are shown in Fig. 46. The measurements span a wide $p_{\rm T}$ range from 0.1 to 4.5 GeVc with the accumulated statistics. The reconstructed spectra are compared to the truly generated ones shown with histograms. The reconstructed spectra match the ones generated within statistical uncertainties. Additional photon selections, such as cluster neutrality and/or a higher minimum energy of clusters with $E_\gamma > 0.2$ GeV were optionally used to further suppress the hadronic background and optimize the reconstructed peak shapes.

The fully corrected spectra obtained using different selections were compared and found to agree within 5-10%, with a tendency for a larger discrepancy at lower momenta. Since statistical uncertainties in such comparisons are highly correlated, the observed discrepancies serve as a rough estimate of the systematic uncertainty for the signal extraction.

5.5.3. *Collective flow of inclusive photons and neutral mesons*

The measurement of the collective flow of inclusive photons is a necessary ingredient for the extraction of the direct-photon flow. The latter is measured as a difference of the inclusive photon flow $v_2^{\gamma.{\rm incl}}$ and flow of decay photons $v_2^{\gamma.{\rm dec}}$:

$$v_{\rm n}^{\gamma.{\rm dir}} = \frac{v_{\rm n}^{\gamma.{\rm incl}} R_\gamma - v_{\rm n}^{\gamma.{\rm dec}}}{R_\gamma - 1}, \quad R_\gamma = \frac{N^{\gamma,{\rm incl}}}{N^{\gamma,{\rm dec}}}. \tag{17}$$

The decay photon flow $v_2^{\gamma.{\rm dec}}$ is estimated using Monte-Carlo simulations based on the measured π^0 flow and on the measured or estimated flow of other neutral mesons [122,123] for details. We compare the reconstructed directed and elliptic flow of inclusive photons with the truly generated signals in Fig. 47a). The inclusive photon directed flow v_1, integrated over $p_{\rm T}$, measured with the ECAL, reproduces the inclusive photon flow calculated at the generator level in the range $|y| < 1.5$. The PCM method also reproduces the generated flow, though with larger uncertainties within $|y| < 1$.

The dependence of the collective elliptic flow v_2 of inclusive photons on the transverse momentum is presented in Fig. 47b). The simulation was performed using approx-

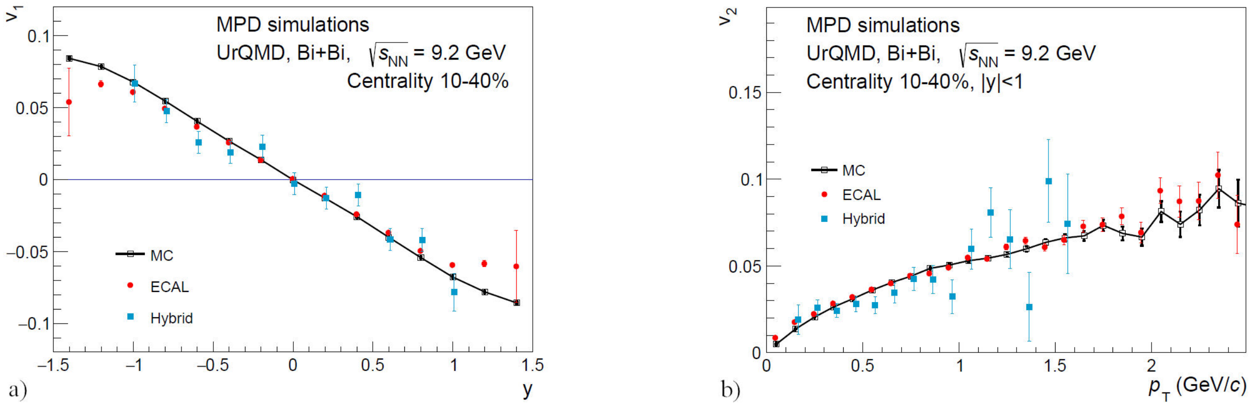

FIGURE 48. a) Neutral pion directed collective flow vs. rapidity. b) Neutral pion elliptic collective flow vs. p_{T}.

TABLE V. Selection cuts for electron track reconstruction and eID. The signals from TPC, TOF and ECAL, *i.e.* $\langle dE/dx \rangle$ in TPC, time-of-flight in TOF, and E/p and time-of-flight in ECAL, respectively, are expressed in units of standard deviations from the signals expected for true electrons. Similar expressions are used for TOF and ECAL matching variables, dϕ and dz.

Variable	Cut
$n_{\mathrm{TPC}}^{\mathrm{hits}}$	39
DCA	$< 3\sigma$
TPC dE/dx	$n_{\sigma,e} < 2\sigma$, $p_{\mathrm{T}} < 0.8$ GeVc
	$-1 < n_{\sigma,e} < 2\sigma$, $p_{\mathrm{T}} > 0.8$ GeVc
TPC-TOF match.	$n_{\sigma,e}^{\mathrm{d}\phi}$ and $n_{\sigma,e}^{\mathrm{dz}} < 2\sigma$
TOF eID	$\lvert n_{\sigma,e}^{\mathrm{ToF}} \rvert < 2\sigma$
TPC-ECAL match.	$n_{\sigma,e}^{\mathrm{d}\phi}$ and $n_{\sigma,e}^{\mathrm{dz}} < 3\sigma$
ECAL E/p eID	$n_{\sigma,e}^{\mathrm{E/p}} < 2\sigma$
ECAL m^2 eID	$\lvert n_{\sigma,e}^{\mathrm{ToF}} \rvert < 1.5\sigma$

1 million Minimum Bias events after event selection. With available statistics, one can measure the elliptic flow of inclusive photons with reasonable accuracy up to $p_{\mathrm{T}} \sim 2.5$ GeVc with the ECAL and up to $p_{\mathrm{T}} \sim 1$ GeVc with the PCM method.

In Fig. 48, we present a comparison of the neutral pion directed flow as a function of rapidity and the elliptic flow v_2 as a function of p_{T}. All three methods can potentially be used to extract the neutral pion flow. However, the PCM method lacks statistics and does not produce any reasonable result at this point. We found that both the ECAL and hybrid methods produce consistent results and reproduce the flow of primary generated neutral pions shown with the MC curve. Similarly to inclusive photons, the collective flow can be measured up to $|y| < 1.5$ in rapidity, and the statistics analyzed of 1 million Minimum Bias events, after event selection, allow the reconstruction of v_2 up to $p_{\mathrm{T}} \sim 2.5$ GeVc.

5.5.4. Dielectrons

Dielectrons (e^+e^- pairs) open another set of possibilities to explore the properties of hot matter. As they add another variable – the mass of the virtual photon – they provide the possibility to measure the temperature of hot matter without blue shift, which appears due to the radial expansion of the fireball in case of real photons. One can expect that, at NICA energies, the heavy-flavor decay contribution will be negligible and thermal virtual photon emission will be the dominant source in the intermediate mass region $1 < M_{\mathrm{ee}} < 3$ GeVcsq. This will provide access to the temperature of the hot source. Thermal photon emission will also appear in the low-mass region, $M_{\mathrm{ee}} < 0.5$ GeVcsq, where one can relate virtual and real photon yields with the Kroll-Wada formula [124] and calculate the real direct photon yield. Thermal dilepton emission in the low-mass region, $M_{\mathrm{ee}} < 0.7$ GeVcsq reflects the temperature of the hadron gas formed in the late stages of the collision and conveys information about the in-medium modification of the ρ-meson spectral function.

The MPD performance for electron measurement was studied and optimized using a sample of 15 million minimum bias Bi+Bi collisions at $\sqrt{s_{NN}} = 9.2$ GeV generated in mass production 1 from Table I. To improve the statistical significance of the dielectron yield in this relatively small sample of events, the branching ratios of dielectron sources, namely $\omega \to e^+e^-$, $\omega \to \pi^0 e^+e^-$, $\rho \to e^+e^-$, $\phi \to \eta e^+e^-$ and $\phi \to e^+e^-$, were increased by a factor of 20 in the decay generator table. The dilepton mass spectra were later scaled down to retrieve the realistic dielectron yield from these sources.

Furthermore, the yields and spectral shapes of the vector mesons $\rho^0(770)$, $\omega(782)$ and $\phi(1020)$ generated with UrQMD were rescaled to match more realistic predictions of the PHSD event generator.

The MPD is well suited for such measurements. Accurate tracking is provided by the TPC and electron identification, together with hadron rejection, are achieved by the combined effect of the measurements of the average specific energy loss dE/dx of the track while traversing the TPC gas, the particle time-of-flight in the TOF and ECAL detectors, and the particle energy in the ECAL. The latter contributes to electron

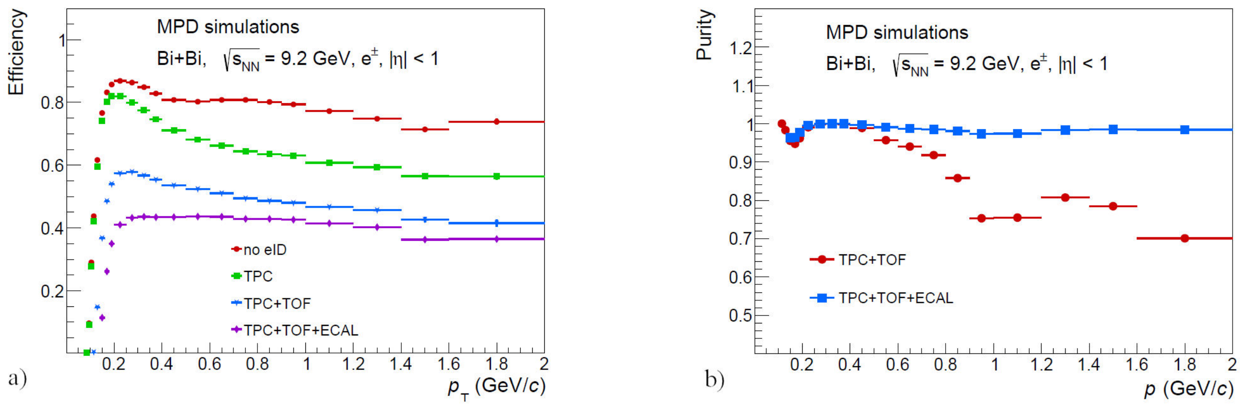

FIGURE 49. Electron track reconstruction and eID efficiency using different detector subsystems as a function of transverse momentum (upper panel) and electron purity (lower panel) achieved with and without ECAL for eID as a function of total momentum in Bi+Bi collisions at $\sqrt{s_{NN}} = 9.2$ GeV.

identification and hadron rejection by requiring the particle ratio E/p to be unity.

Event tracks that have a primary vertex reconstructed within —$z_{\text{vertex}}| < 130$ cm are reconstructed in the TPC within the pseudorapidity interval $|\eta| < 1.0$, requiring at least 39 hits out of a maximum of 53 hits, and are identified using a momentum-dependent cut on the truncated specific energy loss $\langle dE/dx \rangle$ signal. The tracks are then extrapolated to the vertex region and a 3σ cut is applied on the distance-of-closest-approach (DCA) to the primary vertex. This cut removes nearly 98% of the contributions from conversions occurring in the detector material behind the beam pipe. Finally, the tracks are extrapolated to the TOF and ECAL detectors and matched to the hits in these detectors within 2 or 3 σ of the extrapolation point in both the z and ϕ directions. The time-of-flight measurement of the track is provided primarily by the TOF detector. The ECAL also provides a measurement of the track time-of-flight. It has a worse time resolution of 250 ps at high energy, but the measurement is nonetheless useful as it provides electron identification (eID) for those tracks that fall within the inactive area between the modules of the TOF detector. The main benefit of the ECAL is the measurement of the particle energy which, coupled with its momentum reconstructed in the TPC, gives the E/p ratio - a critical discriminant variable for electron-hadron separation. All selection cuts applied along the track reconstruction and identification chain are listed in Table V.

The selection cuts result in a very good single electron reconstruction efficiency and electron purity, as depicted in Fig. 49. The upper panel of the figure shows the gradual decrease in the single-electron reconstruction efficiency as various matching and electron identification cuts are applied. The final single-electron reconstruction efficiency of fully reconstructed tracks (identified in TPC, TOF and ECAL) with $p_{\text{T}} > 200$ MeVc amounts to approximately 45%. The eequirement of a ECAL signal reduces the efficiency to zero for $p_{\text{T}} < 150$ MeVc as such tracks do not reach ECAL. The bottom panel shows an almost 100% purity of the final electron sample over the entire momentum range. The figure also shows that the purity of the electron sample, without the E/p cut enabled by the ECAL, is around 80% for $p_{\text{T}} > 1$ GeVc, highlighting the important role of the ECAL in reducing the hadronic contamination at high momenta. The reconstruction efficiency drops rapidly for electrons with $p_{\text{T}} < 200$ MeVc, reaching 0 at about $p_{\text{T}} = 100$ MeVc (for an electron emitted at $y = 0$, the minimum momentum to reach the TOF detector is 110 MeVc).

A novel pair analysis strategy for the measurement of dileptons at the MPD is being developed aiming at reducing the combinatorial background while maintainkng a high reconstruction efficiency. To enhance the chances of recognizing electrons originating from π^0 Dalitz decays and gamma conversions, the rapidity phase space of fully reconstructed electrons is divided into a fiducial ($|\eta| < 0.7$) and a veto ($0.7 < |\eta| < 1.0$) region. Fully reconstructed electron tracks in the fiducial area are paired among themselves or with tracks in the veto area. Unlike-sign pairs with $M_{\text{ee}} <$ 120 MeV/c^2 are tagged as pairs from π^0 Dalitz decais or conversions and are not used for further pairing. Furthermore, a proximity cut is applied in the TPC: fully reconstructed electron tracks in the fiducial area are paired with partially reconstructed electron tracks, *i.e.* electrons reconstructed in the TPC, and not identified at least in one of the outer detectors, the TOF or ECAL, and both tracks are removed as a potential Dalitz pair if they have $M_{\text{ee}} < 80$ MeV/c^2 and opening angle, $\theta < 5^\circ$ or 10°. The remaining fully reconstructed electron tracks in the fiducial area, with $p_{\text{T}} > 200$ MeVc, are paired among themselves to build the unlike sign (U) and like sign (L) invariant mass spectra.

The combinatorial background B is approximated by the L sign spectrum and thus the reconstructed signal is obtained as $\text{S} = \text{U}-\text{B} \approx \text{U}-\text{L}$, as shown in the upper panel of Fig. 50. The lower panel shows the differential S/B ratio. Currently, a S/B ratio of about 6% is observed over the integrated mass range of $0.2 < M_{\text{ee}} < 1.5$ GeVcsq. The S/B ratio that is obtained in the same mass range following a standard analy-

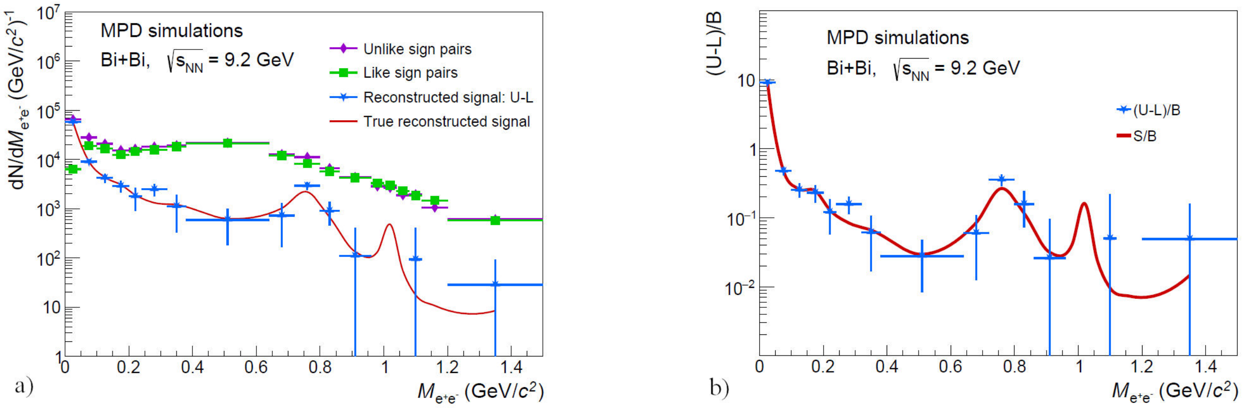

FIGURE 50. Distributions of Unlike sign (U), Like sign (L), measured signal (U-L) and True signal (S) pairs (upper panel) and measured ((U-L)/B) and true (S/B) signal-to-background ratios (lower panel) in Bi+Bi collisions at $\sqrt{s_{NN}} = 9.2$ GeV.

sis based on mixing of all tracks from the fiducial region, is about 2.6%. This demonstrates the advantage that is provided by the adopted analysis strategy.

In summary, the MPD experiment demonstrates a strong capability for comprehensive dielectron measurements, benefiting from excellent electron identification and high electron purity, particularly due to the critical role of the ECAL to reduce hadronic contamination. Tools such as machine learning, to further improve the S/B ratio and the signal significance, are currently under development.

6. Conclusions

In this work, the physics performance of the MPD experiment was studied in Bi+Bi collisions at $\sqrt{s_{NN}} = 9.2$ GeV using large samples of events simulated using UrQMD [14,15], DCM-QGSM-SMM [16], PHQMD [17], PHSD [18,19] and vHLLE+UrQMD [20,21] event generators. A wide variety of observables was analyzed, including the measurement of light-flavor hadrons and (hyper)nuclei, photons and (di)electrons, focusing on those expected to be available for an experimental study with the first collected data sets of 50–100 M events.

The measured differential particle yields span the phase space in transverse momentum and rapidity, corresponding to $\sim 70\%$ of the total light-flavor hadron production cross section. This provides a reduction of systematic uncertainties in the estimation of integrated particle yields, important for mapping the QCD phase diagram in terms of baryon chemical potential and temperature and for studying particle ratios in the strange sector. Differential p_T measurements cover a wide range from $p_T \sim 100$ MeVc to a few GeVc for most light hadrons, providing an opportunity to study the dynamics of heavy-ion collisions, and to better understand the kinetic freezeout conditions. The ability of the MPD to measure the production of various hadronic resonances over a wide range of lifetimes $\tau \sim 1 - 45$ fm/c helps to investigate the properties of the late hadronic phase, which may significantly affect the transition and CEP signatures.

The measurements for light nuclei (d, t) cover the midrapidity region ($|y| < 1$) and are more restricted in the low p_T range due to losses in the detector material. However, accurate reconstruction of the shapes of transverse spectra and rapidity distributions of nuclei is possible, allowing us to study the freezeout process and the role of momentum-space correlations in the production of nuclear clusters.

The feasibility studies showed that the measurement of hypertritons is possible with the MPD. The selection criteria for ${}^3_\Lambda$H reconstruction are optimized for best significance, the detector efficiency for ${}^3_\Lambda$H as a function of p_T is found to vary from 1% to 7% near mid-rapidity. It is shown that the data set volume that could be collected during the first period of data taking is sufficient to obtain enough statistics and to get the yields of hypertritons in several proper time intervals for the measurement of the ${}^3_\Lambda$H lifetime.

Performance of the MPD has been verified for anisotropic flow measurements of identified charged pions, kaons, protons and Λ particles as a function of rapidity (y) and transverse momentum (p_T) in different centrality classes. A detailed comparison of the results obtained from the analysis of the fully reconstructed data and generator-level data has allowed us to conclude that the MPD system will provide detailed differential measurements of directed v_1, elliptic (v_2) and triangular (v_3) flows with high efficiency.

Femtoscopic and correlation measurements are important tools to determine the space-time sizes and the hadronization properties of the particle-emitting source. The main limitation for an accurate determination of the parameters describing the space-time source of particles is the finite track resolution, which causes a smearing to distinguish single particle tracks. The smearing effect is estimated to be about 4.5 MeVc and this affects the determination of the femtoscopic parameters within less than 10% of the generated values. CBFs studies, describing the correlations of oppositely charged particles, were also performed. The rapidity and azimuthal widths of the reconstructed balance functions are shown to coincide within the sample statistics with the corresponding generated functions.

Photons in the MPD can be reconstructed and identified either in the ECAL or through the photon conversion method. The first approach provides a reconstruction efficiency close to unity, whereas the second one ensures purity close to unity. Photons can be used to reconstruct neutral-meson yields and correlations. A statistics of 50 M events is sufficient to extract the centrality-dependent neutral pion spectrum in the range $0.1 < p_{\rm T} < 4$ GeVc and an η-meson yield in minimum bias collisions. The estimated uncertainties of these spectra on the level of a few percent are sufficient to extract the direct-photon spectrum. Collective flows of inclusive photons and neutral pions are also extracted and agree with those at the generator level within statistical uncertainties, which at mid-$p_{\rm T}$ are at percent level for the 50 million events.

The ability to extract the dilepton spectrum was tested on the example of the UrQMD event generator. Although a sample of 50 million events is not sufficient to extract a high-statistics dilepton spectrum in Bi+Bi collisions, it provides a realistic estimate of the background levels and the required statistics.

Acknowledgments

The authors from the Institute of Physics and Technology, Satbayev University are funded by the Science Committee of the Ministry of Science and Higher Education of the Republic of Kazakhstan, Grant number AP23487706. The authors of Fudan University are supported by the China Ministry of Science and Technology (MOST) National Key R&D Program of China Grant number 2024YFA1611002 and the National Natural Science Foundation number 11925502. The authors of the MexNICA Collaboration acknowledge support from UNAM-PAPIIT grant number IG100322, from Consejo Nacional de Humanidades, Ciencia y Tecnología (CONAHCyT) grant numbers A1 S 7655 and CF-2023-G-433, from the DAI UAM PIPAIR 2024 projects under Grant number TR2024-800-00744 and the Consejo de la Investigación Científica de la Universidad Michoacana de San Nicolás de Hidalgo (CIC-UMSNH) grant number 18371. The authors of the High School of Economics University acknowledge support from the Basic Research Program at HSE University. The authors of the Kurchatov Institute acknowledge support from a state assignment of the National Research Centre. The work of the NRNU MEPhI group was funded by the Russian Federation Ministry of Science and Higher Education, project "Fundamental and applied research at the NICA (JINR) mega-science experimental complex" FSWU-2025-0014. The authors of the North Ossetian State University acknowledge support from grant number FEFN-2024-006. The authors of Peter the Great St. Petersburg Polytechnic University (SPbPU) acknowledge support from the Ministry of Science and Higher Education of the Russian Federation (FSEG-2025-0009). The authors of Saint-Petersburg State University acknowledge support from the University's research project number 103821868. The authors of the VINČA Institute of Nuclear Science acknowledge support from the Ministry of Science, Technological Development and Innovation of the Republic of Serbia through the theme 010220.

1. T. Ablyazimov *et al*., Challenges in QCD matter physics -The scientific programme of the Compressed Baryonic Matter ex2076 periment at FAIR, *Eur. Phys. J. A* **53** (2017) 60, https://doi.org/10.1140/epja/i2017-12248-y
2. J. Adams *et al*., Experimental and theoretical challenges in the search for the quark gluon plasma: The STAR Collaboration's critical assessment of the evidence from RHIC collisions, *Nucl. Phys. A* **757** (2005) 102, https://doi.org/10.1016/j.nuclphysa.2005.03.085
3. X. Luo *et al*., A Study of the Properties of the QCD Phase Di2084 agram in High-Energy Nuclear Collisions, *Particles* **3** (2020) 278, https://doi.org/10.3390/particles3020022
4. S. Borsanyi *et al*., Full result for the QCD equation of state with 2+1 flavors, *Phys. Lett. B* 730 (2014) 99, https://doi.org/10.1016/j.physletb.2014.01.007
5. M. A. Stephanov, K. Rajagopal, and E. V. Shuryak, Signatures of the tricritical point in QCD, *Phys. Rev. Lett*. **81** (1998) 4816, https://doi.org/10.1103/PhysRevLett.81.4816
6. J. Chen *et al*., Properties of the QCD matter: review of se2093 lected results from the relativistic heavy ion collider beam en ergy scan (RHIC BES) program, *Nucl. Sci. Tech.* **35** (2024) 214, https://doi.org/10.1007/s41365-024-01591-2
7. M. Gazdzicki, Ion Program of NA61/Shine at the CERN SPS, *J. Phys. G* **36** (2009) 064039, https://doi.org/10.1088/0954-3899/36/6/064039
8. X. Luo *et al*., eds., Properties of QCD Matter at High Baryon Density (Springer, 2022), https://doi.org/10.1007/978-981-19-4441-3
9. V. Golovatyuk *et al.*, Multi-Purpose Detector to study heavy ion collisions at the NICA collider, *Nucl. Phys. A* **982** (2019) 963, https://doi.org/10.1016/j.nuclphysa.2018.10.082
10. V. Abgaryan *et al*., Status and initial physics performance stud ies of the MPD experiment at NICA, *Eur. Phys. J. A* **58** (2022) 140, https://doi.org/10.1140/epja/s10050-022-00750-6
11. A. Averyanov *et al.*, MPD Technical Design Reports, (2109). https://mpd.jinr.ru/doc/mpd-tdr
12. M. Bleicher *et al.*, Relativistic hadron hadron collisions in the ultrarelativistic quantum molecular dynamics model, *J. Phys. G* **25** (1999) 1859, https://doi.org/10.1088/0954-3899/25/9/308

13. S. A. Bass *et al*., Microscopic models for ultrarelativistic heavy ion collisions, *Prog. Part. Nucl. Phys*. **41** (1998) 255, https://doi.org/10.1016/S0146-6410(98)00058-1

14. M. Baznat *et al*., Monte-Carlo Generator of Heavy Ion Collisions DCM-SMM, *Phys. Part. Nucl. Lett.* **17** (2020) 303, https://doi.org/10.1134/S1547477120030024

15. J. Aichelin *et al*., Parton-hadron-quantum-molecular dynamics: A novel microscopic n -body transport approach for heavy ion collisions, dynamical cluster formation, and hypernuclei production, *Phys. Rev. C* **101** (2020) 044905, https://doi.org/10.1103/PhysRevC.101.044905

16. W. Cassing and E. L. Bratkovskaya, Parton transport and hadronization from the dynamical quasiparticle point of view, *Phys. Rev. C* **78** (2008) 034919, https://doi.org/10.1103/PhysRevC.78.034919

17. W. Cassing and E. L. Bratkovskaya, Parton-Hadron-String Dynamics: an off-shell transport approach for relativistic energies, *Nucl. Phys. A* **831** (2009) 215, https://doi.org/10.1016/j.nuclphysa.2009.09.007

18. I. Karpenko, P. Huovinen, and M. Bleicher, A 3+1 dimensional viscous hydrodynamic code for relativistic heavy ion collisions, *Comput. Phys. Commun.* **185** (2014) 3016, https://doi.org/10.1016/j.cpc.2014.07.010

19. I. A. Karpenko *et al*., Estimation of the shear viscosity at finite net-baryon density from A + A collision data at $\sqrt{s_{NN}} = 7.7 - 200$ GeV, *Phys. Rev. C* **91** (2015) 064901, https://doi.org/10.1103/PhysRevC.91.064901

20. CERN-GEANT, Detector Description and Simulation Tool, https://geant4.cern.ch

21. Simulation and Analysis Framework for the MPD experiment of the NICA project, https://mpdroot.jinr.ru/

22. A. Baginyan *et al.*, Current Status of the MICC: an Overview, In 9th International Conference on Distributed Computing and Grid Technologies in Science and Education (2021) pp. 1-8.

23. N. Kutovskiy *et al.*, Integration of Distributed Heterogeneous Computing Resources for the MPD Experiment with DIRAC Interware, *Phys. Part. Nucl.* **52** (2021) 835, https://doi.org/10.1134/S1063779621040419

24. A. Moshkin *et al.*, Approaches, services, and monitoring in a distributed heterogeneous computing environment for theMPD experiment, *Russian Supercomputing Days* **2021** (2021) 4, https://doi.org/10.29003/m2454.RussianSCDays2021

25. A. Chatterjee *et al*., Effect of centrality selection on higher order cumulants of net-proton multiplicity distributions in relativistic heavy-ion collisions, *Phys. Rev. C* **101** (2020) 034902, https://doi.org/10.1103/PhysRevC.101.034902

26. X. Luo *et al*., Volume fluctuation and auto-correlation effects in the moment analysis of net-proton multiplicity distributions in heavy-ion collisions, *J. Phys. G* **40** (2013) 105104, https://doi.org/10.1088/0954-3899/40/10/105104

27. C. Loizides, J. Nagle, and P. Steinberg, Improved version of the PHOBOS Glauber Monte Carlo, *SoftwareX* **1-2** (2015) 13, https://doi.org/10.1016/j.softx.2015.05.001

28. P. Parfenov *et al.*, Anisotropic Flow Measurements of Identified Hadrons with MPD Detector at NICA, *Particles* **4** (2021) 146, https://doi.org/10.3390/particles4020014

29. P. Parfenov *et al*., Performance for Directed Flow Measurements of the MPD Experiment at NICA Collider, *Phys. Part. Nucl.* **52** (2021) 618, https://doi.org/10.1134/S106377962104047X

30. V. B. Luong *et al.*, Elliptic Flow and Its Fluctuations from TransportModels for Au+Au Collisions at = 7.7 and 11.5 GeV, *Particles* **6** (2022) 17, https://doi.org/10.3390/particles6010002

31. A. M. Poskanzer and S. A. Voloshin, Methods for analyzing anisotropic flow in relativistic nuclear collisions, *Phys. Rev. C* **58** (1998) 1671, https://doi.org/10.1103/PhysRevC.58.1671

32. E. Nazarova *et al*., Performance study of the hyperon global polarization measurements with MPD at NICA, *Eur. Phys. J. A* **60** (2024) 85, https://doi.org/10.1140/epja/s10050-024-01308-4

33. E. Schnedermann, J. Sollfrank, and U.W. Heinz, Thermal phenomenology of hadrons from 200-A GeV S+S collisions, *Phys. Rev. C* **48** (1993) 2462, https://doi.org/10.1103/PhysRevC.48.2462

34. J. Rafelski and B. Muller, Strangeness Production in the Quark - Gluon Plasma, *Phys. Rev. Lett.* **48** (1982) 1066, https://doi.org/10.1103/PhysRevLett.48.1066

35. C. Alt *et al*., Pion and kaon production in central Pb + Pb collisions at 20-A and 30-A-GeV: Evidence for the onset of de confinement, *Phys. Rev. C* **77** (2008) 024903, https://doi.org/10.1103/PhysRevC.77.024903

36. F. Antinori *et al.*, Enhancement of strange and multi-strange baryons and anti-baryons in SW interactions at 200-GeV/c, *Phys. Lett. B* **447** (1999) 178, https://doi.org/10.1016/S0370-2693(98)01561-5

37. G. Agakishiev *et al*., Strangeness Enhancement in Cu+Cu and Au+Au Collisions at $snn = 200$ GeV, *Phys. Rev. Lett.* **108** (2012) 072301, https://doi.org/10.1103/PhysRevLett.108.072301

38. B. B. Abelev *et al.*, Multi-strange baryon production at midrapidity in Pb-Pb collisions at $snn = 2.76$ TeV, *Phys. Lett. B* **728** (2014) 216, https://doi.org/10.1016/j.physletb.2014.05.052

39. C. Greiner and S. Leupold, Anti-hyperon production in relativistic heavy ion collision, J. Phys. G **27** (2001) L95, https://doi.org/10.1088/0954-3899/27/9/102

40. A. Palmese *et al*., Chiral symmetry restoration in heavy-ion collisions at intermediate energies, Phys. Rev. C **94** (2016) 044912, https://doi.org/10.1103/PhysRevC.94.044912

41. J. Cleymans, K. Redlich, and E. Suhonen, Canonical description of strangeness conservation and particle production, *Z. Phys. C* **51** (1991) 137, https://doi.org/10.1007/BF01579571

42. F. Becattini and J. Manninen, Centrality dependence of strangeness production in heavy-ion collisions as a geometrical effect of core-corona superposition, *Phys. Lett. B* **673** (2009) 19, https://doi.org/10.1016/j.physletb.2009.01.066

43. M. Ilieva *et al*., Reconstruction of multistrange hyperons with the MPD detector at the NICA collider: a Monte Carlo feasibility study, *Phys. Part. Nucl. Lett*. **12** (2015) 618, https://doi.org/10.1134/S1547477115040160

44. J. Adams *et al*., K(892)* resonance production in Au+Au and p+p collisions at s(NN)**(1/2) = 200 GeV at STAR, *Phys. Rev. C* **71** (2005) 064902, https://doi.org/10.1103/PhysRevC.71.064902

45. M. M. Aggarwal *et al*., K*0 production in Cu+Cu and Au+Au 2221 collisions at $snn = 62.4$ GeV and 200 GeV, *Phys. Rev. C* **84** (2011) 034909, https://doi.org/10.1103/PhysRevC.84.034909

46. B. I. Abelev *et al*., Hadronic resonance production in collisions at GeV measured at the BNL Relativistic Heavy Ion Collider, *Phys. Rev. C* **78** (2008) 044906, https://doi.org/10.1103/PhysRevC.78.044906

47. E. T. Yamamoto, Mid-rapidity φ production in Au+Au collisions at $\sqrt{s_{NN}} = 130$ GeV., *AIP Conf. Proc.* **610** (2002) 532, https://doi.org/10.1063/1.1469985

48. J. Adams *et al.*, phi meson production in Au + Au and p+p collisions at $snn =$ 200-GeV, *Phys. Lett. B* **612** (2005) 181, https://doi.org/10.1016/j.physletb.2004.12.082

49. B. I. Abelev *et al.*, Strange baryon resonance production in $\sqrt{s_{NN}} = 200$ GeV p+p and Au+Au collisions, *Phys. Rev. Lett.* **97** (2006) 132301, https://doi.org/10.1103/PhysRevLett.97.132301

50. B. I. Abelev *et al.*, Spin alignment measurements of the K*0(892) and phi (1020) vector mesons in heavy ion collisions at $\sqrt{s_{NN}} = 200$ GeV, *Phys. Rev. C* **77** (2008) 061902, https://doi.org/10.1103/PhysRevC.77.061902

51. B. B. Abelev *et al*., K*(892)0 and ϕ(1020) production in Pb-Pb collisions at $\sqrt{s_{NN}}$ = 2.76 TeV, *Phys. Rev. C* **91** (2015) 024609, https://doi.org/10.1103/PhysRevC.91.024609

52. J. Adam *et al*., Production of K* (892)0 and ϕ(1020) in p-Pb collisions at $\sqrt{s_{NN}}$ = 5.02 TeV, *Eur. Phys. J. C* **76** (2016) 245, https://doi.org/10.1140/epjc/s10052-016-4088-7

53. J. Adam *et al.*, K*(892)0 and ϕ(1020) meson production at high transverse momentum in pp and Pb-Pb collisions at $\sqrt{s_{NN}}$ = 2.76 TeV, *Phys. Rev. C* **95** (2017) 064606, https://doi.org/10.1103/PhysRevC.95.064606

54. D. Adamova *et al.*, Production of $\sum$(1385)$\pm$ and Ξ(1530)0 in p-Pb collisions at $\sqrt{s_{NN}}$ = 5.02 TeV, *Eur. Phys. J. C* **77** (2017) 389, https://doi.org/10.1140/epjc/s10052-017-4943-1

55. S. Acharya *et al*., Measurement of Λ(1520) production in pp collisions at $\sqrt{s}$ = 7 TeV and p-Pb collisions at $\sqrt{s_{NN}}$ =5.02 TeV, *Eur. Phys. J. C* **80** (2020) 160, https://doi.org/10.1140/epjc/s10052-020-7687-2

56. S. Acharya *et al*., Suppression of Λ(1520) resonance production in central Pb-Pb collisions at $\sqrt{s_{NN}}$ = 2.76 TeV, *Phys. Rev. C* **99** (2019) 024905, https://doi.org/10.1103/PhysRevC.99.024905

57. S. Acharya *et al*., Production of the ρ(770)0 meson in pp and Pb-Pb collisions at $\sqrt{s_{NN}}$ = 2.76 TeV, *Phys. Rev. C* **99** (2019) 064901, https://doi.org/10.1103/PhysRevC.99.064901

58. S. Acharya *et al*., Evidence of Spin-Orbital Angular Momentum Interactions in Relativistic Heavy-Ion Collisions, *Phys. Rev. Lett*. **125** (2020) 012301, https://doi.org/10.1103/PhysRevLett.125.012301

59. V. G. Riabov, Overview of ALICE results on light flavour hadron production, *J. Phys. Conf. Ser*. **1390** (2019) 012026, https://doi.org/10.1088/1742-6596/1390/1/012026

60. S. Acharya *et al.*, Evidence of rescattering effect in Pb-Pb collisions at the LHC through production of K*(892)0 and ϕ(1020) mesons, *Phys. Lett. B* **802** (2020) 135225, https://doi.org/10.1016/j.physletb.2020.135225

61. A. Adare *et al.*, Transverse energy production and charged particle multiplicity at midrapidity in various systems from $\sqrt{s_{NN}}$ = 7.7 to 200 GeV, *Phys. Rev. C* **93** (2016) 024901, https://doi.org/10.1103/PhysRevC.93.024901

62. V. Riabov, Hadronic resonances in heavy-ion collisions at NICA energies and their reconstruction in the MPD setup, *Int. J. Mod. Phys. A* **37** (2022) 2244003, https://doi.org/10.1142/S0217751X22440031

63. D. Ivanishchev, *et al.*, Study of Production Features, Mod2285 eling and Optimization of Algorithms for Reconstruction of Short-Lived Hadron Resonances in the MPD Experimental Setup at the NICA Collider, *Phys. Part. Nucl*. **52** (2021) 703, https://doi.org/10.1134/S1063779621040286

64. D. A. Ivanishchev *et al.*, Properties of ρ(770)0, K*(892), ϕ(1020), P (1385), Λ(1520) and Ξ(1530)0 resonances in heavy-ion collisions at a center of mass energy of and their re2292 construction using the MPD detector at NICA, *J. Phys. Conf. Ser.* **2103** (2021) 012140, https://doi.org/10.1088/1742-6596/2103/1/012140

65. P. A. Zyla *et al.*, Review of Particle Physics, *PTEP* **2020** (2020) 083C01, https://doi.org/10.1093/ptep/ptaa104

66. S. Zhang *et al*., Searching for onset deconfinement via hypernuclei baryon-strangeness correlations, *Phys. Lett. B* **684** (2010) 224, https://doi.org/10.1016/j.physletb.2010.01.034

67. J. Lattimer and M. Prakash, The physics of neutron stars, *Science* **304** (2004) 536, https://doi.org/10.1126/science.1090720

68. J. Steinheimer *et al.*, Hypernuclei, dibaryon and antinuclei production in high energy heavy ion collisions: Thermal production vs. coalescence. *Phys. Lett. B* **714** (2012) 85, https://doi.org/10.1016/j.physletb.2012.06.069

69. L. Adamczyk *et al*., Global Λ hyperon polarization in nuclear collisions: evidence for the most vortical fluid, *Nature* **548** (2017) 62, https://doi.org/10.1038/nature23004

70. M. I. Abdulhamid *et al*., Global polarization of Λ and Λ^- hyperons in Au+Au collisions at $\sqrt{s_{NN}}$=19.6 and 27 GeV, *Phys. Rev. C* **108** (2023) 014910, https://doi.org/10.1103/PhysRevC.108.014910

71. R. Abou Yassine *et al*., Measurement of global polarization of Λ hyperons in few-GeV heavy-ion collisions, *Phys. Lett. B* **835** (2022) 137506, https://doi.org/10.1016/j.physletb.2022.137506

72. A. Ayala *et al.*, Core meets corona: A two-component source to explain Λ and Λ^- 2317 global polarization in semi-central heavy-ion collisions, *Phys. Lett. B* **810** (2020) 135818, https://doi.org/10.1016/j.physletb.2020.135818

73. A. Ayal *et al.*, Rise and fall of Λ and Λ^- global polarization in semi-central heavy-ion collisions at HADES, NICA and RHIC energies from the core-corona model, *Phys. Rev. C* **105** (2022) 034907, https://doi.org/10.1103/PhysRevC.105.034907

74. X.-Y. Wu *et al.*, Local and global polarization of Λ hyperons 2325 across RHIC-BES energies: The roles of spin hall effect, initial condition, and baryon diffusion, *Phys. Rev. C* **105** (2022) 064909, https://doi.org/10.1103/PhysRevC.105.064909

75. J.-H. Gao, Global Polarization Theory Overview, *EPJ Web Conf.* **259** (2022) 02003, https://doi.org/10.1051/epjconf/202225902003

76. N. S. Tsegelnik, E. E. Kolomeitsev, and V. Voronyuk, Helicity and vorticity in heavy-ion collisions at energies available at the JINR Nuclotron-based Ion Collider facility, *Phys. Rev. C* **107** (2023) 034906, https://doi.org/10.1103/PhysRevC.107.034906

77. N. Tsegelnik, E. Kolomeitsev, and V. Voronyuk, Λ and Freeze-Out Distributions and Global Polarizations in Au+Au Collisions, *Particles* **6** (2023) 373, https://doi.org/10.3390/particles6010019

78. M. S. Abdallah *et al.*, Global Λ-hyperon polarization in Au+Au collisions at $\sqrt{s_{NN}}$=3 GeV, *Phys. Rev. C* **104** (2021) L06, https://doi.org/10.1103/PhysRevC.104.L061901

79. S. A. Voloshin, A. M. Poskanzer, and R. Snellings, Collective phenomena in non-central nuclear collisions, *Landolt-Bornstein* **23** (2010) 293, https://doi.org/10.1007/978-3-642-01539-7_10

80. A. Taranenko, Anisotropic flow measurements from RHIC 2347 to SIS, *EPJ Web Conf*. **204** (2019) 03009, https://doi.org/10.1051/epjconf/201920403009

81. A. Sorensen *et al*., Dense nuclear matter equation of state from heavy-ion collisions, *Prog. Part. Nucl. Phys.* **134** (2024) 104080, https://doi.org/10.1016/j.ppnp.2023.104080

82. A. Demanov, P. Parfenov, and A. Taranenko, Elliptic Flow Fluctuations at NICA Energy Range, *Phys. Part. Nucl.* **55** (2024) 1124, https://doi.org/10.1134/S1063779624700825

83. J. Auvinen and H. Petersen, Evolution of elliptic and triangular flow as a function of $\sqrt{s_{NN}}$ in a hybrid model, *Phys. Rev. C* **88** (2013) 064908, https://doi.org/10.1103/PhysRevC.88.064908

84. S. Pratt, Pion Interferometry of Quark-Gluon Plasma, *Phys. Rev. D* **33** (1986) 1314, https://doi.org/10.1103/PhysRevD.33.1314

85. G. Bertsch, M. Gong, and M. Tohyama, Pion Interferometry in Ultrarelativistic Heavy Ion Collisions, *Phys. Rev. C* **37** (1988) 1896, https://doi.org/10.1103/PhysRevC.37.1896

86. P. Batyuk *et al.*, Correlation femtoscopy study at energies available at the JINR Nuclotron-based Ion Collider fAcility and the BNL Relativistic Heavy Ion Collider within a viscous hydrodynamic plus cascade model, *Phys. Rev. C* **96** (2017) 024911, https://doi.org/10.1103/PhysRevC.96.024911

87. G. I. Kopylov, The kinematics of inclusive experiments with unstable particles, *Phys. Lett. B* **41** (1972) 371, https://doi.org/10.1016/0370-2693(72)90598-9

88. G. I. Kopylov and M. I. Podgoretsky, Correlations of identical particles emitted by highly excited nuclei, *Sov. J. Nucl. Phys.* **15** (1972) 219.

89. S. Acharya *et al*., Femtoscopic correlations of identical charged pions and kaons in pp collisions at $s = 13$ TeV with event-shape selection, *Phys. Rev. C* **109** (2024) 024915, https://doi.org/10.1103/PhysRevC.109.024915

90. A. Tumasyan *et al.*, Two-particle Bose-Einstein correlations and their Lévy parameters in PbPb collisions at $sNN = 5.02$ TeV, *Phys. Rev. C* **109** (2024) 024914, https://doi.org/10.1103/PhysRevC.109.024914

91. V. A. Schegelsky, Levy Analysis of Bose-Einstein Correlation in pp Collisions at $\sqrt{s}$ = 7 TeV Measured with the AT2384 LAS, *Phys. Part. Nucl. Lett.* **16** (2019) 503, https://doi.org/10.1134/S1547477119050261

92. M. Csanád and D. Kincses, Femtoscopy with Lévy sources from SPS through RHIC to LHC (2024), https://doi.org/10.3390/universe10020054

93. A. Ayala *et al.*, Collision energy dependence of source sizes for primary and secondary pions at energies available at the JINR nuclotron-based ion collider facility from Lévy fits, *Eur. Phys. J. A* **60** (2024) 135, https://doi.org/10.1140/epja/s10050-024-01350-2

94. M. G. Bowler, Coulomb corrections to Bose-Einstein correlations have been greatly exaggerated, *Phys. Lett. B* **270** (1991) 69, https://doi.org/10.1016/0370-2693(91)91541-3

95. Y. Sinyukov *et al*., Coulomb corrections for interferometry analysis of expanding hadron systems, *Phys. Lett. B* **432** (1998) 248, https://doi.org/10.1016/S0370-2693(98)00653-4

96. S. Acharya *et al.*, Towards the understanding of the genuine three-body interaction for p-p-p and p-p-Λ, *Eur. Phys. J. A* **59** (2023) 145, https://doi.org/10.1140/epja/s10050-023-00998-6

97. M. Cheremnova *et al*., Particle Multiplicity Fluctuations and Spatiotemporal Properties of Particle-Emitting Source of Strongly Interacting Matter for NICA and RHIC Energies, *Symmetry* **14** (2022) 1316, https://doi.org/10.3390/sym14071316

98. S. Acharya *et al*., Investigation of K^+k^- interactions via femtoscopy in Pb-Pb collisions at $sNN = 2.76$ TeV at the CERN Large Hadron Collider, *Phys. Rev. C* **107** (2023) 054904, https://doi.org/10.1103/PhysRevC.107.054904

99. S. V. Akkelin and Y. M. Sinyukov, The HBT interferometry of expanding sources, *Phys. Lett. B* 356 (1995) 525, https://doi.org/10.1016/0370-2693(95)00765-D

100. J. Adams *et al.*, Pion interferometry in Au+Au collisions at S(NN)**(1/2) = 200-GeV, *Phys. Rev. C* **71** (2005) 044906, https://doi.org/10.1103/PhysRevC.71.044906

101. S. A. Bass, P. Danielewicz, and S. Pratt, Clocking hadronization in relativistic heavy ion collisions with balance functions, *Phys. Rev. Lett*. **85** (2000) 2689, https://doi.org/10.1103/PhysRevLett.85.2689

102. S. Pratt and C. Plumberg, Charge balance functions for heavyion collisions at energies available at the CERN Large Hadron Collider, *Phys. Rev. C* **104** (2021) 014906, https://doi.org/10.1103/PhysRevC.104.014906

103. C. Alt *et al*., System size and centrality dependence of the balance function in A + A collisions at s(NN)**(1/2) = 17.2-GeV, *Phys. Rev. C* **71** (2005) 034903, https://doi.org/10.1103/PhysRevC.71.034903

104. M. M. Aggarwal *et al.*, Balance Functions from Au+Au, d+Au, and p + p Collisions at $\sqrt{s_{NN}}$ = 200 GeV, *Phys. Rev. C* **82** (2010) 024905, https://doi.org/10.1103/PhysRevC.82.024905

105. L. Adamczyk *et al.*, Beam-energy dependence of charge balance functions from Au + Au collisions at energies available at the BNL Relativistic Heavy Ion Collider, *Phys. Rev. C* **94** (2016) 024909, https://doi.org/10.1103/PhysRevC.94.024909

106. B. Abelev *et al.*, Charge correlations using the balance function in Pb-Pb collisions at $\sqrt{s_{NN}}$ = 2.76 TeV, *Phys. Lett. B* **723** (2013) 267, https://doi.org/10.1016/j.physletb.2013.05.039

107. S. Acharya *et al*., Two particle differential transverse momentum and number density correlations in p-Pb and Pb-Pb at the LHC, *Phys. Rev. C* **100** (2019) 044903, https://doi.org/10.1103/PhysRevC.100.044903

108. J. Pan, Balance functions of (un)identified hadrons in Pb-Pb, p-Pb, and pp collisions at the LHC, *Nucl. Phys. A* **982** (2019) 315, https://doi.org/10.1016/j.nuclphysa.2018.09.022

109. D. Blau and D. Peresunko, Direct Photon Production in Heavy-Ion Collisions: Theory and Experiment, *Particles* **6** (2023) 173, https://doi.org/10./particles6010009

110. E. Kryshen *et al.*, Thermal Photon and Neutral Meson Mea2450 surements Using the Photon Conversion Method in the MPD Experiment at the NICA Collider, *Phys. Part. Nucl*. **52** (2021) 669, https://doi.org/10.1134/S1063779621040390

111. G. Dellacasa *et al.*, ALICE technical design report of the photon spectrometer (PHOS) (1999)

112. A. Y. Semenov *et al.*, Electromagnetic Calorimeter for MPD Spectrometer at NICA Collider, JINST **15** (2020) C05017, https://doi.org/10.1088/1748-0221/15/05/C05017

113. V. V. Begun andM. I. Gorenstein, Bose-Einstein condensation of pions in high multiplicity events, *Phys. Lett. B* **653** (2007) 190, https://doi.org/10.1016/j.physletb.2007.07.059

114. M. A. Stephanov, Thermal fluctuations in the interacting pion gas, *Phys. Rev. D* **65** (2002) 096008, https://doi.org/10.1103/PhysRevD.65.096008

115. N. M. Kroll and W. Wada, Internal pair production associated with the emission of high-energy gamma rays, *Phys. Rev*. **98** (1955) 1355, https://doi.org/10.1103/PhysRev.98.1355

116. B. V. Jacak, High-energy heavy ion collisions: The Physics of superdense matter, In 30th International Conference on High-Energy Physics (2000) pp. 261-271.

117. S. Acharya *et al.*, The ALICE experiment: a journey through QCD, *Eur. Phys. J. C* **84** (2024) 813, https://doi.org/10.1140/epjc/s10052-024-12935-y

118. Y. Akiba *et al.*, The Hot QCD White Paper: Exploring the Phases of QCD at RHIC and the LHC (2015).

119. New State of Matter created at CERN. Un nouvel état de la matiére (2000), https://cds.cern.ch/record/716634

120. D. Kincses, M. Stefaniak, and M. Csanád, Event-by-Event Investigation of the Two-Particle Source Function in Heavy-Ion Collisions with EPOS, *Entropy* **24** (2022) 308, https://doi.org/10.3390/e24030308

121. A. Maevskiy *et al.*, Simulating the time projection chamber responses at the MPD detector using generative adversarial networks, *Eur. Phys. J. C* **81** (2021) 599, https://doi.org/10.1140/epjc/s10052-021-09366-4

122. T. Csorgo *et al*., Bose-Einstein or HBT correlations and the anomalous dimension of QCD, *Acta Phys. Polon. B* **36** (2005) 329.

123. T. Csorgo, Correlation Probes of a QCD Critical Point, *PoS HIGH-PTLHC* **08** (2008) 027, https://doi.org/10.22323/1.076.0027

124. T. Csorgo *et al*., Bose-Einstein or HBT correlation signature of a second order QCD phase transition, *AIP Conf. Proc*. **828** (2006) 525, https://doi.org/10.1063/1.2197465

125. S. Pratt *et al*., Testing transport theories with correlation measurements, *Nucl. Phys. A* **566** (1994) 103C, https://doi.org/10.1016/0375-9474(94)90614-9

126. N. Ermakov and G. Nigmatkulov, Modeling of two-particle femtoscopic correlations at top RHIC energy, *J. Phys. Conf. Ser.* **798** (2017) 012055, https://doi.org/10.1088/1742-6596/798/1/012055

127. Q. Li, G. Graef, and M. Bleicher, UrQMD calculations of two-pion HBT correlations in p+p and Pb+Pb collisions at LHC energies, *J. Phys. Conf. Ser*. **420** (2013) 012039, https://doi.org/10.1088/1742-6596/420/1/012039

128. W. A. Zajc *et al*., Two-pion correlations in heavy ion colli2506 sions, *Phys. Rev. C* **29** (1984) 2173, https://doi.org/10.1103/PhysRevC.29.2173

129. U. A. Wiedemann and U. W. Heinz, Particle interferometry for relativistic heavy ion collisions, *Phys. Rept*. **319** (1999) 145, https://doi.org/10.1016/S0370-1573(99)00032-0

130. H. Adhikary *et al.*, Two-pion femtoscopic correlations in Be+Be collisions at $\sqrt{s_{NN}}$ = 16.84 GeV measured by the NA61/SHINE at CERN, *Eur. Phys. J. C* **83** (2023) 919, https://doi.org/10.1140/epjc/s10052-023-11997-8
131. M. Bystersky, Non-Gaussian effects in identical pion correlation function at STAR, *AIP Conf. Proc.* **828** (2006) 533, https://doi.org/10.1063/1.2197466
132. T. Csorgo, S. Hegyi, and W. A. Zajc, Bose-Einstein correlations for Levy stable source distributions, *Eur. Phys. J. C* **36** (2004) 67, https://doi.org/10.1140/epjc/s2004-01870-9
133. J. Cimerman, C. Plumberg, and B. Tomášik, The Shape of the Correlation Function, *Phys. Part. Nucl*. **51** (2020) 282.
134. M. Y. Bogolyubsky *et al*., Characteristics of the groups of charged particles in anti-p p, p p and K-p interactions at 32-GeV/c, *Phys. Atom. Nucl*. **58** (1995) 1877
135. M. Y. Bogolyubsky *et al*., Clan model and factorial moments of the multiplicity distribution in intervals, *Phys. Atom. Nucl*. **57** (1994) 2132
136. K. U. Abraamyan *et al*., The MPD detector at the NICA heavy-ion collider at JINR, *Nucl. Instrum. Meth. A* **628** (2011) 99, https://doi.org/10.1016/j.nima.2010.06.293
137. I. P. Lokhtin *et al.*, Heavy ion event generator HYDJET++ (HYDrodynamics plus JETs), *Comput. Phys. Commun*. **180** (2009) 779, https://doi.org/10.1016/j.cpc.2008.11.015
138. A. Giovannini and L. Van Hove, Negative Binomial Properties and Clan Structure in Multiplicity Distributions, *Acta Phys. Polon. B* **19** (1988) 495.
139. P. Sarma and B. Bhattacharjee, Color reconnection as a possible mechanism of intermittency in the emission spectra of charged particles in PYTHIA-generated high-multiplicity pp collisions at energies available at the CERN Large Hadron Collider, *Phys. Rev. C* **99** (2019) 034901, https://doi.org/10.1103/PhysRevC.99.034901
140. R. Sharma and R. Gupta, Scaling Properties of Multiplicity Fluctuations in the AMPT Model, *Adv. High Energy Phys.* **2018** (2018) 6283801, https://doi.org/10.1155/2018/6283801
141. O. Kodolova *et al.*, Factorial Moments in the NICA/MPD Experiment, *Phys. Part. Nucl.* **52** (2021) 658, https://doi.org/10.1134/S106377962104033X
142. T. Anticic *et al.*, Critical fluctuations of the proton density in A+A collisions at 158 A GeV, *Eur. Phys. J. C* **75** (2015) 587, https://doi.org/10.1140/epjc/s10052-015-3738-5
143. N. Davis, Searching for the Critical Point of Strongly Interacting Matter in Nucleus-Nucleus Collisions at CERN SPS, *Acta Phys. Polon. Supp.* **13** (2020) 637, https://doi.org/10.5506/APhysPolBSupp.13.637
144. M. Mohisin Khan *et al*., Improved intermittency analysis of charged particle density fluctuations in Pb+Pb collisions at $\sqrt{s_{NN}}$ = 2.76 TeV, *DAE Symp. Nucl. Phys.* **61** (2016) 840.
145. N. G. Antoniou, N. N. Davis, and F. K. Diakonos, Improved intermittency analysis of proton density fluctuations in NA49 ion collisions at 158 AGeV, *EPJ Web Conf.* **71** (2014) 00035, https://doi.org/10.1051/epjconf/20147100035
146. A. Bialas and R. B. Peschanski, Moments of Rapidity Distributions as a Measure of Short Range Fluctuations in High-Energy Collisions, *Nucl. Phys. B* **273** (1986) 703, https://doi.org/10.1016/0550-3213(86)90386-X
147. M. Hippert and E. S. Fraga, Multiplicity fluctuations near the QCD critical point, *Phys. Rev. D* **96** (2017) 034011, https://doi.org/10.1103/PhysRevD.96.034011
148. A. Adare *et al*., Lévy-stable two-pion Bose-Einstein correlations in $\sqrt{s_{NN}}$ = 200 GeV Au+Au collisions, *Phys. Rev. C* **97** (2018) 064911, https://doi.org/10.1103/PhysRevC.97.064911
149. M. Csanad, Exploring the QCD phase diagram via the collision energy dependence of multi-particle femtoscopy with PHENIX, *J. Phys. Conf. Ser*. **1602** (2020) 012009, https://doi.org/10.1088/1742-6596/1602/1/012009
150. A. Bzdak *et al*., Mapping the Phases of Quantum Chromodynamics with Beam Energy Scan, *Phys. Rept*. **853** (2020) 1, https://doi.org/10.1016/j.physrep.2020.01.005
151. M. Nagy *et al.*, A novel method for calculating Bose-Einstein correlation functions with Coulomb final-state interaction, *Eur. Phys. J. C* **83** (2023) 1015, https://doi.org/10.1140/epjc/s10052-023-12161-y
152. T. Csorgo, B. Lorstad, and J. Zimanyi, Bose-Einstein correlations for systems with large halo, *Z. Phys. C* **71** (1996) 491, https://doi.org/10.1007/s002880050195
153. B. Porfy, Femtoscopic Correlation Measurement with Sym2589 metric Lévy-Type Source at NA61/SHINE, *Universe* **9** (2023) 298, https://doi.org/10.3390/universe9070298
154. D. Kincses, PHENIX results on Lévy analysis of Bose-Einstein correlation functions, *Acta Phys. Polon. Supp*. **10** (2017) 627, https://doi.org/10.5506/APhysPolBSupp.10.627
155. D. Kincses, Lévy analysis of HBT correlation functions in $\sqrt{s_{NN}}$ = 62 GeV and 39 GeV Au+Au collisions at PHENIX, *Universe* **4** (2018) 11, https://doi.org/10.3390/universe4010011
156. S. Lökös, Lévy-stable two-pion Bose-Einstein correlation functions measured with PHENIX in $\sqrt{s_{NN}}$ = 200 GeV Au+Au collisions, In 13th Workshop on Particle Correlations and Femtoscopy (2018).
157. A. Mukherjee, Kaon femtoscopy with Lévy-stable sources from $\sqrt{s_{NN}}$ = 200 GeV Au + Au collisions at RHIC, *Universe* **9** (2023) 300, https://doi.org/10.3390/universe9070300
158. U. A. Wiedemann and U. W. Heinz, Resonance contributions to HBT correlation radii, *Phys. Rev. C* **56** (1997) 3265, https://doi.org/10.1103/PhysRevC.56.3265
159. J. Bolz *et al*., Resonance decays and partial coherence in Bose-Einstein correlations, *Phys. Rev. D* **47** (1993) 3860, https://doi.org/10.1103/PhysRevD.47.3860
160. T. Csorgo, Particle interferometry from 40-MeV to 40-TeV, *Acta Phys. Hung. A* **15** (2002) 1, https://doi.org/10.1556/APH.15.2002.1-2.1